N = 7 SHELL EVOLUTION AT AND BEYOND THE NEUTRON DRIPLINE

By

Daniel Gregory Jenks Votaw

A DISSERTATION

Submitted to
Michigan State University
in partial fulfillment of the requirements
for the degree of

Physics - Doctor of Philosophy

2019

ABSTRACT

N = 7 SHELL EVOLUTION AT AND BEYOND THE NEUTRON DRIPLINE

By

Daniel Gregory Jenks Votaw

This dissertation reports the results of a search for the controversial parity inversion in the unbound $N = 7$ isotones ^{9}He and ^{10}Li. Proton removal reactions from two different radioactive ion beams (^{11}Be, $E_{lab} = 44$ MeV/u and ^{12}B, $E_{lab} = 45$ MeV/u) on a beryllium target were used to directly and selectively populate unbound resonances of a given neutron configuration in the nuclides of interest. Neutrons and fragments were measured in coincidence using the MoNA-LISA-Sweeper setup, and invariant mass spectroscopy or the time-of-flight method were used to determine the decay energy or relative velocity of the neutron decays. Results on multiple unbound resonances in the ^{9}He and ^{10}Li systems will be presented, as well as a discussion of ground state level inversion.

ACKNOWLEDGMENTS

My time at MSU has been very rewarding, and I owe many thanks to all of the people who helped make it that way. First, I want to thank my advisor, Michael Thoennessen, for always providing guidance and mentorship, even after leaving MSU and starting a new job in a different state. His commitment to mentoring his students is unparalleled, and it was truly an honor to be one of them. I would also like to thank the members of my guidance committee: Daniel Bazin, Scott Bogner, Laura Chomiuk, and Wade Fisher, whose feedback and suggestions over the years have been very helpful. I am very grateful for their time and attention throughout my time here.

All of the members of the MoNA Collaboration also contributed greatly to my time at MSU. The Collaboration has always been welcoming and supportive, and I will greatly miss being a part of it. I would like to specifically point out the collaborators who regularly attended my weekly analysis meetings: Thomas Baumann, Paul DeYoung, and Anthony Kuchera. Their consistent, vigilant guidance is what got me through a major DAQ/analysis software upgrade right before my thesis experiment, all the way through years of data analysis, and finally to the results which will be presented in this dissertation. I would also like to specifically acknowledge Paul Gueye for moving from Virginia to Michigan in order to help maintain a strong local MoNA presence at the NSCL after Michael's move. And I would also like to thank Paul for opening doors for collaboation with Jefferson Lab, and for his seemingly infinite supply of "crazy" ideas. To the rest of the (present and former) MoNA PIs with whom I've have the pleasure of working, Jim Brown, Joe Finck, Nathan Frank, Jerry Hinnefeld, Bryan Luther, Warren Rogers, Artemis Spyrou, and Sharon Stephenson, I offer my thanks to all of you as well.

I also must acknowledge the MoNA graduate students with whom I've worked over the years. Each and every one of them has positively influenced by graduate school experience in some way. Michael Jones, Krystin Stiefel, Han Liu, Thomas Redpath, Dayah Chrisman, and Hank Thurston, thank you all, and I wish you all the best of luck in your careers.

A few NSCL staff members who made great contributions to setting up my thesis experiment deserve recognition: Ron Fox, Jorge Pereira, Jeromy Tompkins, and Daniel Bazin. Without them, we may not have had functioning detectors and data acquisition software.

I would also like to thank Sean Liddick and the Nuclear Science and Security Consortium for the opportunities to attend many conferences, workshops, and summer schools related to nuclear nonproliferation, and the chance to spend a summer at Los Alamos National Laboratory. Aaron Couture, Shea Mosby, Chris Prokop, and the rest of the P-27 group at LANL deserve thanks for the great summer I had out in New Mexico.

Finally, I would like to thank my family and friends, who always supported my choice to move to Michigan and pursue a Ph.D. in physics. None of them have ever shown me a shred of doubt in my decision. I look forward to seeing what the next chapter brings.

TABLE OF CONTENTS

LIST OF TABLES . . . . **vii**

LIST OF FIGURES . . . . **viii**

Chapter 1 Introduction **1**
- 1.1 The nuclear landscape 1
- 1.2 The nuclear shell model 5
- 1.3 Shell evolution and inversion 7
- 1.4 Previous experiments with the $N = 7$ isotones 9

Chapter 2 Theoretical Background **11**
- 2.1 s-wave ($\ell = 0$) lineshape 11
- 2.2 Energy-dependent Breit-Wigner ($\ell > 0$) lineshape 13

Chapter 3 Experimental Techniques **17**
- 3.1 Primary beam 17
- 3.2 Secondary beams 18
- 3.3 N2 vault 19
  - 3.3.1 Sweeper magnet 20
  - 3.3.2 Charged particle detectors 22
    - 3.3.2.1 Timing scintillators 22
    - 3.3.2.2 Cathode Readout Drift Chambers 23
    - 3.3.2.3 Ion chamber 24
  - 3.3.3 Neutron detectors 25
  - 3.3.4 Electronics and DAQ 28
    - 3.3.4.1 Hardware 28
    - 3.3.4.2 Software 31
- 3.4 Invariant mass spectroscopy 35
- 3.5 Time-of-Flight method 37

Chapter 4 Data Analysis **39**
- 4.1 Detector calibrations and corrections 39
  - 4.1.1 Charged particle timing scintillators 39
  - 4.1.2 CRDCs 43
  - 4.1.3 Ionization chamber 48
  - 4.1.4 MoNA-LISA 51
    - 4.1.4.1 QDC calibration 52
    - 4.1.4.2 TDC calibration 54
    - 4.1.4.3 x-position calibration 55
    - 4.1.4.4 T_{mean} calibration 56
- 4.2 Event selection 58

        - 4.2.1 Beam gate 58
        - 4.2.2 CRDC quality gates 59
        - 4.2.3 Charged fragments 60
        - 4.2.4 Neutrons 64
    - 4.3 Fragment tracking 65
    - 4.4 Simulation 69
        - 4.4.1 Beam parameters 71
        - 4.4.2 Reaction parameters 73
        - 4.4.3 Decay parameters 75
    - 4.5 Parameter estimation 76
        - 4.5.1 Binned likelihood parameter estimation 76
        - 4.5.2 Simulated annealing 79

Chapter 5 Results and Discussion 82
    - 5.1 ^{12}B(-3p)^{9}He 82
    - 5.2 ^{11}Be(-2p)^{9}He 85
    - 5.3 ^{12}B(-2p)^{10}Li 92
    - 5.4 ^{11}Be(-1p)^{10}Li 94

Chapter 6 Summary and Conclusions 96

APPENDIX 98

REFERENCES 100

LIST OF TABLES

Table 3.1: Estimated secondary beam parameters. 20

Table 4.1: Unreacted secondary beam velocities. 40

Table 4.2: Charged particle timing detector offsets. 41

Table 4.3: CRDC mask calibration parameters. 47

Table 4.4: The common inputs to COSY used for all settings in this analysis. 68

Table 4.5: Sweeper current, magnetic field, and rigidities for various settings used in this work. The Hall probe is physically located near the edge of the magnet, so the Hall probe value is not indicative of the central field strength, which is usually on the order of 1 Tesla. 69

Table 4.6: The simulated beam parameters used in this analysis. 71

Table 4.7: The simulated reaction parameters. 75

Table 5.1: Statistical and systematic uncertainties in the fitting of the resonance parameters for ^{12}B(-3p)^{9}He. The values for the E_1 and E_2 parameters are for two-sided intervals, and the values for the Γ_1 and Γ_2 parameters correspond to one-sided deviations from the likelihood maximum. 84

Table 5.2: Statistical and systematic uncertainties in the fitting of the scattering length for ^{11}Be(-2p)^{9}He. 92

Table 5.3: ^{10}Li resonance parameters from the Ph.D. dissertation of J. K. Smith [1]. 93

LIST OF FIGURES

Figure 1.1: The Chart of Nuclides, from NNDC [2]. The colors indicate ground state half-lives. 2

Figure 1.2: The first few single-particle orbitals in the nuclear mean field potential, from Wikipedia [3]. 6

Figure 1.3: The chart of nuclides, with the observed regions of inversion highlighted, from the dissertation of J. K. Smith [1]. 8

Figure 2.1: Normalized s-wave lineshapes for various values of the scattering length (a) and binding energy (ε_b) parameters. The effective range parameter was fixed at 4 fm. 13

Figure 3.1: The Coupled Cyclotron Facility and the A1900 fragment separator. . . . 18

Figure 3.2: The N2 vault experimental layout. 20

Figure 3.3: A schematic drawing of the Sweeper magnet, from Reference [4]. Both the superconducting Sweeper coils (horizontal) and normal-conducting trim coils (vertical) are shown in the diagram on the right. 21

Figure 3.4: A schematic drawing of the thin scintillator. Adopted and modified from Reference [5]. 23

Figure 3.5: A schematic drawing of a CRDC, from Reference [6]. 24

Figure 3.6: A schematic drawing of the ion chamber, from Reference [1]. 25

Figure 3.7: A schematic drawing of a single MoNA-LISA bar, from Reference [1]. . . 26

Figure 3.8: The layout of the tables, layers, and bars of MoNA-LISA. 27

Figure 3.9: A diagram of the DAQ hardware. Data sources are shown in green, signal processing modules in yellow, Level 1, 2, and 3 logic in grey. Green arrows represent START signals, red arrows represent STOP signals, and blue arrows represent GATE signals. The cyan arrow is the system trigger from the Thin Left Up. 30

Figure 3.10: A diagram of the DAQ software. Data sources are shown in green, data sinks in red, ring buffers in yellow, and event builders in blue. The arrows indicate the direction of the data flow. 32

Figure 3.11: The contents of a PHYSICS_EVENT ring item in the Sweeper ring buffer, adapted from the Sweeper DAQ Wiki [7]. Ring items like this are consumed both by a Sweeper-only SpecTcl program, and the master event builder, which will combine this item with the corresponding ring items from MoNA and LISA. 34

Figure 3.12: A schematic representation of the 2-body decay ^{9}He $\rightarrow$ ^{8}He + n. 35

Figure 4.1: The first stage of time calibration of the target scintillator. The left panel shows the raw TDC spectrum. The right panel shows the spectrum after applying the slope, but before subtracting the jitter, and applying the offset. These data were taken from a target-out run where the Sweeper magnet was set to center the ^{11}Be beam (Run 2005). 42

Figure 4.2: The second stage of time calibration of the target scintillator. The left panel shows the TDC spectrum after applying the slope and jitter subtraction, but before applying the offset. The right panel shows the spectrum after applying the offset. These data were taken from a target-out run where the Sweeper magnet was set to center the ^{11}Be beam (Run 2005). 43

Figure 4.3: The pedestal distributions for the CRDCs, taken offline at the beginning of the experiment (Run 2001). The left panel shows CRDC1 and the right panel shows CRDC2. 45

Figure 4.4: The gain-matching of the CRDC2 pads. The left panel shows the pad summary before pedestal subtraction and gain-matching, and the right panel shows the pad summary after. The same procedure was applied to both CRDCs, and the reference pad for both was chosen to be Pad 75. The data come from a chain of Run 2026 (centered ^{12}B), and Runs 2032 - 2039 (sweeping ^{12}B). 46

Figure 4.5: The mask calibration of CRDC2. The left panel shows the uncalibrated spectrum, and the right panel shows the calibrated spectrum. Due to the physical orientation of the detector, the calibration involves a horizontal and vertical reflection. The data are taken from Run 2083, where the target was removed, the ^{12}B beam was centered, and the CRDC2 mask was inserted. 48

Figure 4.6: The energy loss spectra of each good pad overlaid. The left plot shows all of the raw energy loss spectra, and the right panel shows all of the gain-matched energy loss spectra. The largest two peaks in the spectra were fit to Gaussian functions, and their centroids were linearly transformed to align with the reference pad (marked in red). These data were taken from a target-out run where the Sweeper magnet was set to center the ^{11}Be beam (Run 2005). 49

Figure 4.7: The horizontal position correction of the ion chamber energy loss. The left panel shows the uncorrected spectrum, and the right panel shows the corrected spectrum, with reduced position-dependence. The data come from a chain of Run 2026 (centered ^{12}B), and Runs 2032 - 2039 (sweeping ^{12}B). 51

Figure 4.8: The QDC calibration for one PMT in LISA. The left spectrum is uncalibrated, and the right spectrum is calibrated. After calibration, the pedestal is removed, and the features which remain are a sharp peak at low charge due to background γ-rays, and a broad cosmic muon peak. . . 53

Figure 4.9: The TDC calibration for one PMT in LISA. The left spectrum is uncalibrated, and the right spectrum is calibrated. These data are taken from a time calibrator run, where the "picket fence" spacing is set to 40 ns. This is used to determine the TDC slope for each PMT in the array. The offsets are determined later, using the method described in subsequent sections. 54

Figure 4.10: The x-position calibration for one bar in LISA. The left spectrum is uncalibrated, and the right spectrum is calibrated. These data are taken from a cosmic muon run. The vertical lines in the calibrated spectrum represent the physical ends of the bars. Some small number of counts fall outside these lines due to the stochastic nature of the detector response. 56

Figure 4.11: ^{11}Be secondary beam identification gate. A 1D cut requiring the ToF to lie between the red vertical lines is used to select events where the incoming particle is ^{11}Be. The main contaminant in this case is ^{14}C, which is easily removed by applying this gate. The same process is applied to the ^{12}B beam, even though it is almost pure. 59

Figure 4.12: The CRDC quality gates used for the ^{11}Be beam. The same gates were used for the ^{12}B beam. The left panel shows CRDC1, and the right panel shows CRDC2. The events above both the horizontal and vertical lines are accepted as good events, and the rest (within the cross-hatched area) are removed from the analysis. 60

Figure 4.13: Element identification for the ^{11}Be beam. The helium element gate is shown in red. A similar gate can be made for other elements, and the same procedure is followed for the ^{12}B beam. 62

Figure 4.14: 1D helium isotope identification for the ^{11}Be beam. 64

Figure 4.15: Neutron selection for the ^{11}Be beam. The same cuts are made on the ^{12}B data. The corrected ToF is the ToF, position-corrected as if the interaction had occurred in the front and center bar of the array. Events which lie above the horizontal line and between the vertical lines are identified as neutron events. All others (within the cross-hatched area) are presumed to be cosmic muons or photons, and are removed from the analysis. . . . 65

Figure 4.16: Comparison of the CRDC1 position distributions between data and simulation for the ^{11}Be beam. The data were taken in a target-out run, where the Sweeper magnet was set to center the unreacted beam (Run 2005). The points are data and the curves are simulation. The same comparison was done for the ^{12}B (Run 2026). 72

Figure 4.17: Comparison of the CRDC angle distributions between data and simulation for the ^{11}Be beam. The data were taken in a target-out run, where the Sweeper magnet was set to center the unreacted beam (Run 2005). The points are data and the curves are simulation. The same comparison was done for the ^{12}B (Run 2026). 72

Figure 4.18: Comparison of the CRDC2 position distributions between data and simulation for the ^{11}Be beam. The data were taken in a target-out run, where the Sweeper magnet was set to center the unreacted beam (Run 2005). The points are data and the curves are simulation. The same comparison was done for the ^{12}B (Run 2026). 73

Figure 4.19: Comparison of the CRDC1 x and fragment kinetic energy distributions between data and simulation for the ^{11}Be beam. The data were taken from a chain of target-in runs. The points are data and the curves are simulation. The same comparison was done independently for the ^{12}B beam. 75

Figure 5.1: The decay energy spectrum from the ^{12}B(-3p)^{9}He reaction. 83

Figure 5.2: The likelihood maximization for the first resonance energy from the ^{12}B(-3p)^{9}He reaction. The points are the calculated likelihoods, and the black curve is a cubic spline interpolation. The red vertical lines correspond to the 1σ (stat.) error band. 83

Figure 5.3: The ^{11}Be(-2p)^{9}He decay energy at the global maximum of the coarse-grained search. The simulated parameter values are $a = -2$ fm, $\Theta = 2.5$ MeV, and a relative scale factor of 0.5. 86

Figure 5.4: A 1D projection of the log-likelihood near the global maximum of the coarse-grained search. The points are the calculated log-likelihoods, and the curve is a cubic spline interpolation to guide the eye. 87

Figure 5.5: The ^{11}Be(-2p)^{9}He decay energy at the maximum in the restricted parameter space. The points are data and the curves are simulations. The simulated parameter values are $a = -7$ fm, $\Theta = 1.5$ MeV, and a relative scale factor of 1.5. 88

Figure 5.6: A 1D projection of the log-likelihood near the maximum of the coarse-grained search, when the parameter space has been restricted to large scale factors. The points are the calculated log-likelihoods, and the curve is a cubic spline interpolation to guide the eye. 88

Figure 5.7: The 1D log-likelihood of fine-grained search around $a = -2$ fm. The points are the calculated log-likelihoods, and the curve is a parabolic fit. 90

Figure 5.8: The 1D log-likelihood of fine-grained search around $a = -7$ fm. The points are the calculated log-likelihoods, and the curve is a parabolic fit. 91

Figure 5.9: The relative velocity spectrum from the ^{12}B(-2p)^{10}Li reaction. The points are data from this work, and the curves are the simulations of the resonances from the previous work. The three resonances are shown individually in the red, green, and blue curves. The black curve is the combined simulation. 93

Figure 5.10: The ^{11}Be(-1p)^{10}Li decay energy at the global maximum of the coarse-grained search. The simulated parameter values are $a = -1$ fm, $\Theta = 1.0$ MeV, and a relative scale factor of 0.5. 94

Figure 5.11: The ^{11}Be(-1p)^{10}Li decay energy at the maximum of the restricted, coarse-grained search. The simulated parameter values are $a = -7$ fm, $\Theta = 1.0$ MeV, and a relative scale factor of 1.5. 95

Chapter 1

Introduction

1.1 The nuclear landscape

The atomic nucleus is a system of one or more nucleons (protons and neutrons), bound by the strong force. Each particular species of atomic nucleus, called a "nuclide", is characterized by its atomic number (the number of protons, Z), its number of neutrons (N), and its mass number (the number of nucleons, A). The mass number is related to Z and N via $A = Z + N$, so only two of these quantities are required to uniquely specify a nuclide. The nuclear landscape is the set of all known nuclides, plotted in the (N, Z)-plane, as shown in Figure 1.1. A nuclear system in general may contain various discrete bound states, quasi-discrete resonant states, and a continuum of scattering states. Each nuclear bound or resonant state is characterized by some set of quantum numbers, including excitation energy, angular momentum, parity, and isospin. In addition to these quantum numbers, there are a number of other observable quantities of interest, such as the half-life/energy width, electomagnetic multipole moments, decay modes, and their branching fractions. The study of these properties of bound and resonant nuclear states constitutes the field of nuclear structure physics.

Not only are the properties of individual nuclear levels of interest, but the systematic trends across the nuclear landscape are of utmost importance to forming a comprehensive understanding of nuclear structure. Nuclei are in general complicated, strongly-interacting quantum many-body systems, so in most cases, there is no simple rule that dictates how any one of these properties will evolve as a function of Z and N.

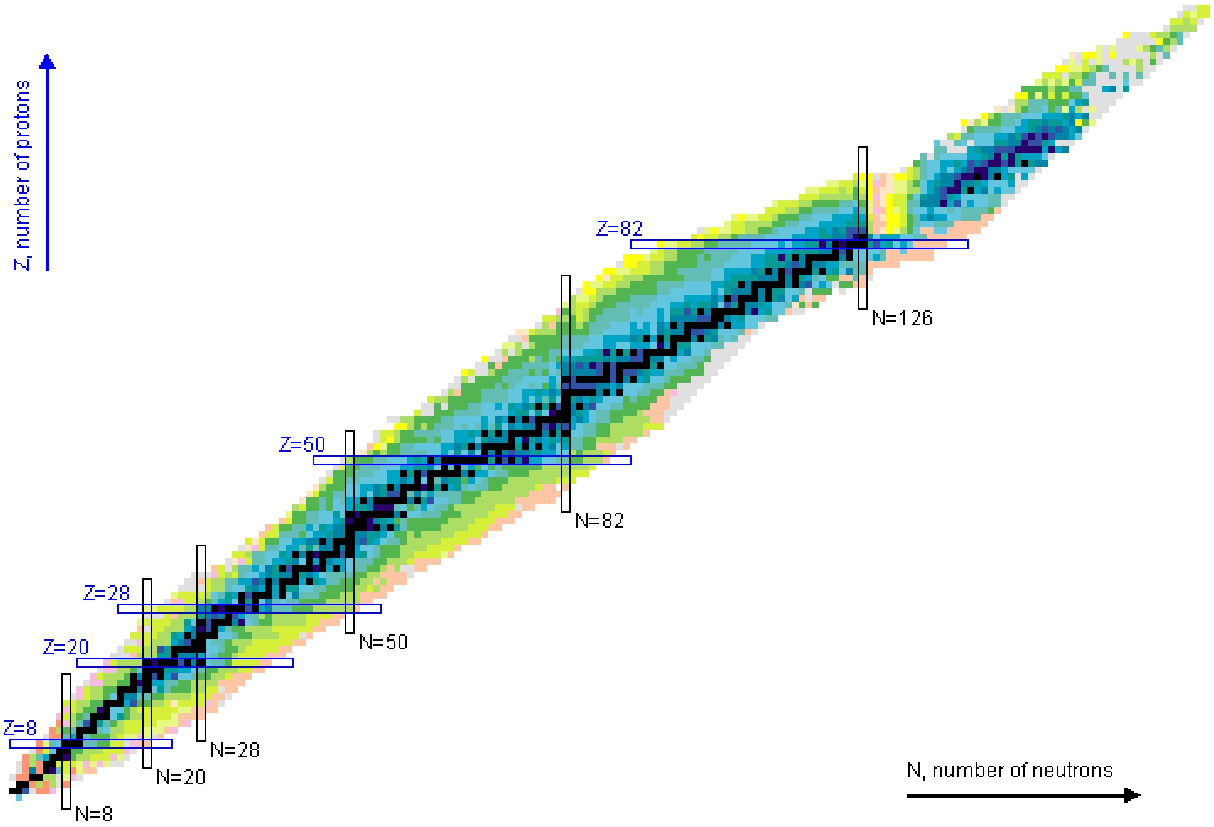

Figure 1.1: The Chart of Nuclides, from NNDC [2]. The colors indicate ground state half-lives.

Across the nuclear landscape, observed half-lives of unstable nuclides can vary from many times the current age of the universe, down to $\sim 10^{-22}$ seconds, for particle-unbound nuclides. At the extreme limit of large N/Z, there is a sharp jump in half-lives from ~ 1 ms to $\sim 10^{-18}$ ms where the neutron separation energies (the "energy cost" for removing one neutron) become negative. The longer half-lives are for particle-bound nuclides, with positive separation energies, which tend to decay by β-emission, whereas the shorter half-lives are for particle-unbound nuclides, with negative separation energies, which decay by nucleon emission. This transitional region is known as the neutron "dripline", where the neutron separation energies become negative [8]. The sharp difference in half-lives across the neutron dripline is due to the relative strengths of the weak and strong forces, at the energy scales relevant to nuclear structure. The "weakness" of the weak force means that β-decay half-lives tend to be very long compared to the characteristic timescale of the "motion" of nucleons within a nucleus ($\sim 10^{-22}$ sec).

The overarching goal of nuclear structure theory is to be able to predict all of the properties of any given nuclear state within a concise, unified framework. At present, there are many different theoretical approaches to nuclear structure, at various levels of "granularity".

At the most fundamental level, nuclear structure is dominated by strong interactions, and can be described using quantum chromodynamics (QCD) (with relatively small corrections due to the electroweak interactions). Because QCD is non-perturbative at low energies, the study of nuclei from QCD must be done on a discretized spacetime lattice, within the formalism of lattice QCD (LQCD). The fundamental degrees of freedom in an LQCD calculation are the quark fields at each lattice point, and the "gauge links" between points, which would represent the gluon fields in the continuum theory. To study a nucleus from LQCD, interpolating operators composed of quark fields coupled to the desired quantum numbers are constructed, and their vacuum expectation values are evaluated using the Feynman path integral formalism in Euclidean spacetime. In the limit of large Euclidean time, the expectation value decays exponentially with the energy of the ground state, which is simply the mass of the nucleus of interest. These so-called "baryon spectroscopy" calculations allow for the discrete nuclear energy levels to be predicted from the most fundamental description of the strong force currently available. However the ability to model nuclei from LQCD is currently limited by computational cost, so only the lightest nuclei are currently accessible with this method [9].

At the expense of a "less fundamental" approach, gains have been made in the computational ease of modeling a nucleus. Rather than choosing quarks and gluons as the fundamental degrees of freedom from which to build nuclei, effective field theories (EFTs) of hadrons can be used instead. In this case, mesons and baryons are treated as fundamental particles, and the nucleon-nucleon interaction is modeled diagrammatically as a meson exchange force [10, 11]. These EFTs can be constructed to respect the same physical symmetries as the underlying theory of QCD, and nuclei can be built "ab initio" from the nucleon-nucleon forces derived from the EFT [12]. These approaches are ultimately limited by computational cost as well, but can presently reach mass numbers significantly higher than LQCD can.

Rather than exactly solving a quantum A-body problem with complicated ab initio interactions, which may be computationally intractable for sufficiently high A, so-called "configuration interaction" (CI) methods can be used. CI methods will be discussed in detail in the next section.

For the heaviest known nuclides, even CI methods can't be used due to the computational cost, and density functional theory (DFT) must be used instead. DFT methods have been used for many years in atomic and condensed matter physics [13, 14], and have since been applied to atomic nuclei as well [15]. In these methods, rather than considering individual particle degrees of freedom, continuous densities and currents are used, and the equations for the nuclear density and the interactions are solved self-consistently. This method allows for determination of ground and excited state energies, and therefore calculations of binding energies.

The combination of these methods allows nuclear structure theorists to study nuclei from individual nucleons, all the way up to the superheavy nuclides ($Z \gtrsim 104$) [16], and even make predictions about the yet unobserved "hyperheavy" ($Z \gtrsim 126$) nuclides [17]. However rather than dividing the nuclear landscape into regions of applicability of multiple distinct theoretical frameworks, a unified approach which is computationally tractable over the entire landscape, while simultaneously maintaining a close connection to the fundamental degrees of freedom, is desired. This would arguably be the "Holy Grail" of nuclear structure theory.

1.2 The nuclear shell model

The nuclear shell model is a framework with which the time-independent Schrödinger equation is solved for a bound system of A non-relativistic nucleons by direct diagonalization of a many-body Hamiltonian. The matrix elements for a given Hamiltonian are often determined phenomenologically for a certain mass range, and the eigenvalues and eigenstates of a given shell model Hamiltonian can then be used to predict physical properties of a given nuclide within its range of applicability. The nuclear shell model is an example of a CI method, mentioned in the previous section.

The motivation for developing the nuclear shell model was the experimentally observed sudden jumps in quantities like binding energies and nucleon separation energies near certain "magic" numbers of nucleons (2, 8, 20, 28, 50, 82, etc.). Previous models, like Gamow, Bethe, and Weizsäcker's liquid drop model [18, 19], were unable to explain this behavior, which bears similarity to the behavior of atoms with closed electron shells (noble gases). If nucleons within a nucleus are arranged in shells similar to those of atomic electrons, it could explain the observed behavior. The problem then became finding an appropriate set of interactions to reproduce the experimental magic numbers.

In the late 1940's and early 1950's, it was determined by Wigner, Goeppert-Mayer,

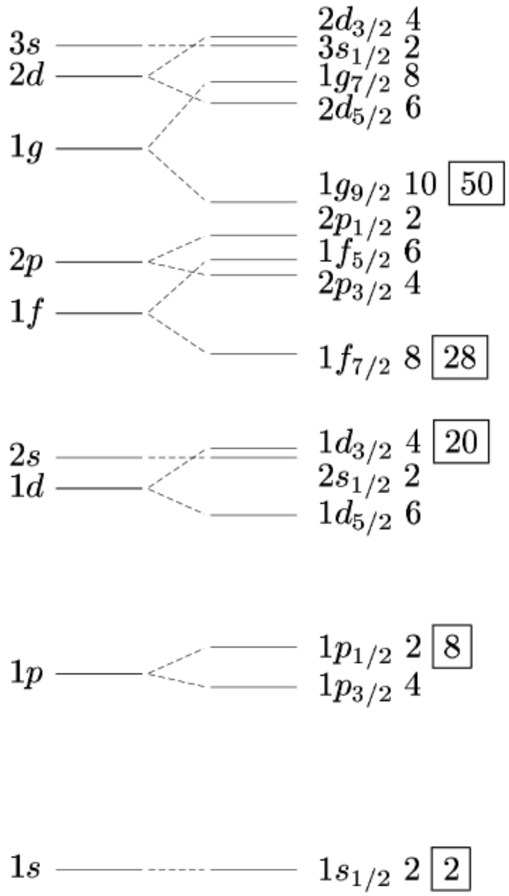

Figure 1.2: The first few single-particle orbitals in the nuclear mean field potential, from Wikipedia [3].

Jensen, and Haxel that a Woods-Saxon plus spin-orbit potential would produce the correct experimental magic numbers between single-particle nucleon orbitals [20, 21], a discovery that would go on to earn the 1963 Nobel Prize in physics. An energy level diagram for the single-particle orbitals in this potential is shown in Figure 1.2. The physical intepretation is that a valence nucleon primarily feels a “mean-field” potential from all of the nucleons in the core, in addition to “residual” interactions with each of the other valence nucleons. Then in order to calculate observable quantities from this model, all that is necessary are the appropriate parameters for the mean-field potential, and a model for the residual interactions. Many-body wavefunctions can be constructed in the basis of Slater determinants of single-particle orbitals in the mean-field potential, and corrections to the wavefunctions and energies can be calculated taking into account the residual interactions. Because the residual interactions are not zero in general, the mean-field potential does not encompass all of the physical interactions within the nucleus, and Slater determinants of single-particle orbitals (also called "configurations") are not truly eigenstates of the full nuclear Hamiltonian. So nuclear states with definite energies are in general linear combinations of shell model configurations. This is known as "configuration mixing".

Clearly this method should be expected to work best near magic numbers, where the proton and neutron valence shells are fully-occupied, and there are no residual interactions. As particles or holes are added, and the system moves away from closed-shell configurations, the residual interactions become more important, and the mean-field description begins to break down. Near a closed shell the nuclear Hamiltonian would be expected to be almost diagonal in the basis of shell model configurations, but away from closed shells this will not be the case. Away from closed shells, interesting collective phenomena like nuclear vibrations and rotations emerge. Excited states will not necessarily consist of a single valence nucleon promoted into a higher single-particle orbital, but instead many nucleons can participate in the excitation together. A topic that is currently of great interest in nuclear structure physics is the evolution of shell structure away from stable and near-stable nuclides. This topic will be discussed in the next section.

1.3 Shell evolution and inversion

The shell model has been remarkably successful in predicting the structure of nuclei near closed shells however in recent decades, emphasis in nuclear structure physics has moved toward nuclei away from closed shells. It has been shown that the structure of nuclei evolves in interesting and nontrivial ways, due to a combination of effects. For example, the energies of single-particle configurations can evolve along an isotopic or isotonic chain, and even rearrange in order. So in nuclei far from stability, the levels predicted by considering mean-field configurations may be in the wrong order. This phenomenon is called "shell inversion", because the mean-field levels are "inverted" relative to the true level scheme. The primary effects driving this structural evolution appear to be many-body forces [22], the tensor force [23], and close to the driplines, continuum effects [24]. Regions of the chart of nuclides where inversion has been observed (depicted in Figure 1.3) are known as "islands of inversion" [25]. The lightest island of inversion contains some of the $N = 7$ isotones, which are the subject of this dissertation.

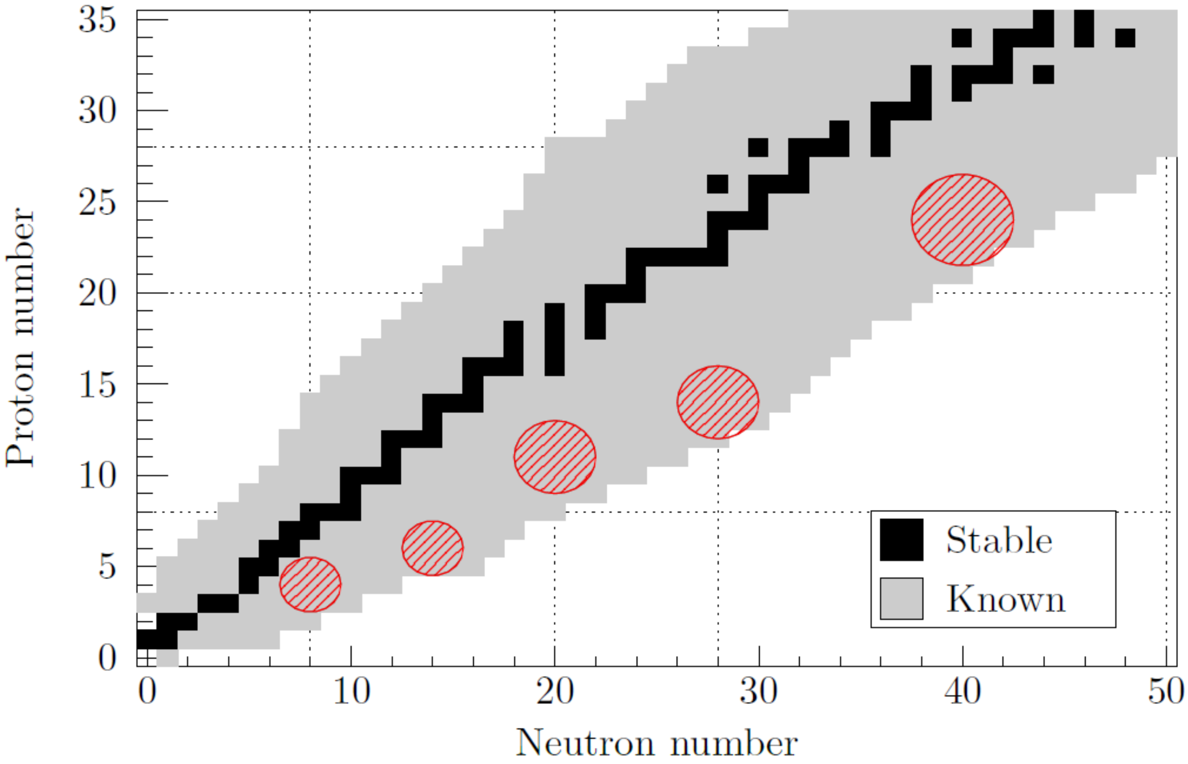

Figure 1.3: The chart of nuclides, with the observed regions of inversion highlighted, from the dissertation of J. K. Smith [1].

1.4 Previous experiments with the $N = 7$ isotones

There has been a great deal of discussion in previous works about the structural evolution of single-particle neutron orbitals along the $N = 7$ isotone. Given the proximity to the "light island of inversion" and the well-known case of the 2n-halo nucleus ^{11}Li, it's a topic of great interest in the study of the structure of light nuclei. It's been suggested that the presence or absence of inversion in ^{10}Li may shed light on the formation of the 2n halo in ^{11}Li [26, 27, 28, 29, 30]. It has also been indicated that presence or absence of inversion in ^{9}He could put constraints on a low-lying "double halo"-like ground state of ^{10}He [31, 32].

In a mean-field approach, the first six neutrons of an $N = 7$ nucleus completely fill the $\nu(1s_{1/2})$ and $\nu(1p_{3/2})$ orbitals, leaving the single valence neutron to occupy a $\nu(1p_{1/2})$ orbital. However it is known that the lowest-Z particle-bound isotone, ^{11}Be, has an inverted shell structure due a strong $\nu(2s_{1/2})$ occupation, evident from its well-known neutron halo. Calculations have suggested that this inverted neutron structure could be shared by the more proton-deficient, neutron-unbound isotones, ^{9}He and ^{10}Li [33, 34, 32], but there is still some theoretical disagreement [35].

Previous experiments have yielded contradictory results about the low-lying structure of ^{9}He [36, 37, 38, 39, 40, 41, 42, 43, 44, 45, 46, 47]. Early experimental works [36, 37, 38, 39] relied on concurrent nuclear structure theory to make a spin and parity assignment of $\frac{1}{2}^{-}$ to the observed ground state resonance. In the work of L. Chen, *et al.* [40], it was first suggested that a low-lying s-wave virtual state had been observed with scattering length $a_s < -10$ fm. However this experiment was not able to simultaneously constrain other resonances to confirm parity inversion. Subsequent experiments using transfer reactions to populate ^{9}He directly [42, 43, 46], or studying isobaric analog states in ^{9}Li [41, 47] have not painted a consistent picture of the structure of ^{9}He. Concise summaries of the experimental results as of 2013 and 2015 are given by T. Al Kalanee, *et al.* [46] and H. T. Forture [48], respectively.

^{10}Li has also had a long and controversial experimental history [49, 50, 51, 52, 53, 54, 55, 56, 57, 39, 58, 59, 60, 61, 62, 63, 64, 65, 66, 67]. Some experiments have provided evidence for a low-lying s-wave neutron resonance in ^{10}Li [49, 50, 51, 53, 54, 57, 39, 59, 60, 62, 63], while others have not [52, 55, 56, 58, 61, 64, 65, 66, 67]. For both ^{9}He and ^{10}Li, many of the previous experimental works suffer from poor statistics and high signal-to-background ratios, making the results and conclusions somewhat uncertain.

Chapter 2

Theoretical Background

2.1 s-wave ($\ell = 0$) lineshape

This section will provide a simplistic derivation of the lineshape for decays via the emission of an s-wave neutron. The treatment here will follow what was done in Refs. [57, 68]. We are interested in the transition matrix element between a loosely-bound neutron state from a neutron-halo beam, to an s-wave continuum state, upon the sudden removal of some number of protons. The initial core-neutron state will be modeled by a spatial wavefunction of the form:

$$\Psi_0(\vec{R}, \vec{r}) = f(\vec{R})\frac{e^{-kr}}{r} \tag{2.1}$$

where $\vec{R}$ is the coordinate vector of the core and $\vec{r}$ is the coordinate vector of the loosely-bound neutron relative to the core. The parameter $k \equiv \sqrt{2\mu\varepsilon_b}$, where μ is the reduced mass of the core-neutron system and ε_b is the neutron separation energy of the beam nuclide.

In the final state, the neutron wavefunction will take the form of an $\ell = 0$ spherical wave of the form:

$$\psi_p(\vec{r}) \sim \frac{\sin(pr + \delta)}{pr} \tag{2.2}$$

where p is the relative momentum of the neutron and the fragment in the final state ($\hbar = 1$), and δ is the s-wave phase shift. The matrix element that we are interesting in caclulating is then:

$$M(\vec{R}, p) = \int d^3r \; \psi_p^*(\vec{r})\Psi_0(\vec{R}, \vec{r}) \tag{2.3}$$

Substituting in the forms of the wavefunctions and carrying out the integration, the matrix element becomes:

$$M \sim f(\vec{R}) \frac{\cos\delta - \frac{k}{p}\sin\delta}{k^2 + p^2} \tag{2.4}$$

We now convert this into an energy-differential cross section:

$$\frac{d\sigma}{dE} \propto p|M|^2 \propto \frac{p}{(k^2+p^2)^2}\left[\cos\delta - \frac{k}{p}\sin\delta\right]^2 \tag{2.5}$$

Finally, we parametrize the phase shift in terms of the effective range approximation:

$$p\cot\delta \approx -\frac{1}{a} + \frac{1}{2}r_0p^2 \tag{2.6}$$

The previous two equations determine the s-wave lineshape used for this analysis. There are two unknown parameters: the scattering length (a) and the effective range (r_0). However it can be shown that the shape of the distribution is very insensitive to the value of the effective range over a physically reasonable range ($\sim 2 - 8$ fm), so this parameter is usually fixed to an arbitrary value within that range [68]. For this analysis, an effective range of 3 fm was used. This leaves only the scattering length as an undetermined parameter, so it was used as the single fitting parameter for s-wave decays in this analysis.

This lineshape in the limit where $a \to 0$, corresponding to zero final state interactions between the continuum neutron and the fragment, will be referred to in this work as a "correlated background". Examples of the s-wave lineshape are plotted in Figure 2.1.

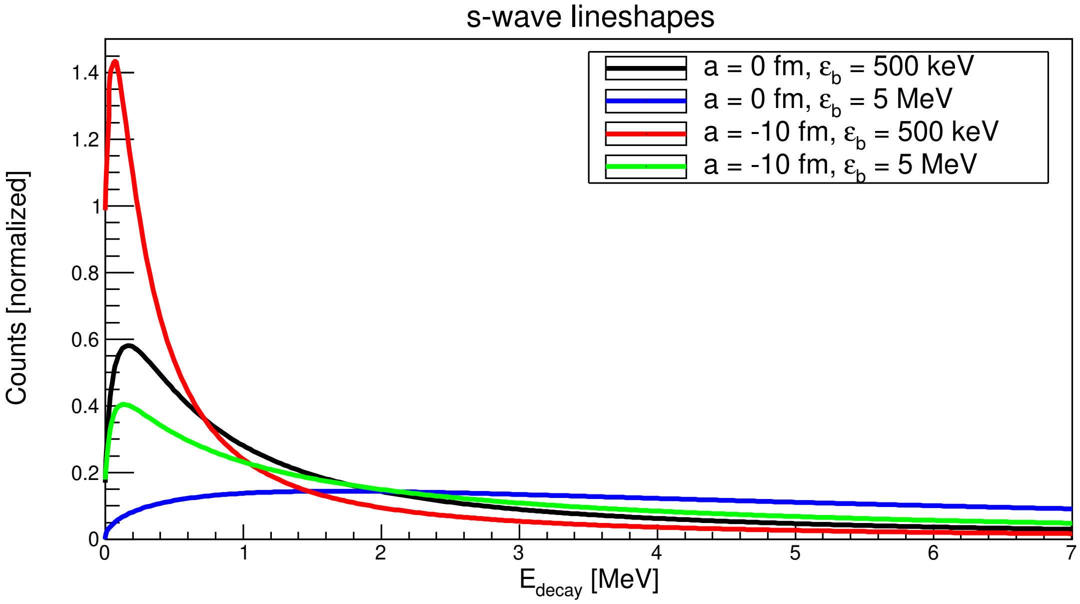

Figure 2.1: Normalized s-wave lineshapes for various values of the scattering length (a) and binding energy (ε_b) parameters. The effective range parameter was fixed at 4 fm.

2.2 Energy-dependent Breit-Wigner ($\ell > 0$) lineshape

This section will provide a derivation of the lineshape for decays via the emission of a neutron with $\ell > 0$, using R-matrix theory, following the treatment in Reference [69]. Only the minimum amount of R-matrix theory needed to derive the result will be covered. For a more comprehensive treatment, the reader should consult the textbook by Thompson and Nunes [69], or the review article by Lane and Thomas [70]. In this work, we are interested in decays via neutron emission immediately following direct proton removal reactions. Within the R-matrix formalism, the neutron emission can be treated as inelastic scattering. For a transition from some entrance channel α to some exit channel β, the R-matrix can be written as a sum over energy poles λ:

$$R_{\beta\alpha} = \sum_{\lambda} \frac{\gamma_{\lambda\alpha}\gamma_{\lambda\beta}}{\varepsilon_{\lambda} - E} \tag{2.7}$$

where E is the bombarding energy and ε_{λ} is the energy associated with the pole λ.

Then the transition S-matrix element can be written in terms of the R-matrix as:

$$\mathbf{S} = \mathbf{t}^{1/2} \frac{\mathbf{H}^{-} - a\mathbf{R}(\mathbf{H}'^{-} - \eta\mathbf{H}^{-})}{\mathbf{H}^{+} - a\mathbf{R}(\mathbf{H}'^{+} - \eta\mathbf{H}^{+})} \tag{2.8}$$

where $t_{\alpha} \equiv \hbar^2/2\mu_{\alpha}$, $\mathbf{H}^{\pm}$ are diagonal matrices with the Hankel functions on the diagonals, and η is the logarithmic derivative of the R-matrix evaluated at the channel radius a. The Hankel function of a given partial wave is given by a linear combination of regular and irregular Coulomb functions, $H_{\ell}^{\pm} = G_{\ell} \pm iF_{\ell}$, and the Coulomb functions are the solutions to the time-independent radial Schödinger equation with a repulsive Coulomb potential.

We now define the penetrability factor:

$$P_{\alpha} \equiv \frac{k_{\alpha}a}{F_{\alpha}^2 + G_{\alpha}^2} \tag{2.9}$$

and the $\mathbf{L}$ matrix:

$$L_{\alpha} \equiv \frac{H_{\alpha}'^{+}}{H_{\alpha}^{+}} - \eta \tag{2.10}$$

and the $\mathbf{\Omega}$ matrix:

$$\Omega_{\alpha} \equiv e^{i\phi_{\alpha}},\ \tan\phi_{\alpha} \equiv -\frac{F_{\alpha}}{G_{\alpha}} \tag{2.11}$$

With a similarity transformation to put the S-matrix into symmetric form, it can be written as:

$$\tilde{\mathbf{S}} \equiv \mathbf{v}^{1/2}\mathbf{S}\mathbf{v}^{-1/2} = \boldsymbol{\Omega}\Big[1 + 2i\mathbf{P}^{1/2}\Big(1 - a\mathbf{R}\mathbf{L}\Big)^{-1}\mathbf{R}\mathbf{P}^{1/2}\Big]\boldsymbol{\Omega} \tag{2.12}$$

where $\mathbf{v}$ is a diagonal matrix with elements $v_\alpha = \hbar k_\alpha/\mu_\alpha$.

Assuming there are only two relevant channels, the elements of the transformed S-matrix are given explicitly by:

$$\tilde{S}_{\beta\alpha} = e^{i\phi_\alpha}\left[\delta_{\beta\alpha} + \frac{2iP_\alpha^{1/2}\gamma_\alpha\gamma_\beta P_\beta^{1/2}}{(\varepsilon_\lambda - E)(1 - aR_{11}L_1 - aR_{22}L_2)}\right]e^{i\phi_\beta} \tag{2.13}$$

We now define the partial widths:

$$\Gamma_\alpha \equiv 2\gamma_\alpha^2 P_\alpha \tag{2.14}$$

and the total resonance width:

$$\Gamma \equiv \sum_\alpha \Gamma_\alpha \tag{2.15}$$

The expression for the S-matrix elements simplifies to:

$$\tilde{S}_{\beta\alpha} = e^{i\phi_\alpha}\left[\delta_{\beta\alpha} - \frac{i\Gamma_\alpha^{1/2}\Gamma_\beta^{1/2}}{E - E_r + i\Gamma/2}\right]e^{i\phi_\beta} \tag{2.16}$$

where the total resonance energy E_r is defined by:

$$E_r \equiv \varepsilon_\lambda - \gamma_1^2 S_1^0 - \gamma_2^2 S_2^0 \tag{2.17}$$

From elementary multi-channel reaction theory, the relationship between the cross section and the S-matrix element is given by:

$$\sigma_{\beta\alpha} = \frac{\pi}{k_\alpha^2} \frac{2J+1}{(2I_p+1)(2I_t+1)} |\tilde{S}_{\beta\alpha}|^2 \tag{2.18}$$

where the subscripts “p” and “t” refer to “projectile” and “target”, respectively. Explicitly plugging in the S-matrix element gives:

$$\sigma_{\beta\alpha} = \frac{\pi}{k_\alpha^2} \left(\frac{2J+1}{(2I_p+1)(2I_t+1)} \right) \left[\frac{\Gamma_\alpha \Gamma_\beta}{(E-E_r)^2 + \Gamma^2/4} \right] \tag{2.19}$$

This is the familiar functional form of an isolated Breit-Wigner resonance, however the quantity E_r is not exactly equal to the pole energy ε_λ. Instead, it’s the pole energy, shifted due to the couplings between channels. This dependence can instead be absorbed into an “energy-dependent width”, and the cross section can be written explicitly in terms of the pole energy. This form was chosen to illustrate the similarity to a standard Breit-Wigner lineshape. The name of this lineshape is an “energy-dependent Breit-Wigner”, or “asymmetric Breit-Wigner” distribution. The final form, in terms of the pole energy and total width is:

$$\sigma_\ell(E;\varepsilon_\lambda,\Gamma_\ell) \propto \frac{\Gamma_\ell}{\Big(\varepsilon_\lambda - E + \Delta_\ell(E;\varepsilon_\lambda,\Gamma_\ell)\Big)^2 + \frac{1}{4}\Gamma_\ell^2} \tag{2.20}$$

This is the lineshape used to fit decays with $\ell > 0$ in this analysis. The free parameters are the pole energy and the total width.

Chapter 3

Experimental Techniques

This chapter provides an overview of the experimental setup in the N2 vault of the National Superconducting Cyclotron Laboratory (NSCL) at Michigan State University (MSU).

3.1 Primary beam

The first step in producing the two secondary beams of interest is to produce a primary beam for in-flight projectile fragmentation. The primary beam of 120 MeV/u ^{18}O is provided by the CCF [71]. Figure 3.1 depicts everything necessary to produce a fast radioactive ion beam for delivery to the experimental area. The stable primary beam particles originate in an electron-cyclotron resonance (ECR) ion source, where electron cyclotron motion in a plasma is resonantly excited using microwaves. This causes heating of the plasma, and an increased degree of ionization. The ^{18}O ions are then extracted from the ion source and delivered to the K500 cyclotron for the first stage of acceleration. After being accelerated to $\sim$ 10 MeV/u in the K500 cyclotron, the primary beam is transported and injected into the K1200 cyclotron for the second stage of acceleration. There is a stripper foil inside the K1200 that increases the charge state of the primary beam upon its injection into the K1200 to aid with acceleration. After the second stage of acceleration, with a final kinetic energy of 120 MeV/u, the primary beam is directed onto a beryllium production target. Projectile fragmentation of a beam particle of mass number A_p will produce every bound nucleus with

$A < A_p$ according to some stastical distribution. The task now becomes separating out the fragments of interest in order to deliver a relatively pure secondary beam to the experimental area.

For the ^{11}Be secondary beam, the production target had a thickness of 2938 mg/cm^2, and for the ^{12}B secondary beam, the production target had a thickness of 3523 mg/cm^2.

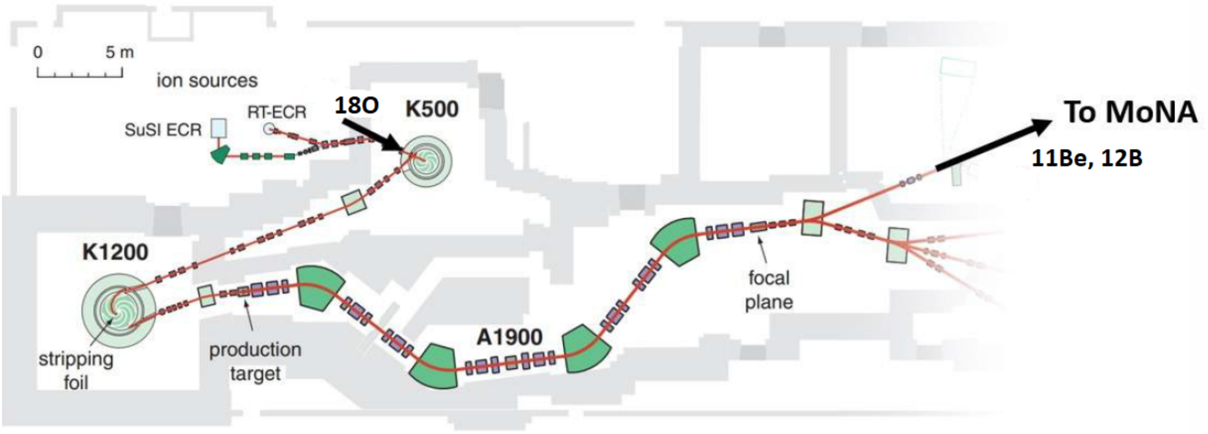

Figure 3.1: The Coupled Cyclotron Facility and the A1900 fragment separator.

3.2 Secondary beams

In order to separate out a desired species for a secondary beam, the A1900 fragment separator [72, 73] is used. The A1900 is a series of magnets consisting for four main dipoles and eight quadrupole triplets. There are three intermediate images where separation of unwanted fragments occurs, and finally an achromatic focus in the A1900 focal plane, where the beam is then directed into one of the various experimental areas. The main dipoles are tuned to the magnetic rigidity ($B\rho = p/q$) of the secondary fragment of interest. The dipole magnets introduce a dispersion to the beam (a correlation between the deviation from central rigidty and horizontal position). At Image 1, the further off-rigidity a particle is, the further it is from the beam axis. A set of horizontal slits with controllable width are then used to physically remove particles that are sufficiently off from the desired $B\rho$. After Image 1, the beam enters the second dipole and is directed toward a wedge at Image 2, which provides differential energy loss according to Z^2. The third dipole disperses and directs the beam to Image 3, where a second set of slits is used to remove more off-rigidity particles from the beam. Finally the fourth dipole exactly cancels the remaining dispersion and the filtered secondary beam is brought to an achromatic focus in the A1900 focal plane, where there are various detectors and diagnostics available. The quadrupole triplets throughout the A1900 are used for beam focusing in both the horizontal and vertical directions. By the end of the A1900 separator, the ^{11}Be beam was 85% pure, with the main contaminant being ^{14}C ($\sim$ 15%), and the ^{12}B beam was $\sim$ 99% pure.

3.3 N2 vault

This section provides an overview of the experimental setup witin the N2 vault (Fig. 3.2). Properties of the secondary beams upon delivery to the experimental vault are summarized in Table 3.1. Once the beam is delivered to the vault, it impinges onto a reaction target in which the unbound nuclides of interest are produced. The reaction target used with both secondary beams was a 188 mg/cm^2 of beryllium.

Following the reactions in the target, the fragments enter the Sweeper magnet (discussed in Section 3.3.1, where their trajectories are bent horizonally into a vacuum chamber containing multiple charged particle detectors. The vacuum chamber contains two Cathode-Readout Drift Chambers (CRDCs) [74], an ionization chamber, a thin BC-404 scintillator, and a CsI(Na) hodoscope. The CsI(Na) hodoscope was not used for this analysis, but the rest of the charged particle detectors will be described in detail in Section 3.3.2.

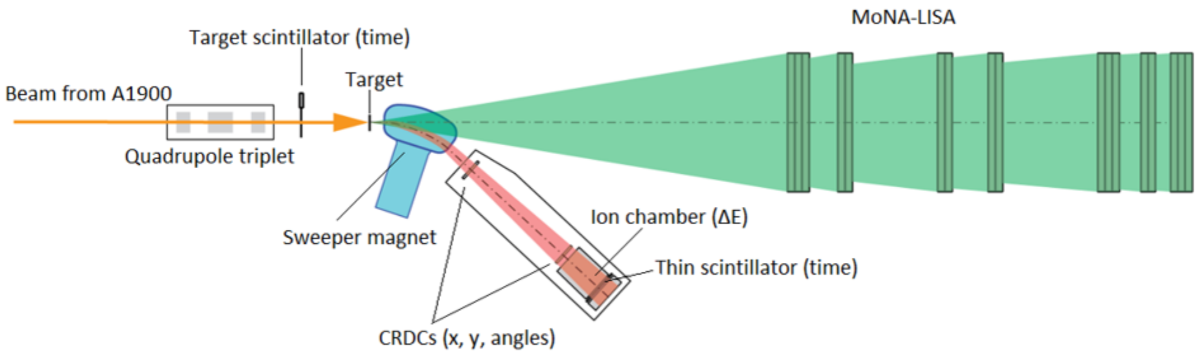

Figure 3.2: The N2 vault experimental layout.

Table 3.1: Estimated secondary beam parameters.

Beam	Energy [MeV/u]	Rate [pps]	Purity [%]
^{11}Be	44	2×10^5	85
^{12}B	45	4×10^5	99

The prompt neutrons emitted from the unbound nuclide travel, unaffected by the Sweeper magnet, across a ~ 6 meter flight path to MoNA-LISA, an array of 272 (10 cm) × (10 cm) × (2 m) BC-408/EJ-200 scintillator bars, with a photomultiplier tube (PMT) on each end [75]. The neutron detectors will be described in detail in Section 3.3.3.

With the combination of the charged particle and neutron detector arrays, the full four-momentum vector of both the fragment and neutron can be determined for each valid event.

3.3.1 Sweeper magnet

The Sweeper magnet is a large-gap dipole superconducting electromagnet used to sweep charged reaction products and unreacted beam out of the path of the neutrons. The vertical gap has a full height of 14 cm in order to accomodate the neutron cone between the target location and the front face of MoNA-LISA. The Sweeper has a maximum magnetic rigidity of 4 Tm, with a bending radius of about 1 meter, and a bending angle of 43.3°. The magnetic field inside the Sweeper gap is monitored using a Hall probe, and the details of the shape of the magnetic field have been characterized in previous works [76, 77, 78]. The Sweeper field is controlled by directly setting the current that flows through the superconducting coils.

To center the trajectories of the ^{11}Be and ^{12}B secondary beams, the Sweeper current was set to 211 Amps ($B\rho = 2.639$ Tm) and 173 Amps ($B\rho = 2.320$ Tm), respectively. To center the ^{8}He decay products in the production setting, the current was set to 355 Amps ($B\rho = 3.776$ Tm).

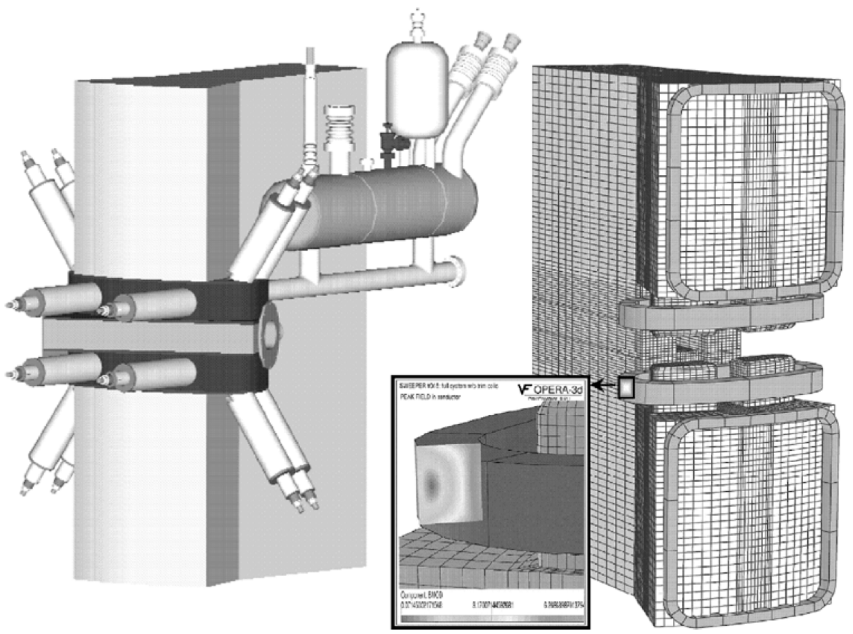

Figure 3.3: A schematic drawing of the Sweeper magnet, from Reference [4]. Both the superconducting Sweeper coils (horizontal) and normal-conducting trim coils (vertical) are shown in the diagram on the right.

The side of the Sweeper magnet is also fitted with two normal-conducting trim coils, to help cancel the fringe field outside the magnet. It has been shown in previous works that these coils have negligible effect on the field within the gap. The trim coil current was set to 200 Amps during this experiment. A schematic illustration of the Sweeper magnet is shown in Figure 3.3.

3.3.2 Charged particle detectors

There are various charged particle detectors positioned along the path of the secondary beam and fragments whose signals are used in the analysis, beginning at the A1900 extended focal plane (XFP), and ending with a suite of detectors in the vacuum chamber just downstream of the Sweeper magnet. The A1900/XFP scintillator, target scintillator, and the “thin” scintillator are all used for timing (the target and thin scintillators provide charge signals as well, but they are not used in this analysis). The CRDCs provide transverse positions (x and y) at two different locations in z (separated by about 1.55 meters), allowing for the determination of transverse angles. The ionization chamber detects energy loss as the fragments traverse its gaseous active volume. There is also a thick CsI(Na) scintillating hodoscope at the end of the Sweeper vacuum chamber for total energy deposition, but it was not needed for this analysis. Each detector system will be described in detail in the following sub-sections.

3.3.2.1 Timing scintillators

Various plastic scintillators are used in this analysis to extract timing information from charged ions. Specifically, there are the A1900 extended focal place (XFP), target, and thin scintillators. All of these detectors are organic scintillators optically coupled to photomultiplier tubes (PMTs). The XFP and target scintillators are made of BC-404 with thicknesses of 1000 μm and 420 μm, respectively. The thin scintillator is a 55 cm × 55 cm × 5 mm block of EJ-204 with four PMTs attached to it, one on each corner, coupled to the scintillator via light guides. The PMTs are named “Left Up”, “Right Up”, “Right Down”, and “Left

Down", corresponding to their locations. The thin scintillator PMTs are biased to 1260 V, 1290 V, 1380 V, and 1260 V, respectively, and the target scintillator PMT is biased to 1500 V. A diagram of the thin scintillator is given in Figure 3.4.

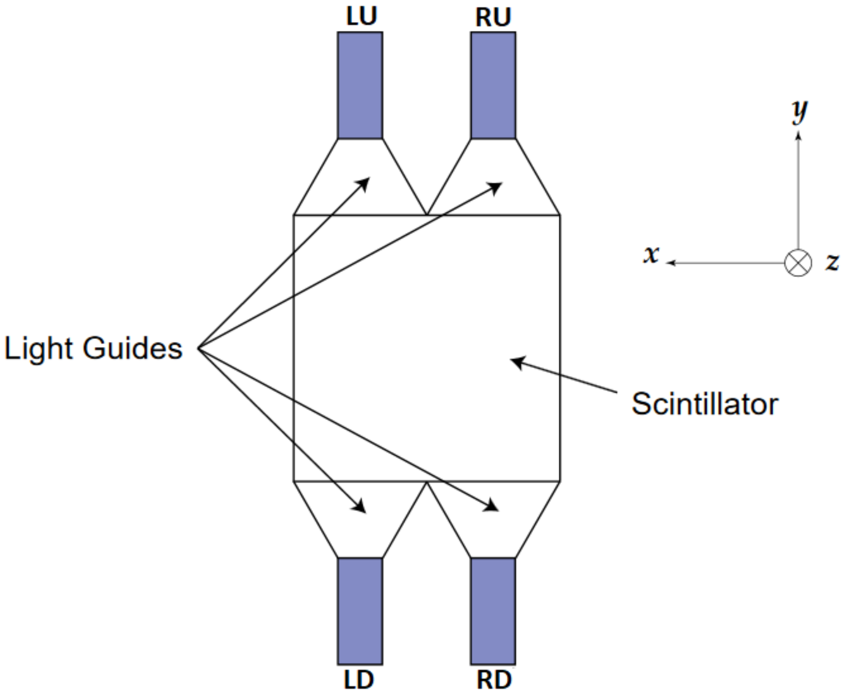

Figure 3.4: A schematic drawing of the thin scintillator. Adopted and modified from Reference [5].

3.3.2.2 Cathode Readout Drift Chambers

This work involved two Cathode Readout Drift Chamber (CRDC) detectors, separated by 1.55 meters. CRDCs are gas-filled detectors used for tracking of charged fragments. The active area of each detector is 30 cm × 30 cm, and the active gas is a mixture of 20% isobutane and 80% CF_4, at a pressure of 40 Torr. Inside each CRDC, a drift voltage of 1000 V is applied. When an ion traverses the detector, it creates some ionization in the active gas. The freed electrons then drift along the direction opposite the drift electric field, towards a

Frisch grid. Beyond the Frisch grid is a horizontal anode wire, biased to 1150 V, which serves to create an electron avalanche. Parallel to the anode wire, there is a segmented plane of 2.54 mm cathode pads. The charge distribution induced on the pads will provide information about the horizontal (x) coordinate of the incident ion, and the drift time of the electrons to the anode will profive information about the vertical (y) coordinate of the incident ion. A more detailed description of the CRDC detectors can be found in Refs. [74, 6], and a schematic drawing is shown in Figure 3.5.

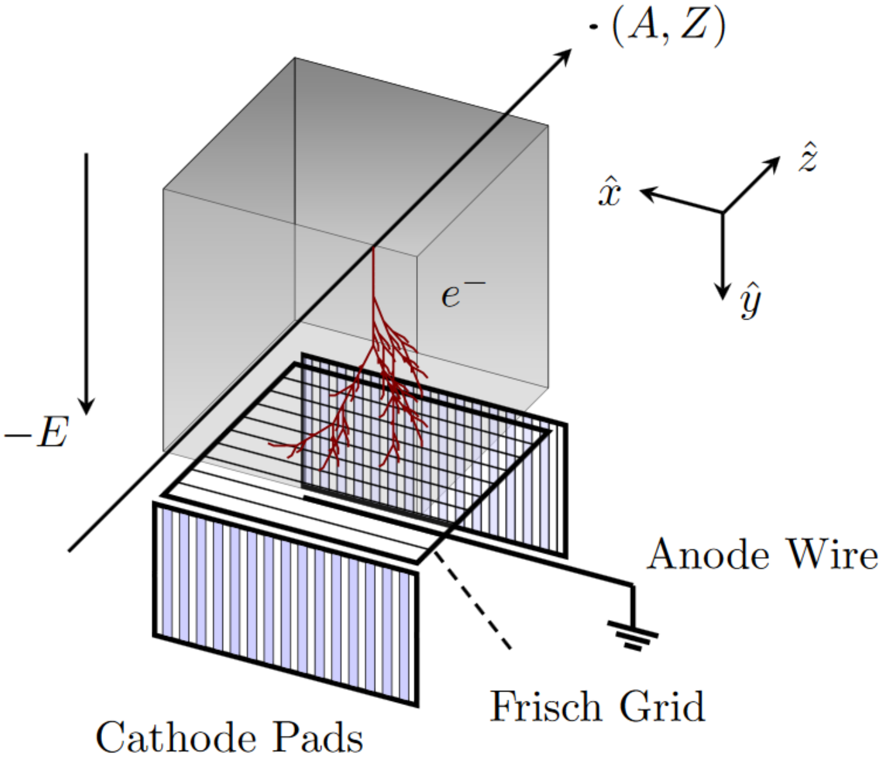

Figure 3.5: A schematic drawing of a CRDC, from Reference [6].

3.3.2.3 Ion chamber

The ion chamber is similar to the CRDCs, but it is used for particle identification (PID) rather than tracking. The ion chamber is segmented into 16 pads in the longitudinal (z) direction. The active gas is P10, with an operating pressure of 500 Torr. The drift voltage is set to 1000 V, and the anode voltage is set to 200 V. Similarly to the CRDCs, ionization in the active gas leads freed electrons inducing a charge on the pads. The pad charge signals are pre-amplified and processed through peak-sensing analog-to-digital converter (ADC) circuits. The combined signal amplitude from all of the pads is proportional to the energy loss of the incident ion as it passes through the active gas. A diagram of the ion chamber is shown in Figure 3.6.

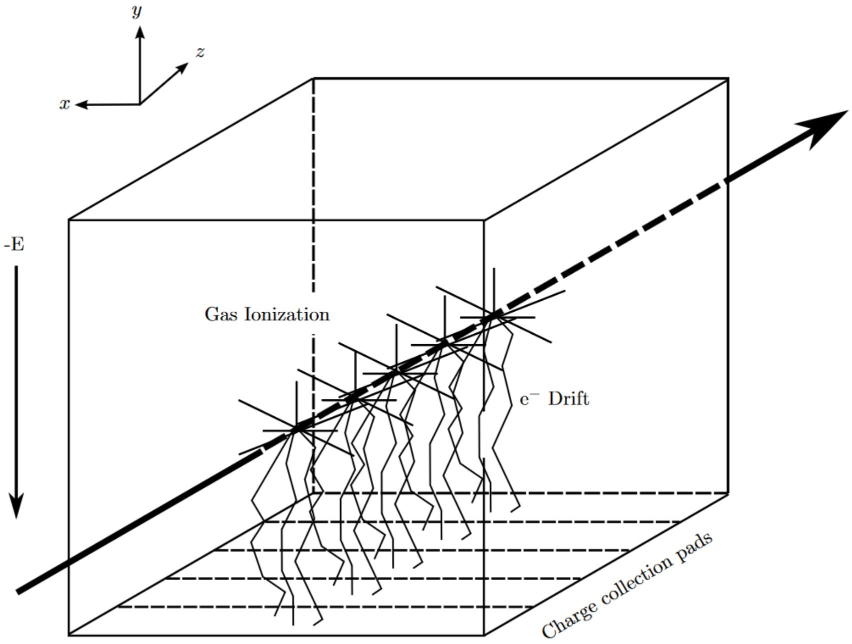

Figure 3.6: A schematic drawing of the ion chamber, from Reference [1].

3.3.3 Neutron detectors

The neutron detectors used in this analysis were the bars of the MoNA (Modular Neutron Array) and LISA (Large-area multi-Institutional Scintillator Array) arrays [75]. The combined MoNA-LISA array consists of 272 plastic scintillator bars (BC-408 for MoNA and EJ-200 for LISA). Each bar has dimensions of 10 cm × 10 cm × 2 m, and an optically-coupled PMT on each end (Photonis XP2262/B for MoNA and Hamamatsu R329-02 for LISA). The bars are wrapped with reflector, and then with black tape in order to enhance light transmission inside the bar, and prevent external light from leaking in and corrupting the output signals. A schematic of a bar is shown in Figure 3.7.

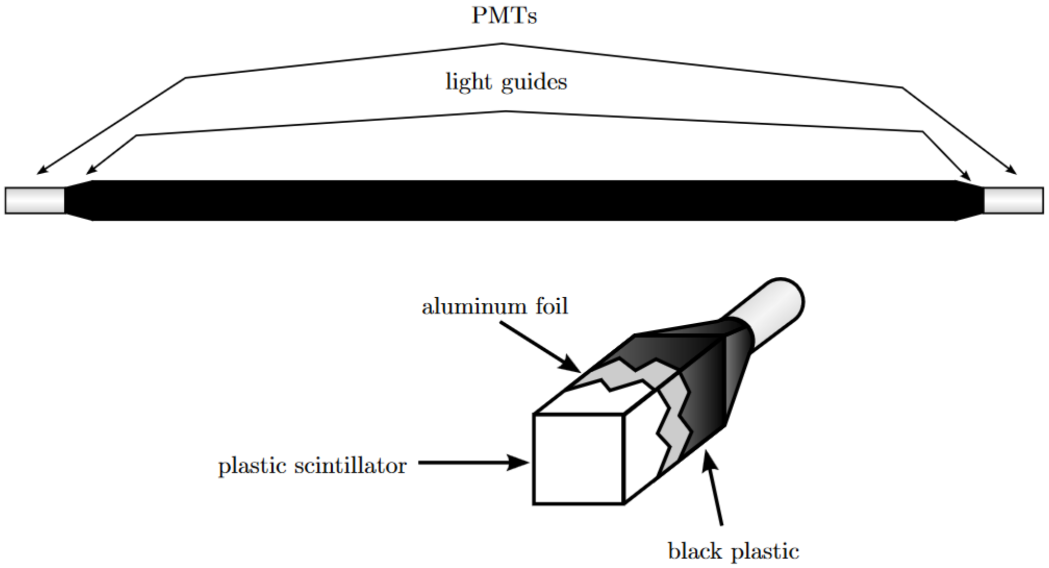

Figure 3.7: A schematic drawing of a single MoNA-LISA bar, from Reference [1].

In this experiment, the bars were stacked into 17 “layers”, each 16 bars high. All of the detectors were aligned with their centers at 0° from the beamline. Layers A through H of MoNA were stacked on a single table (Layer I was located at Los Alamos National Laboratory for detector characterization experiments). LISA was segmented into two separate tables, consisting of Layers J - M (LISA I) and Layers N - R (LISA II), respectively. In order of increasing z distance from the target position, the tables were ordered: LISA II, LISA I, MoNA. The layout of the bars and layers of MoNA-LISA is shown in Figure 3.8.

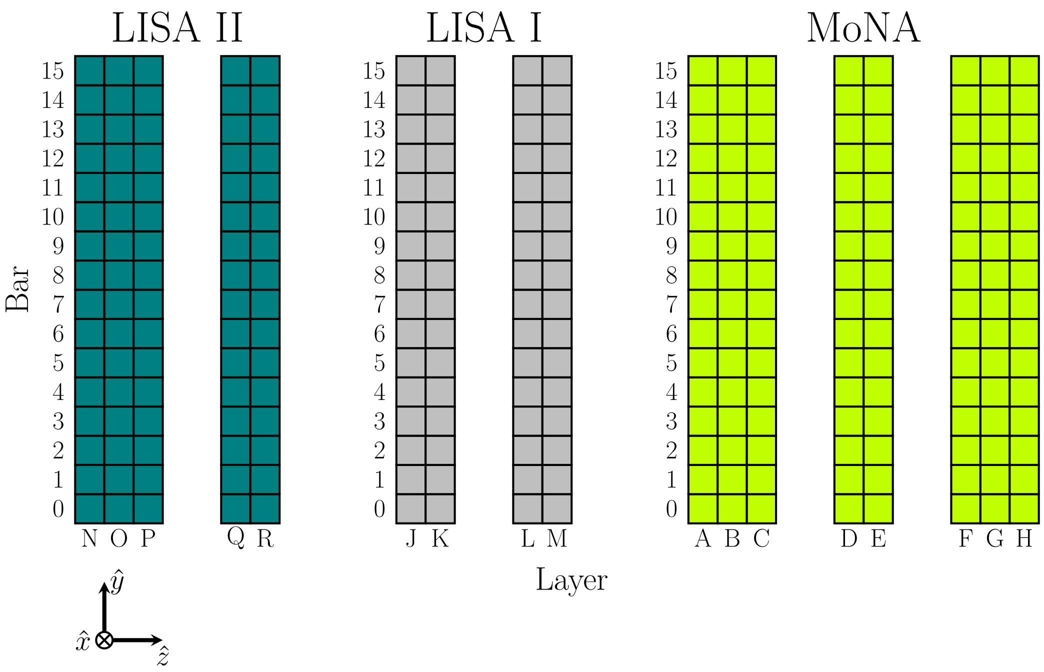

Figure 3.8: The layout of the tables, layers, and bars of MoNA-LISA.

Each PMT has three feedthroughs: an HV supply input, an anode output, and a dynode output. The anode signal is used for timing pickoff, and the dynode signal is used for measuring light output in the scintillator. The important physics comes with the timing signals, while the light output signal is optionally used to enhance the neutron event selection.

The segmentation of the array allows for localization of neutron hits in both the vertical (y) and depth (z) directions. In order to localize the hits along the length of the bars (x), the difference between the timing signals of the PMTs on each end is used. The average of the two timing signals, measured relative to the common stop (the target scintillator) gives the time-of-flight of the neutron from the target to the hit in the neutron array. Both the 3D position and the time-of-flight for each neutron hit are recorded, so this fully determines the neutron four-momentum, assuming it originated from the target position.

3.3.4 Electronics and DAQ

3.3.4.1 Hardware

The MoNA-LISA-Sweeper DAQ hardware has been thoroughly explained in previous dissertations (Refs. [76, 79, 80, 1, 6, 81, 5]), but the main points will be highlighted here. The three subsystems (MoNA, LISA, and Sweeper) each have their own independent acquisition hardware, connected by the "Level 3" logic system, which generates a system trigger that is sent to each of the individual subsystems and a 64-bit timestamp unique to each event. In this experiment, the system trigger comes from the Thin Left Up PMT. The logic for this experimental setup is handled by field-programmable gate arrays (FPGAs) in Xilinx Logic Modules (XLMs). The logic hardware is separated into three "Levels". Levels 1 and 2 are used to determine whether a valid event (valid time signals from both PMTs of a given bar) was detected in MoNA-LISA. Level 3 contains a clock which is counting whenever the system is not busy, and the coincidence logic between MoNA-LISA and Sweeper.

This experiment was run in Sweeper singles mode, meaning that the whole system is triggered by the Sweeper, and read out whether or not there is a coincident event in MoNA-LISA. When Level 3 receives a signal from the Thin Left Up detector, a coincidence gate is opened, and the system waits for a valid signal from MoNA or LISA. Because the Sweeper provides the trigger, MoNA-LISA will never be read out unless there is a coincidence with Sweeper. So if MoNA-LISA receives a signal without Sweeper (for example due to a cosmic muon), it will cause Level 3 to go busy, preventing a system trigger from the Sweeper, and leading to a fast clear of MoNA-LISA.

Each PMT in the MoNA-LISA array outputs two signals for a valid event: an anode signal and a dynode signal. The anode is used for timing, while the dynode is used to measure the amount of light deposited on the photocathode. The anode signals are processed through constant fraction discriminators (CFDs) before being sent to time-to-digital converter (TDC) circuits, as well as the XLMs for trigger logic. The dynode signals are sent directly into charge-to-digital converter (QDC) circuits.

The suite of Sweeper detectors includes three plastic timing scintillators (the thin scintillator, the target scintillator, and the A1900 XFP scintillator), two CRDCs, and the ionization chamber. All of the timing signals from the plastic scintillators are processed through CFDs and sent to TDCs. In addition, the timing signal from the Left Up PMT of the thin scintillator is sent to Level 3 to serve as the system trigger. The charge signals from each pad of the ionization chamber are sent through shaping amplifiers and then to an analog-to-digital converter (ADC). The charge signals from each CRDC pad are processed by frontend electronics (FEE) housed on each CRDC detector, before being sent to XLMs.

A diagram of the DAQ hardware in its entirety is shown in Figure 3.9.

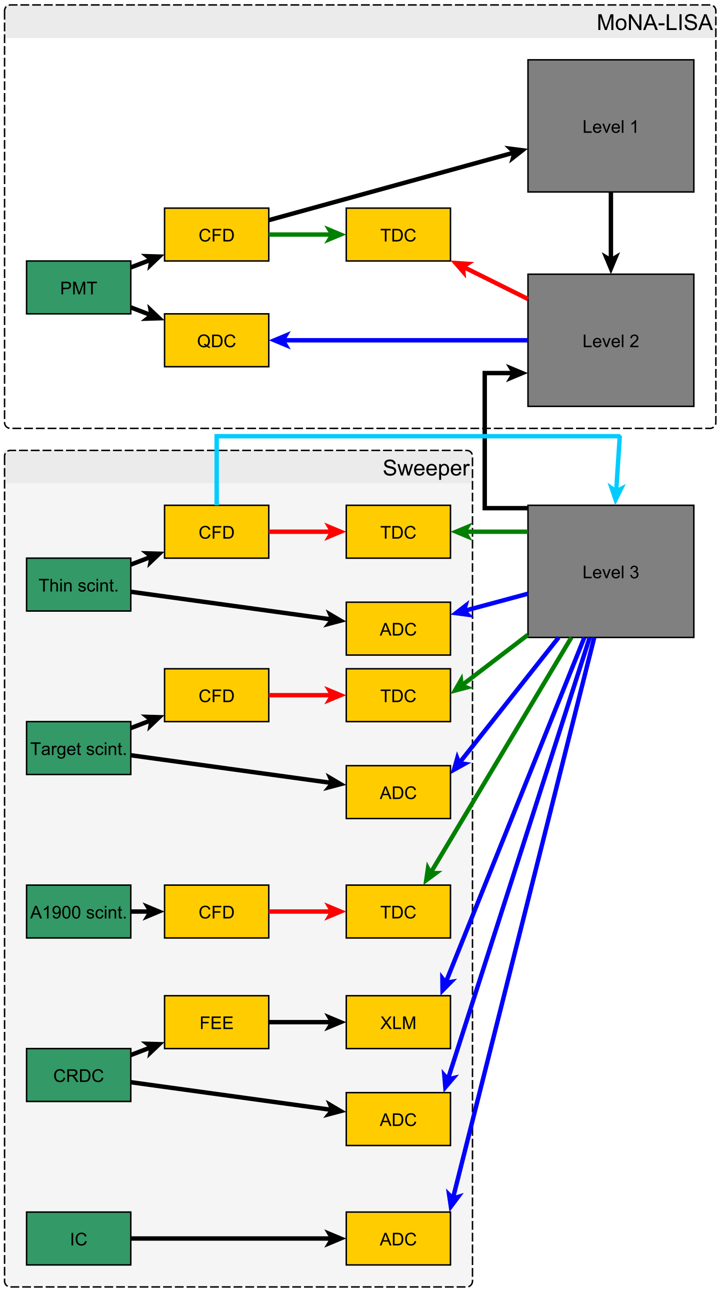

Figure 3.9: A diagram of the DAQ hardware. Data sources are shown in green, signal processing modules in yellow, Level 1, 2, and 3 logic in grey. Green arrows represent START signals, red arrows represent STOP signals, and blue arrows represent GATE signals. The cyan arrow is the system trigger from the Thin Left Up.

3.3.4.2 Software

Each of the three subsystems have their own readout programs using NSCLDAQ 11.2 [82]. Each readout program runs on the DAQ computer dedicated to each device (spdaq40, spdaq42, and spdaq34, for MoNA, LISA, and Sweeper, respectively), and each has its own corresponding single-producer, multi-consumer ring buffer (named “mona”, “lisa”, and “sweeper”). (The “sweeper” ring consists of event-built data from both the VME and CAMAC portions of the Sweeper hardware, as shown in Figure 3.11.) A ring buffer is a data structure with a fixed size and modulo addressing, and two pointers called *put* and *get*. The ring buffer is defined to be empty if ($put == get$) is true, and full if ($++put == get$) is true. When a data producer wishes to store data in the ring buffer, it puts that data at the location of the *put* pointer, and the pointer is incremented. When a consumer wishes to take data from the ring buffer, it reads from the location of the *get* pointer, and the pointer is incremented. Thus, the ring buffer operates as a first-in-first-out queue in which data are enqueued by one producer and dequeued by some number of consumers. A more detailed discussion can be found in the NSCLDAQ documentation [82].

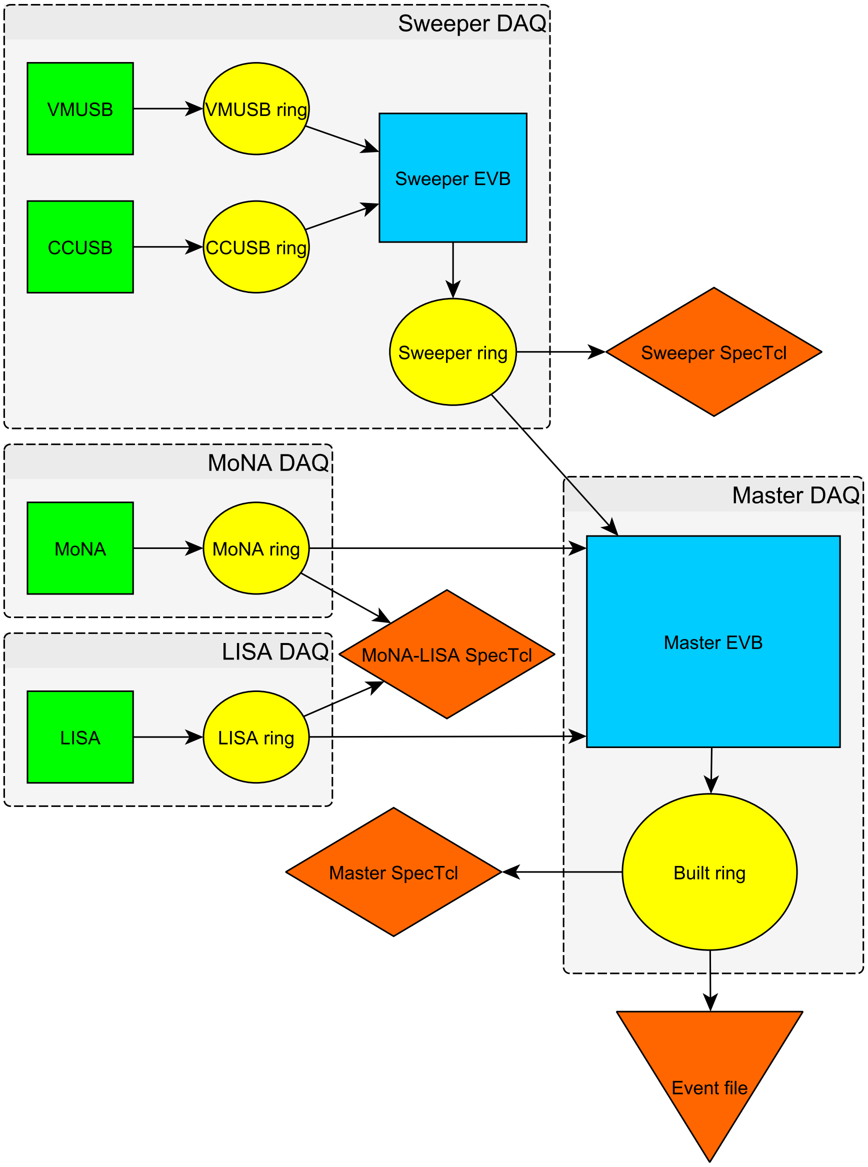

Figure 3.10: A diagram of the DAQ software. Data sources are shown in green, data sinks in red, ring buffers in yellow, and event builders in blue. The arrows indicate the direction of the data flow.

When all of the subsytems are being operated in tandem, as is the case during an experiment, there is a “master” readout program which enslaves the readouts of each of the subsystems, and a master ring buffer (named “built”). The master readout program handles event building, where the ring items of corresponding physics events from each subsystem are combined using the unique 64-bit timestamp carried with each ring item. Finally, a consumer can grab the event-built ring items from the "built" ring and write them to a data file. The binary data file then just needs to be unpacked offline and saved into raw ROOT files, which can then be calibrated and analyzed.

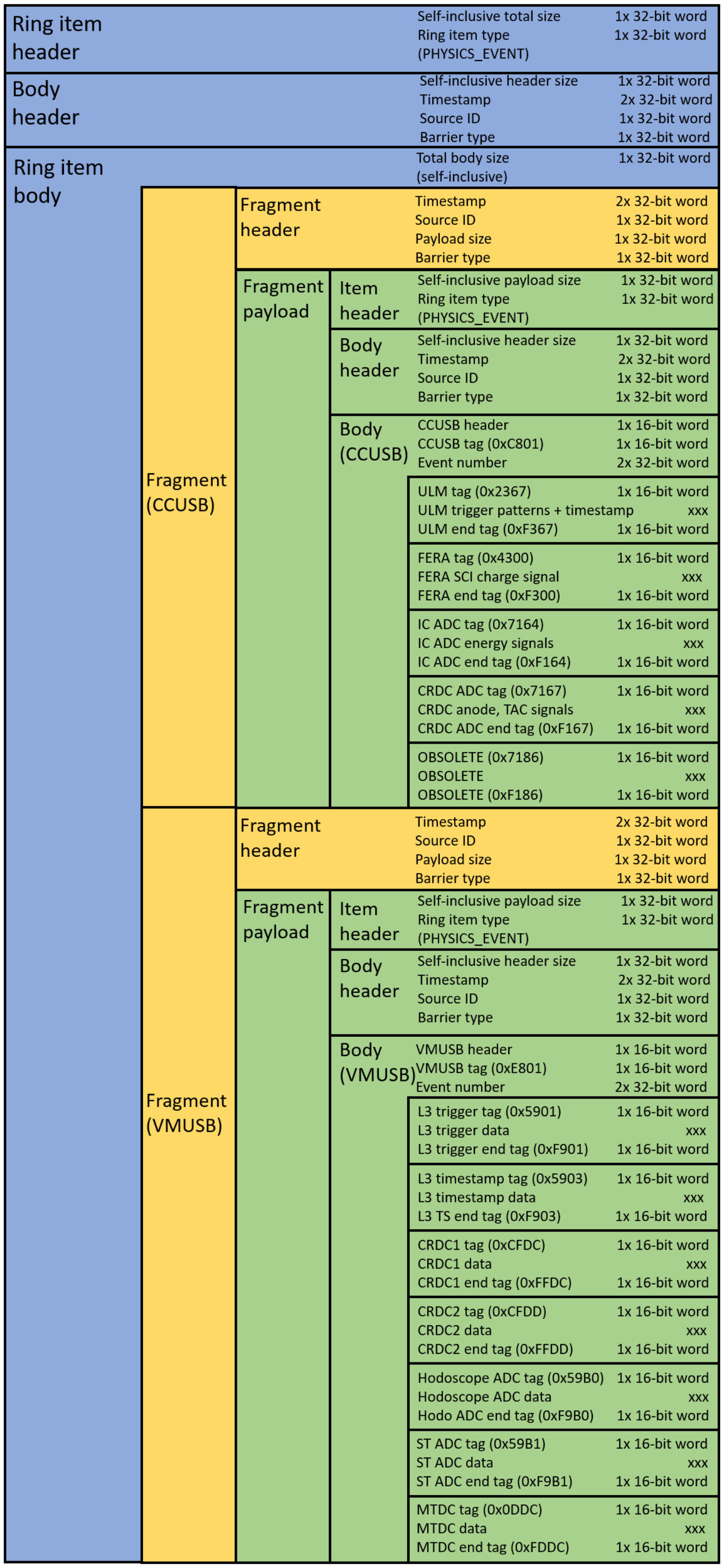

Ring item header				Self-inclusive total size	1x 32-bit word
				Ring item type (PHYSICS_EVENT)	1x 32-bit word
Body header				Self-inclusive header size	1x 32-bit word
				Timestamp	2x 32-bit word
				Source ID	1x 32-bit word
				Barrier type	1x 32-bit word
Ring item body				Total body size (self-inclusive)	1x 32-bit word
	Fragment (CCUSB)	Fragment header		Timestamp	2x 32-bit word
				Source ID	1x 32-bit word
				Payload size	1x 32-bit word
				Barrier type	1x 32-bit word
		Fragment payload	Item header	Self-inclusive payload size	1x 32-bit word
				Ring item type (PHYSICS_EVENT)	1x 32-bit word
			Body header	Self-inclusive header size	1x 32-bit word
				Timestamp	2x 32-bit word
				Source ID	1x 32-bit word
				Barrier type	1x 32-bit word
			Body (CCUSB)	CCUSB header	1x 16-bit word
				CCUSB tag (0xC801)	1x 16-bit word
				Event number	2x 32-bit word
				ULM tag (0x2367)	1x 16-bit word
				ULM trigger patterns + timestamp	xxx
				ULM end tag (0xF367)	1x 16-bit word
				FERA tag (0x4300)	1x 16-bit word
				FERA SCI charge signal	xxx
				FERA end tag (0xF300)	1x 16-bit word
				IC ADC tag (0x7164)	1x 16-bit word
				IC ADC energy signals	xxx
				IC ADC end tag (0xF164)	1x 16-bit word
				CRDC ADC tag (0x7167)	1x 16-bit word
				CRDC anode, TAC signals	xxx
				CRDC ADC end tag (0xF167)	1x 16-bit word
				OBSOLETE (0x7186)	1x 16-bit word
				OBSOLETE	xxx
				OBSOLETE (0xF186)	1x 16-bit word
	Fragment (VMUSB)	Fragment header		Timestamp	2x 32-bit word
				Source ID	1x 32-bit word
				Payload size	1x 32-bit word
				Barrier type	1x 32-bit word
		Fragment payload	Item header	Self-inclusive payload size	1x 32-bit word
				Ring item type (PHYSICS_EVENT)	1x 32-bit word
			Body header	Self-inclusive header size	1x 32-bit word
				Timestamp	2x 32-bit word
				Source ID	1x 32-bit word
				Barrier type	1x 32-bit word
			Body (VMUSB)	VMUSB header	1x 16-bit word
				VMUSB tag (0xE801)	1x 16-bit word
				Event number	2x 32-bit word
				L3 trigger tag (0x5901)	1x 16-bit word
				L3 trigger data	xxx
				L3 trigger end tag (0xF901)	1x 16-bit word
				L3 timestamp tag (0x5903)	1x 16-bit word
				L3 timestamp data	xxx
				L3 TS end tag (0xF903)	1x 16-bit word
				CRDC1 tag (0xCFDC)	1x 16-bit word
				CRDC1 data	xxx
				CRDC1 end tag (0xFFDC)	1x 16-bit word
				CRDC2 tag (0xCFDD)	1x 16-bit word
				CRDC2 data	xxx
				CRDC2 end tag (0xFFDD)	1x 16-bit word
				Hodoscope ADC tag (0x59B0)	1x 16-bit word
				Hodoscope ADC data	xxx
				Hodo ADC end tag (0xF9B0)	1x 16-bit word
				ST ADC tag (0x59B1)	1x 16-bit word
				ST ADC data	xxx
				ST ADC end tag (0xF9B1)	1x 16-bit word
				MTDC tag (0x0DDC)	1x 16-bit word
				MTDC data	xxx
				MTDC end tag (0xFDDC)	1x 16-bit word

Figure 3.11: The contents of a PHYSICS_EVENT ring item in the Sweeper ring buffer, adapted from the Sweeper DAQ Wiki [7]. Ring items like this are consumed both by a Sweeper-only SpecTcl program, and the master event builder, which will combine this item with the corresponding ring items from MoNA and LISA.

The data producers in this system are the detectors: MoNA, LISA, and Sweeper. The Sweeper system is further subdivded into VMUSB and CCUSB controlers for the VME and CAMAC portions, respectively. The data consumers are various SpecTcl programs, and eventually the event files which are written to disk. (SpecTcl is a tool for online viewing and analysis of the incoming data [83].) A diagram of the DAQ software is shown in Figure 3.10.

3.4 Invariant mass spectroscopy

In this section, the relativistic kinematics of a 2-body decay of the form $A \to B + C$ will be considered, and an expression for the decay energy will be derived from conservation of four-momentum. An example of this kind of decay relevant to this work is shown in Figure 3.12. The decay energy is simply the amount of energy released by the decay in the center-of-mass frame. Units with $c = 1$ will be used.

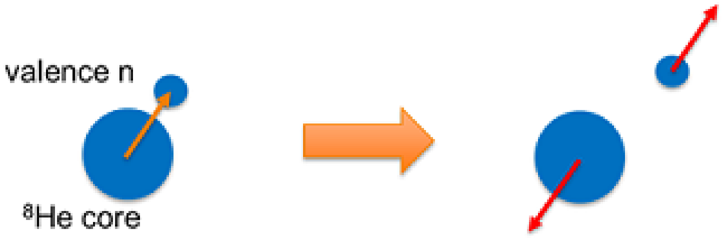

Figure 3.12: A schematic representation of the 2-body decay ^{9}He $\to$ ^{8}He + n.

Conservation of energy and momentum requires that the total four-momentum of the initial state be equal to the sum of the four-momenta of all particles in the final state. Therefore,

$$p_A^\mu = p_B^\mu + p_C^\mu \tag{3.1}$$

$$(p_A^\mu)^2 = (p_B^\mu + p_C^\mu)^2 \tag{3.2}$$

Squares of four-momenta are Lorentz-invariant, so they can be evaluated in any frame of reference. Defining the decay energy to be the rest energy of the initial particle, minus the sum of the rest energies of the final particles, the quantity on the left side will be evaluated in the center-of-mass frame:

$$(p_A^\mu)^2 = (E_d + m_B + m_C)^2 \tag{3.3}$$

The quantity on the right side of the previous equation factors into three terms:

$$(p_B^\mu + p_C^\mu)^2 = (p_B^\mu)^2 + (p_C^\mu)^2 + 2(p_B)^\mu (p_C)_\mu \tag{3.4}$$

The squared terms are trivial to evaluate in the rest frame of each particle, and the cross term is evaluated in the laboratory frame.

$$(p_B^\mu + p_C^\mu)^2 = m_B^2 + m_C^2 + 2(E_B E_C - \vec{p}_B \cdot \vec{p}_C) \tag{3.5}$$

Combining these results, and solving for the decay energy, the result is:

$$E_d = \sqrt{m_B^2 + m_C^2 + 2(E_B E_C - \vec{p}_B \cdot \vec{p}_C)} - m_B - m_C \tag{3.6}$$

Now the decay energy is specified for an arbitrary 2-body decay, in terms of the masses, total energies, and three-momenta of the two particles in the final state. This equation is symmetric between particles B and C. For the purposes of this dissertation, “B” will represent a neutron, and “C” will represent the daughter of the decay, referred to as the “fragment”.

3.5 Time-of-Flight method

Invariant mass spectroscopy works very well for cases where the fragment of interest moves approximately along the design trajectory through the Sweeper magnet. However, if one wishes to analyze fragments with a magnetic rigidity significantly different than what the Sweeper magnet is set to, the small-angle approximation may be violated, and the application of a COSY optics matrix can give unreliable results. Instead of analyzing a decay energy, which relies on knowledge of the fragment angles at the target position, one can analyze a somewhat less robust observable, the “relative velocity”:

$$v_{rel} \equiv |\vec{v}_n| - |\vec{v}_f| \tag{3.7}$$

To calculate this quantity, the neutrons are treated in the exact same way that they are in the invariant mass method. However the fragment angles are no longer necessary, and the fragment kinetic energy is simply calculated from the time-of-flight between the target and the thin scintillators, without involving the COSY optics matrix. The flight path length of the fragment is not known on an event-by-event basis, so a single value is used, representing the arc length of the path of the centroid of the magnetic rigidity distribution for the desired fragment. In order to ensure that this approximation is valid, a tight gate is made around the center of the neutron x versus y distribution in order to restrict the analysis to cases where the fragment and neutron are emitted in the forward/backward direction in the center-of-mass frame. The path length can be used as a tunable parameter (within uncertainties) to align the centroid of the relative velocity distribution with zero. The important information in the relative velocity distribution is carried in the shape and the width rather than the location of the centroid, which should be close to zero.

Because the relative velocity requires less information than the decay energy, it can be calculated even in cases where the fragment is not centered in the Sweeper magnet. But the fact that it contains less information also means that it is a less sensitive observable for fitting. To summarize: a decay energy should be used when possible, but when a decay energy is not accessible, a relative velocity can be used instead.

Chapter 4

Data Analysis

4.1 Detector calibrations and corrections

This section details the calibrations and corrections performed on all of the various detectors used in this analysis.

4.1.1 Charged particle timing scintillators

Signals from the various charged particle timing detectors are used (after constant-fraction discrimination) to START and STOP time-to-digital converter (TDC) circuits. In this experimental setup, the TDCs are operated in common start mode, meaning that all TDC channels are started based on a common signal from Level 3, and the TDC STOP is provided by each individual detector. So the timing signal for each detector is measured relative to the common start. However, only time differences are physically relevant for this analysis, so the overall timing offset for each detector is arbitrary. In this analysis, the convention will be that $t = 0$ should represent the passage of the secondary beam through the target position. Offsets for each timing detector will be set to enforce this condition.

The TDC slopes, on the other hand, are not arbitrary. They represent a conversion factor between TDC channels and physical times, measured in nanoseconds. All of the charged particle timing signals are processed through different channels in the same Mesytec

Table 4.1: Unreacted secondary beam velocities.

Beam:	Speed after A1900 XFP [cm/ns]:	Speed after target scintillator [cm/ns]:
^{11}Be	8.92	8.83
^{12}B	9.01	8.90

TDC module, and the slopes are fixed by the hardware to be 0.0625 ns/channel.

The constant-fraction discrimination helps to mitigate timing walk, however the raw TDC spectra are still distorted by jitter, introduced by the Field Programmable Gate Arrays (FPGAs) controling the Sweeper logic. The FPGA jitter varies on an event-by-event basis, but it is common to all of the charged particle timing detectors. In order to correct for this effect, a jitter subtraction is done using the Thin Left Up time signal. Subtracting the Thin Left Up signal from all of the others before applying the individual offsets helps to cancel the common FPGA jitter.

Taking the above value of the slope, the raw time spectrum from each detector in a target-out run can be converted into partially calibrated, jitter-subtracted time spectra in nanoseconds, but without any offset. Then, using the known distances between each detector and the target position, and the known speed of the secondary beam based on the A1900 rigidity acceptance, an offset can be applied such that the peak in each time spectrum can be placed at the appropriate physical time. Even though there is no reaction target present during these runs, the beam will still lose a small amount of energy as it passes through the scintillator detectors. However it is straightforward to calculate these energy losses in LISE++, and use the appropriate beam velocity when calibrating each detector. The relevant velocities are shown in Table 4.1. Because there are two different secondary beams used in this analysis, with different velocities, the timing detector offsets are determined independently for each secondary beam. The results are shown in Table 4.2.

Table 4.2: Charged particle timing detector offsets.

Detector:	z position [cm]:	^{11}Be TDC offset [ns]:	^{12}B TDC offset [ns]:
Thin Left Up	405	45.9	45.6
Thin Left Down	405	47.2	46.9
Thin Right Up	405	48.4	48.0
Thin Right Down	405	50.1	49.7
Target scintillator	-107	14.6	12.3
A1900 scintillator	-1088	-571.2	-571.5

The offsets are all very similar between the two different calibrations, except for the target scintillator, where the difference in offsets is about 2 ns. This difference is due to the fact that the bias voltage applied to the PMT on this detector was changed between the calibration runs. This difference does not affect any other quantities in the analysis, as the time-of-flight is only used for particle identification (PID). As long as PID can still be achieved, even the absolute value of the time-of-flight can be treated as arbitrary.

The target and A1900 scintillators are standalone detectors, but the “thin scintillator” represents the combination of the four quadrants of the detector (Left Up, Left Down, Right Up, and Right Down), each of which has its own PMT and signal processing circuits. After each of the quadrants is calibrated in the way described above, they are combined in software into a single quantity by taking the arithmetic mean of their calibrated times for each event.

An example of the charged particle timing scintillator calibration is shown in Figures 4.1 and 4.2.

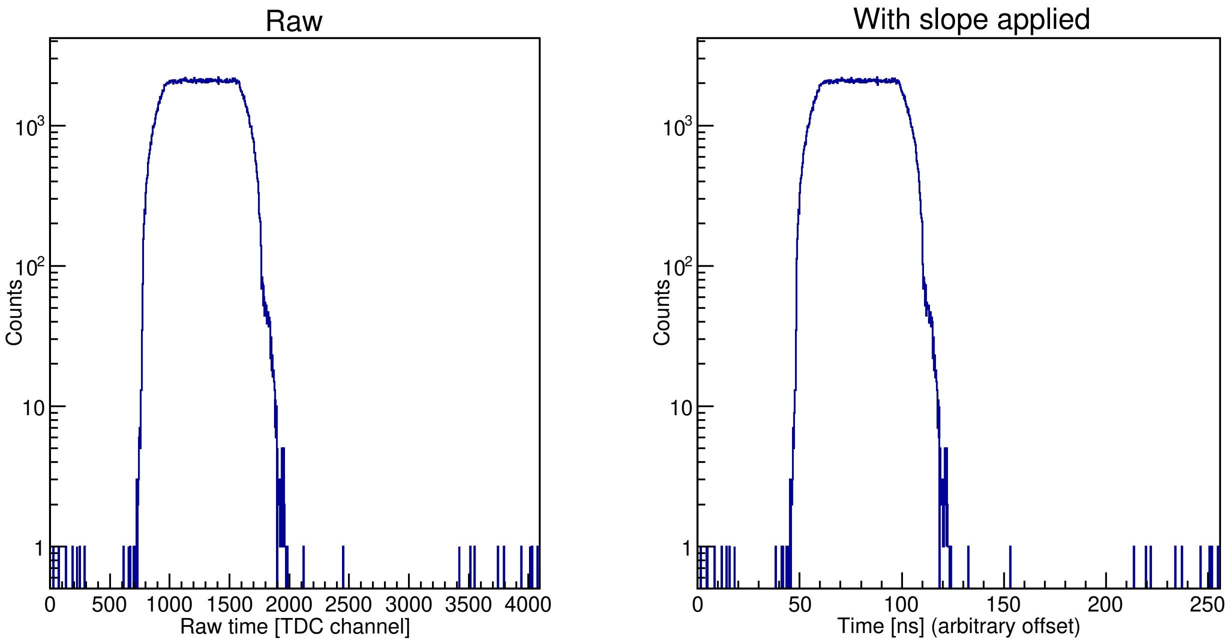

Figure 4.1: The first stage of time calibration of the target scintillator. The left panel shows the raw TDC spectrum. The right panel shows the spectrum after applying the slope, but before subtracting the jitter, and applying the offset. These data were taken from a target-out run where the Sweeper magnet was set to center the ^{11}Be beam (Run 2005).

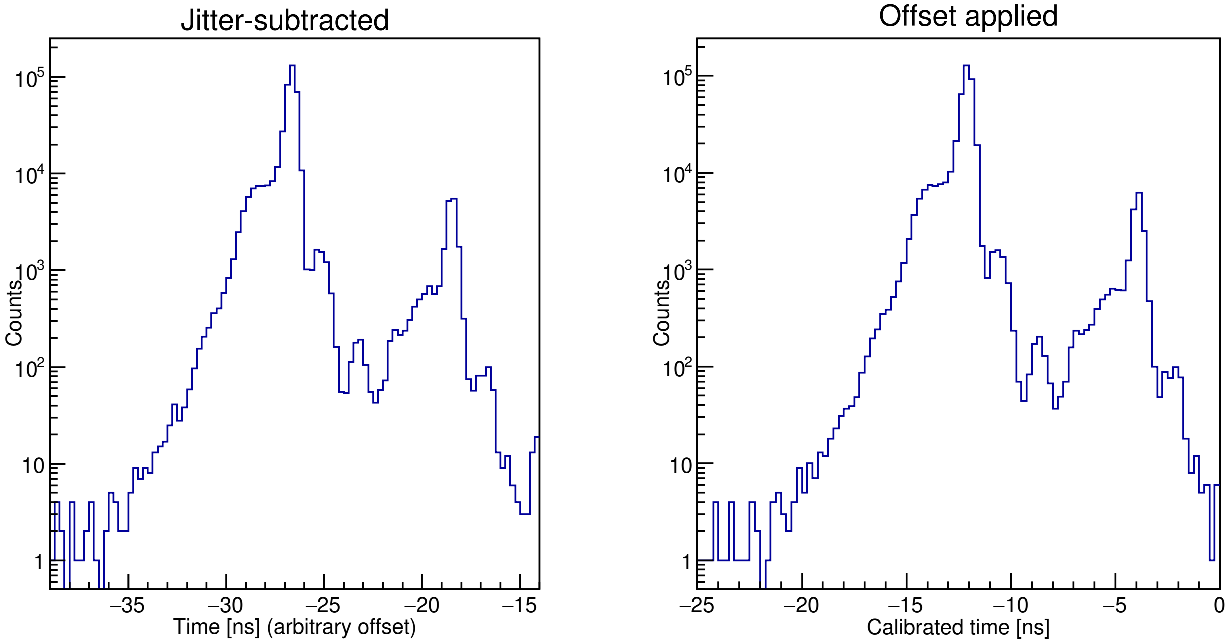

Figure 4.2: The second stage of time calibration of the target scintillator. The left panel shows the TDC spectrum after applying the slope and jitter subtraction, but before applying the offset. The right panel shows the spectrum after applying the offset. These data were taken from a target-out run where the Sweeper magnet was set to center the ^{11}Be beam (Run 2005).

4.1.2 CRDCs

The CRDCs are two gas-filled detectors used to measure the positions and angles of the fragments after they travel through the Sweeper magnet. Each one is segmented horizontally into 128 pads (the first 12 are not present in the physical detectors, so there are really only 116 active pads). The charge induced on each pad is read out for each event and processed through an analog-to-digital converter (ADC) circuit. By fitting the charge distribution as a function of pad number, the physical position of each event in the horizontal (x) direction can be inferred. And by measuring the time for the the freed electrons to drift vertically through the detector, a vertical (y) position is measured as well. The drift time for each event is recorded using a time-to-amplitude converter (TAC) circuit. Therefore each CRDC provides an (x,y) coordinate pair for each event, and the combination of the two CRDC (x,y) positions determines the angles of each fragment relative to the beam axis in the horizontal and vertical directions. This section discusses the calibrations performed on the CRDC detectors in this work.

Noise in the signal processing electronics creates a “pedestal” signal which shows up in the energy loss spectrum of each CRDC pad. Before any further calibrations are done, an offset is applied to subtract this pedestal from the spectrum of each pad. These offsets are determined by running the acquisition code offline while the CRDCs are turned on. Only the pedestal signal will show up in the pad charge spectra. Then each pad spectrum can be fit to a Gaussian function, and the centroid of that Gaussian fit is the pedestal value for that pad. In all subsequent uses of the CRDCs, those pedestal values will be subtracted from the raw data in each pad, in each CRDC.

The CRDC pedestal distributions can be seen in Figure 4.3.

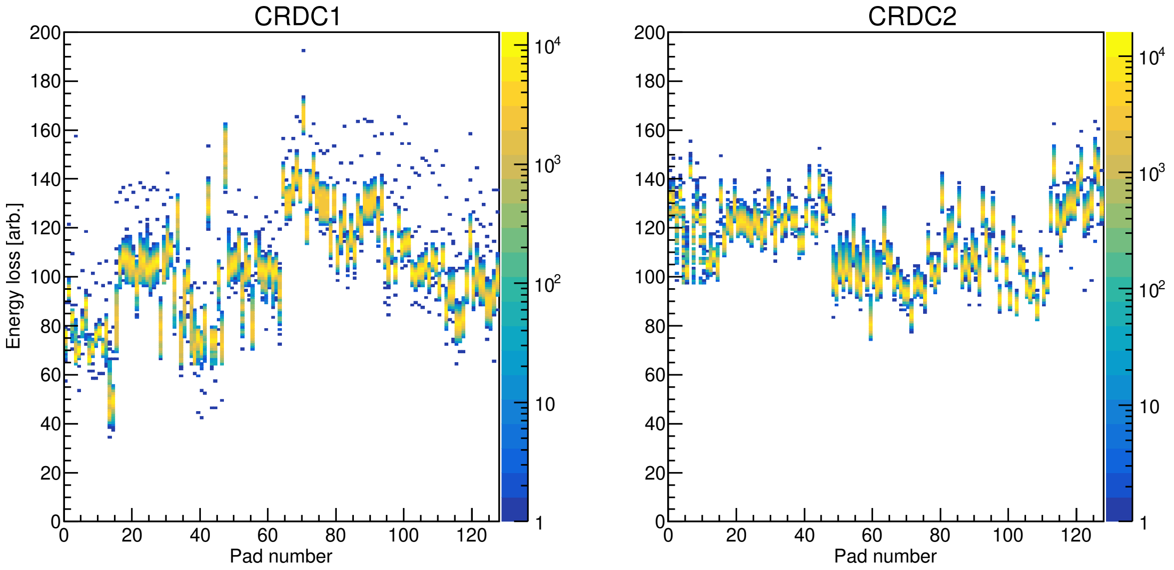

Figure 4.3: The pedestal distributions for the CRDCs, taken offline at the beginning of the experiment (Run 2001). The left panel shows CRDC1 and the right panel shows CRDC2.

Once the pedestals are removed from each CRDC pad, the pads must be gain-matched to each other in order to reconstruct the x-position correctly. The CRDC pad gain matching is very similar to the ion chamber pad gain matching, described in detail in the next section. Any pads that are not functioning properly are declared "bad pads", and removed from the analysis. In theory the removal of a few isolated pads does not hinder the determination of the x-position, as long as a Gaussian fit to the charge distribution as a function of pad number can still be performed. The gain-matching is performed with a chain of data runs in which the unreacted ^{12}B beam is swept across the vacuum chamber by varying the Sweeper current. It can be helpful to apply an energy loss gate on the ion chamber in order to isolate a single element and get the cleanest possible pad summary spectra. The results of gain-matching CRDC2 are shown in Figure 4.4. In the raw spectrum, four distinct bands are visible. This is because the pad charge distribution is time-sampled four times, and the results are averaged in order to obtain the raw charge induced on each pad. The three "shadow" bands below the main peak correspond to cases where one, two, or three samples for that pad are missing.

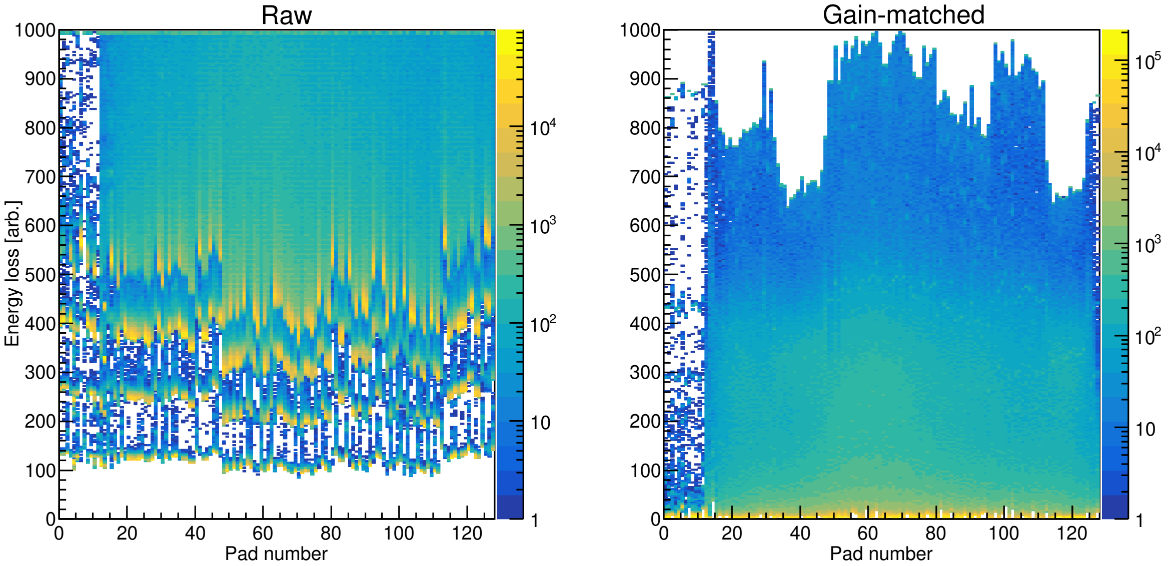

Figure 4.4: The gain-matching of the CRDC2 pads. The left panel shows the pad summary before pedestal subtraction and gain-matching, and the right panel shows the pad summary after. The same procedure was applied to both CRDCs, and the reference pad for both was chosen to be Pad 75. The data come from a chain of Run 2026 (centered ^{12}B), and Runs 2032 - 2039 (sweeping ^{12}B).

After the gain matching is done, the position calibrations can be performed. The position calibrations are done using "mask runs", where a tungsten mask (0.25 inch thick) with holes drilled at specific, known locations is placed in front of each CRDC. Highly-charged heavy ions will be stopped within the thickness of the tungsten, but pass freely through the holes. This leads to an image of the mask holes being projected onto each CRDC, and then the coordinates of each hole can be mapped via a linear function to the physical values. Some low-Z ions may be able to penetrate through the entire thickness of the tungsten and degrade the quality of the mask calibration data, but these events can be removed in software by placing a gate on something with high energy loss in the ion chamber, isolating particles

Table 4.3: CRDC mask calibration parameters.

Detector:	x slope [mm/pad]:	x offset [mm]:	y slope [mm/channel]:	y offset [mm]:
CRDC1	2.54	-186.103	-0.0761	106.040
CRDC2	-2.54	186.055	-0.0767	98.610

of high Z. Even though the physical origins of the horizontal and vertical positions signals (fitting of pad charge distributions, and a TAC time spectrum, respectively) are different, the mask calibration works in the exact same way for both: a linear calibration function is used to map the raw signal onto physical positions in millimeters. The slope of the x-position is fixed by the geometry of the pads, but the x-offset, y-slope, and y-offset are determined by linear fits to the locations of the holes. For this experiment, the CRDC1 mask run was Run 2028 and the CRDC2 mask run was Run 2083. Both runs were taken with the target out and the ^{12}B beam centered in the Sweeper magnet. The results of the CRDC2 mask run are shown in Figure 4.5, and the calibration parameters used in this analysis are shown in Table 4.3.

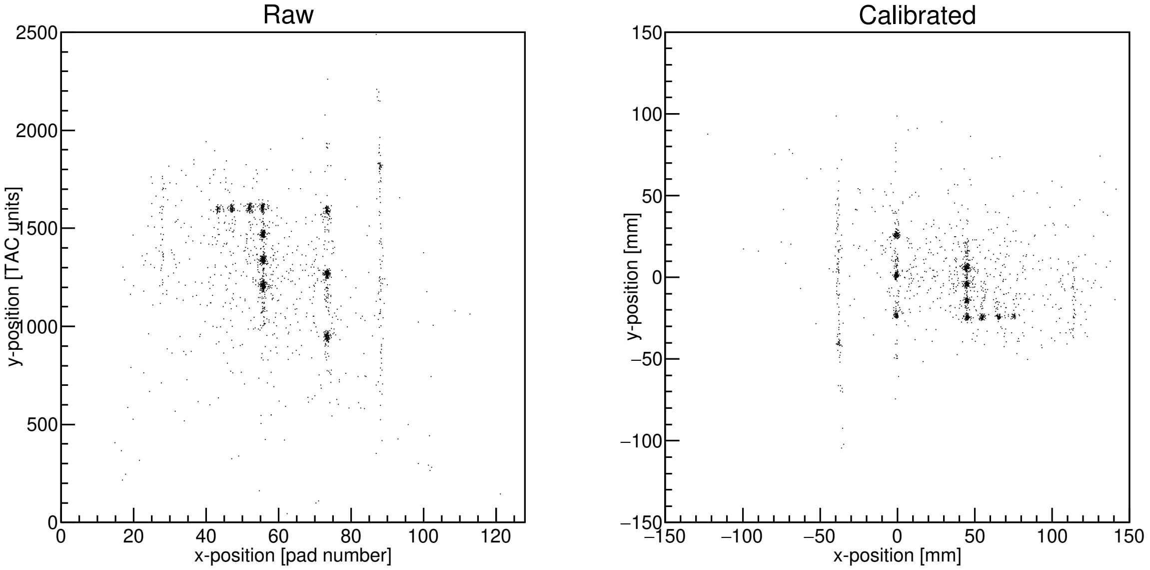

Figure 4.5: The mask calibration of CRDC2. The left panel shows the uncalibrated spectrum, and the right panel shows the calibrated spectrum. Due to the physical orientation of the detector, the calibration involves a horizontal and vertical reflection. The data are taken from Run 2083, where the target was removed, the ^{12}B beam was centered, and the CRDC2 mask was inserted.

4.1.3 Ionization chamber

The ion chamber is a gas-filled detector which is used to measure the energy loss of charged ions which pass through its active volume. The detector is segmented into 16 pads along the beam axis, and the charge induced on each pad is read out for each event. Each of the signals is processed through an ADC circuit. For this analysis, four of the ion chamber pads (Pads 0, 4, 7, and 15) were dysfunctional, and were removed from the analysis. The energy loss value used in the analysis comes from the summed signals on each of the good pads, and in order to improve the energy resolution of the detector, the pads must be gain-matched to each other. This is done in software by applying a slope and offset to each good pad in order to align peaks in a calibration spectrum to those of an arbitrary reference pad.

The calibration data were taken with the target out and the secondary beam centered in the Sweeper magnet. Because the beam is not pure, and particles of different Z will lose different amounts of energy in the active gas, there will be multiple peaks in the energy loss spectrum of any given pad. These peaks can be fit to Gaussian functions, and their centroids can be used to determine the coefficients of the linear function necessary to align each pad with the reference pad. The result of the ion chamber gain-matching is a linear function which maps the energy loss in raw ADC channels to an energy loss in arbitrary, physical units. Because the ion chamber energy loss is only used for particle identification, the numerical value in absolute units is not relevant. The pad spectra before and after gain-matching are shown in Figure 4.6.

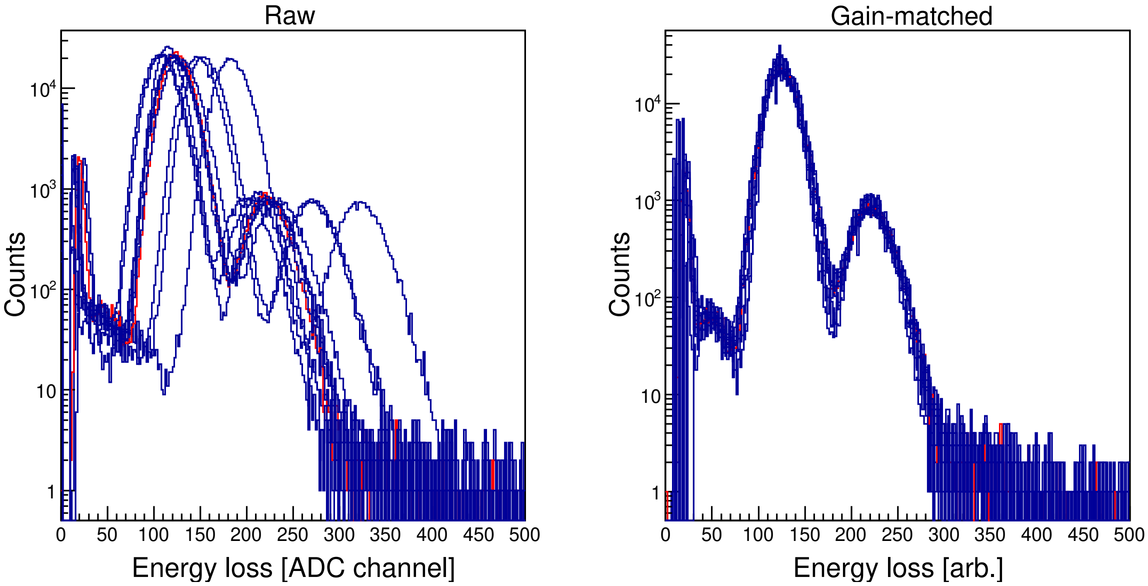

Figure 4.6: The energy loss spectra of each good pad overlaid. The left plot shows all of the raw energy loss spectra, and the right panel shows all of the gain-matched energy loss spectra. The largest two peaks in the spectra were fit to Gaussian functions, and their centroids were linearly transformed to align with the reference pad (marked in red). These data were taken from a target-out run where the Sweeper magnet was set to center the ^{11}Be beam (Run 2005).

After the ion chamber is gain-matched, no further calibration is necessary, and the energy loss is simply proportional to the sum of the signals in each of the gain-matched pads. However there are some unwanted dependencies that can be corrected in order to achieve better energy resolution, and therefore cleaner particle identification. The ionization and charge collection inside the ion chamber are correlated with both the horizontal (x) and vertical (y) positions of the incident particle (horizontal moreso than vertical). These dependencies can be corrected one-by-one by fitting the correlation to some polynomial function, and dividing the summed energy loss parameter by that polynomial. Formulaically:

$$\Delta E_x = \frac{\Delta E}{\sum_{i=1}^{N_x} \alpha_i x^i} \tag{4.1}$$

where ΔE is the uncorrected (gain-matched) energy loss signal, and ΔE_x is the energy loss after correction for x-dependence. Then to correct the y-dependence, simply repeat the procedure using the x-corrected energy loss:

$$\Delta E_{xy} = \frac{\Delta E_x}{\sum_{i=1}^{N_y} \beta_i y^i} \tag{4.2}$$

N_x and N_y are the chosen orders of the polynomial fit functions (both were set to 3 for this analysis), and α_i and β_i are the fit parameters. The x and y values used for the position corrections are the x and y positions of the particle measured by CRDC2. Now the energy loss signal for the ion chamber, still in arbitrary units, can be taken to be ΔE_{xy}, which has reduced dependencies on the horizonal and vertical positions. This makes for a cleaner particle identification plot, which makes event selection easier.

The position corrections are done using a chain of target-out runs with the ^{12}B secondary beam, where the Sweeper current is varied in order to sweep the unreacted beam horizontally across the CRDC detectors. The sweep runs allow access to regions of large $|x|$, where the position-dependence is strongest. The horizontal position correction is demonstrated in Figure 4.7. The vertical correction is done in the same way, except the dependence is much weaker. The position dependences in this analysis are very weak, so these corrections are not particularly important. This conclude all of the calibrations and corrections needed for the ion chamber.

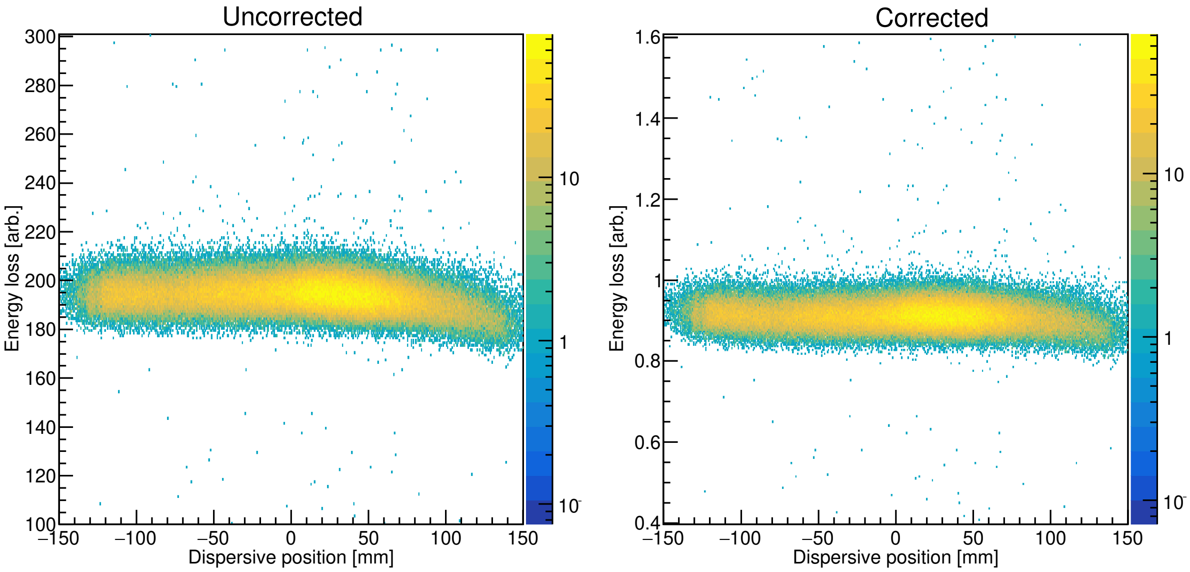

Figure 4.7: The horizontal position correction of the ion chamber energy loss. The left panel shows the uncorrected spectrum, and the right panel shows the corrected spectrum, with reduced position-dependence. The data come from a chain of Run 2026 (centered ^{12}B), and Runs 2032 - 2039 (sweeping ^{12}B).

4.1.4 MoNA-LISA

Each bar of MoNA-LISA has two PMTs, and each PMT provides a time signal and a light output (“charge”) signal. The charge signal is processed through a charge-to-digital converter (QDC), and the time signal is processed through a time-to-digital converter (TDC) (after discrimination). Both the time and the charge spectra are calibrated, and then there are additional calibrations applied for the horizontal (x) position, for tying the timings of each bar to the other bars within the same table, and finally, the overall timing of each table relative to the common stop.

Most of the calibrations are done offline using cosmic muons, but some are done using a time calibrator module, or online using bremsstrahlung photons. The cosmic muons are ultrarelativistic, so their speed can be approximated as c. Before any calibrations are performed, each of the PMTs needs to be gain-matched to the others. This is done offline, before the experiment begins. The procedure is to take cosmic ray data, and iteratively change the bias voltage on each PMT until the cosmic peak in the charge spectrum aligns with a fixed distance from the QDC pedestal. The final voltages for each PMT typically lie within the range of 1300-1950 V. Once the gain-matching is complete, the QDC calibrations are performed. The MoNA-LISA calibrations are performed with the array operating in standalone mode, so no coincidence with Sweeper detectors is required.

4.1.4.1 QDC calibration

The QDC calibration consists of determining a threshold, which is used by the data acquisition system to ignore the QDC pedestal, and a linear calibration to set the cosmic muon peak to about 20 MeVee (MeV electron equivalent, the amount of light produced by an electron with a kinetic energy of 1 MeV). This value comes from the average energy loss of a cosmic muon in the detector bars (from Reference [84]), and the thickness of each bar. If q_p is the location of the pedestal in QDC channels, the QDC threshold is calculated as:

$$Q_0 = \frac{q_p}{16} + 2 \tag{4.3}$$

The factor of 16 is used to convert the channel number from 12 bits to 8 bits, and the

2 is simply to place the threshold slightly above the pedestal value. The linear calibration function which converts the raw charge in QDC channels (q_r) into a calibrated charge in MeVee (q_c) is then:

$$q_c = m(q_r - q_p) \tag{4.4}$$

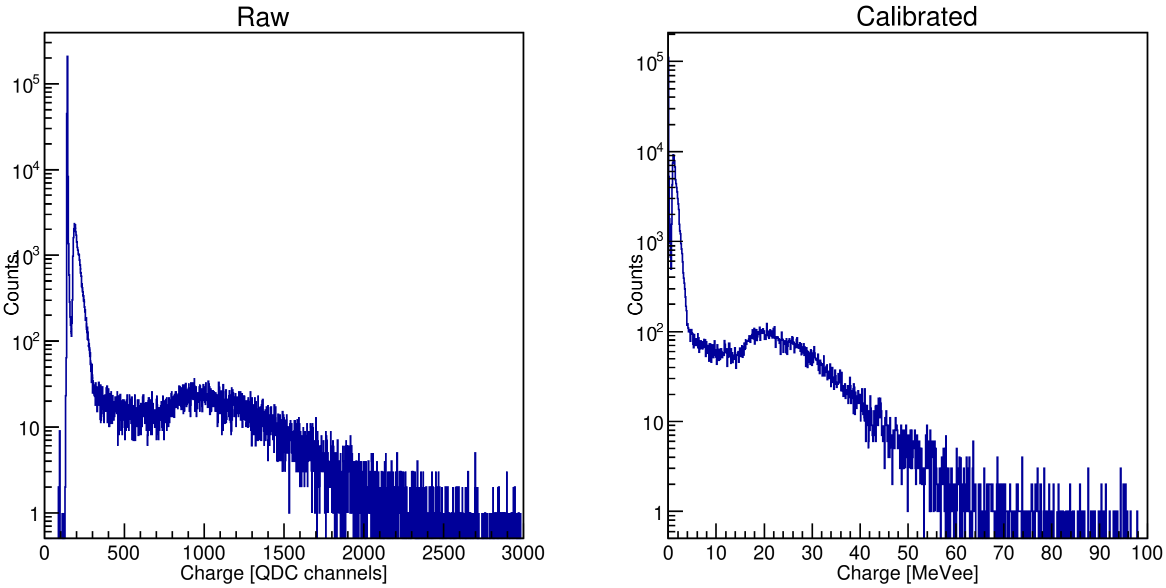

Figure 4.8: The QDC calibration for one PMT in LISA. The left spectrum is uncalibrated, and the right spectrum is calibrated. After calibration, the pedestal is removed, and the features which remain are a sharp peak at low charge due to background γ-rays, and a broad cosmic muon peak.

The determination of the calibration parameters is automated using Gaussian fits to find the locations of the pedestal and the cosmic peak for each PMT. The resulting calibrated spectrum should have the pedestal subtracted, and the cosmic peak aligned with 20 MeVee. And example of the QDC calibration for one PMT is shown in Figure 4.8.

4.1.4.2 TDC calibration

The first step in calibrating the neuton time-of-flight spectra is to determine the TDC slopes for each individual PMT in the array. This is done using a time calibrator module, which produces a START signal, and a STOP signal randomly at discrete intervals after the START. This produces a "picket fence" in the MoNA-LISA time spectra, and the spacing of the picket fence is tunable in the hardware of the time calibrator. For this analysis, the picket fence spacing was chosen to be 40 ns. Using the known spacing, the slope of a linear function can be determined in order to convert the raw peak locations in TDC channels to physical times in nanoseconds. This calibration only determines the slope, so there is still an overall offset which will be determined in subsequent sections. An example of a TDC slope calibration is shown in Figure 4.9.

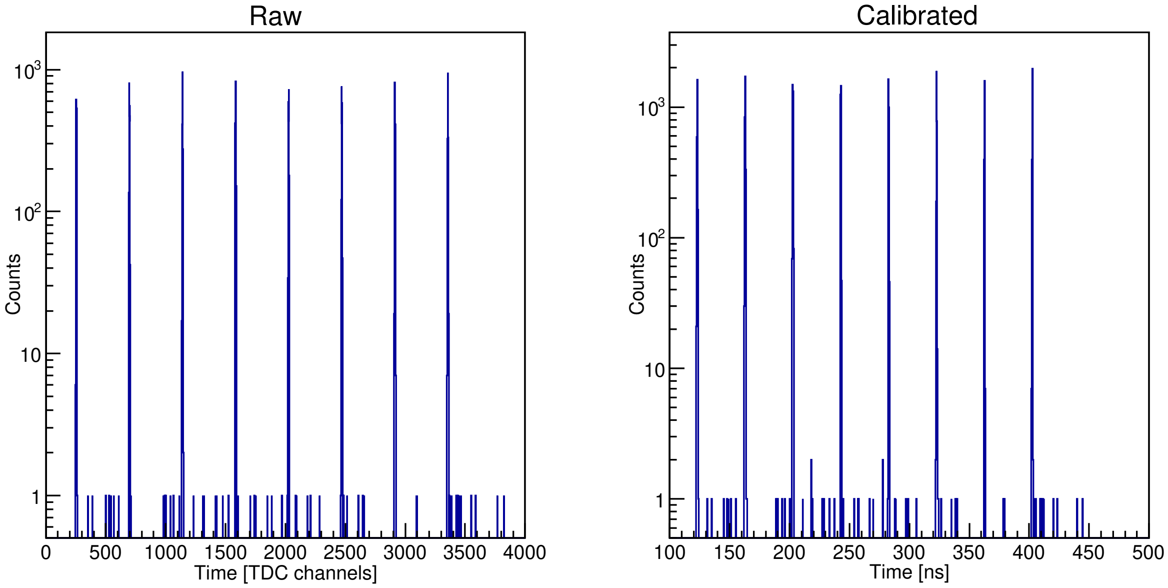

Figure 4.9: The TDC calibration for one PMT in LISA. The left spectrum is uncalibrated, and the right spectrum is calibrated. These data are taken from a time calibrator run, where the "picket fence" spacing is set to 40 ns. This is used to determine the TDC slope for each PMT in the array. The offsets are determined later, using the method described in subsequent sections.

4.1.4.3 x-position calibration

In order to determine the x-position of each hit in the array, the time difference between the signals in the left and right PMTs is used. Because light propagates through the bars at constant speed, this time difference should be proportional to the x-position where the light originated from. In order to determine the slopes and offsets of the linear calibration function for each bar, cosmic muons are used to illuminate the bars uniformly in position. A histogram of the time differences for each bar should then have a rectangular shape. The edges of the rectangle can be fit to sigmoid functions, and a slope and offset can be determined to map the edges of the bars to their physical distances (±100 cm). In terms of the TDC-calibrated left and right PMT times (t_l and t_r, respectively) the calibration function has the form:

$$x = m(t_l - t_r) + b \tag{4.5}$$

This calibration determines the parameters m and b. An example is shown in Figure 4.10.

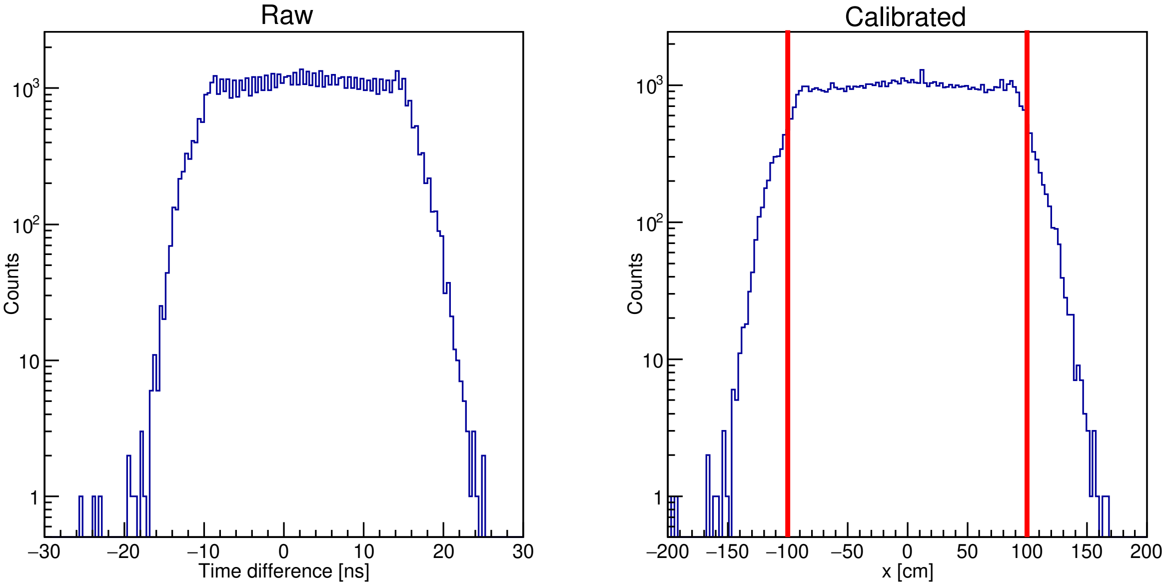

Figure 4.10: The x-position calibration for one bar in LISA. The left spectrum is uncalibrated, and the right spectrum is calibrated. These data are taken from a cosmic muon run. The vertical lines in the calibrated spectrum represent the physical ends of the bars. Some small number of counts fall outside these lines due to the stochastic nature of the detector response.

However, this only determines the position of the hit relative to the center of the bar, it does not contain any information about the absolute locations of the bars in the experimental vault. In order to account for the locations of each bar relative to the beam axis, there is an additional offset for the locations of the bars in beamline coordinates. The bar locations were determined from laser measurements.

4.1.4.4 $\mathbf{T}_{mean}$ calibration

The TDC calibrations discussed above set the slopes for each TDC, but there is still an overall timing offset which must be determined for each bar. The calibrated time-of-flight for a given bar is calculated as the average of the time-of-flights registered by each PMT. The overall timing offset is applied to this averaged time. The timing offset can be split into two parts, where each bar has some offset relative to a reference bar (typically the top bar in the first layer of each table), and then each table has an offset with respect to the target. The first part, the relative offset between bars in a given table, is determined using cosmic muons. The idea behind this calibration is simply to select high-muliplicity events, where a single muon interacts with many bars on the same table. Then, using the differences in the calibrated positions of the hits, and the known speed of the muon (assumed to be c), an absolute timing offset can be applied to each bar relative to the reference bar (shown in Equation 4.6). This is done separately for each of the three tables, and then all that remains is to place each table on an absolute time scale relative to the target scintillator.

$$t_{ij} = \frac{|\vec{r}_j - \vec{r}_i|}{c} \tag{4.6}$$

Finally, the second part of the overall timing offset is determined online using bremsstrahlung gamma rays. When the beam passes through the target, bremsstrahlung x-rays are produced, and some of them will deposit their energy into MoNA-LISA. Using the calibrated position of the x-ray hit in MoNA-LISA, and the known speed of the photons, the mean time-of-flight for each table can be placed into an absolute time scale. This calibration assumes that the photons originate from the target position. One should be aware that there will also be bremsstrahlung from the unreacted beam hitting the walls of the Sweeper vacuum chamber, but these are not usable for the time-of-flight calibration, because they originate from some unknown position, not at the target location. Once each bar and each table has been placed on the same absolute time scale, the MoNA-LISA calibrations are complete.

4.2 Event selection

In order to reconstruct a decay energy spectrum of a given unbound nuclide, we need to isolate the events in which the decay products of that unbound nuclide are detected in coincidence. Since the trigger logic for the entire system is based on the Sweeper detectors, a coincidence with a charged fragment is required for any event in MoNA-LISA. But coincidence alone does not guarantee that the detected event is an event of interest. Impurities in the secondary beam, reactions other than the reaction of interest in the target, and random coincidences between the Sweeper and MoNA-LISA systems will all result in spurious events in the decay energy spectrum, if not properly removed. The following subsections will describe the process of removing these spurious events from the analysis.

4.2.1 Beam gate

Secondary beams coming from the A1900 separator are not pure. The first step in event selection is to isolate events coming from the desired secondary beam, removing events coming from the undesired "contaminant" beams. This is done using a software cut (the "beam gate") based on the time-of-flight between the A1900 XFP scintillator and the target scintillator. For this analysis, making a 1D gate on this spectrum is sufficient to greatly suppress contaminants, as shown in Figure 4.11. For secondary beams with a higher amount of contamination, and/or smaller separation between species, additional requirements may need to be employed.

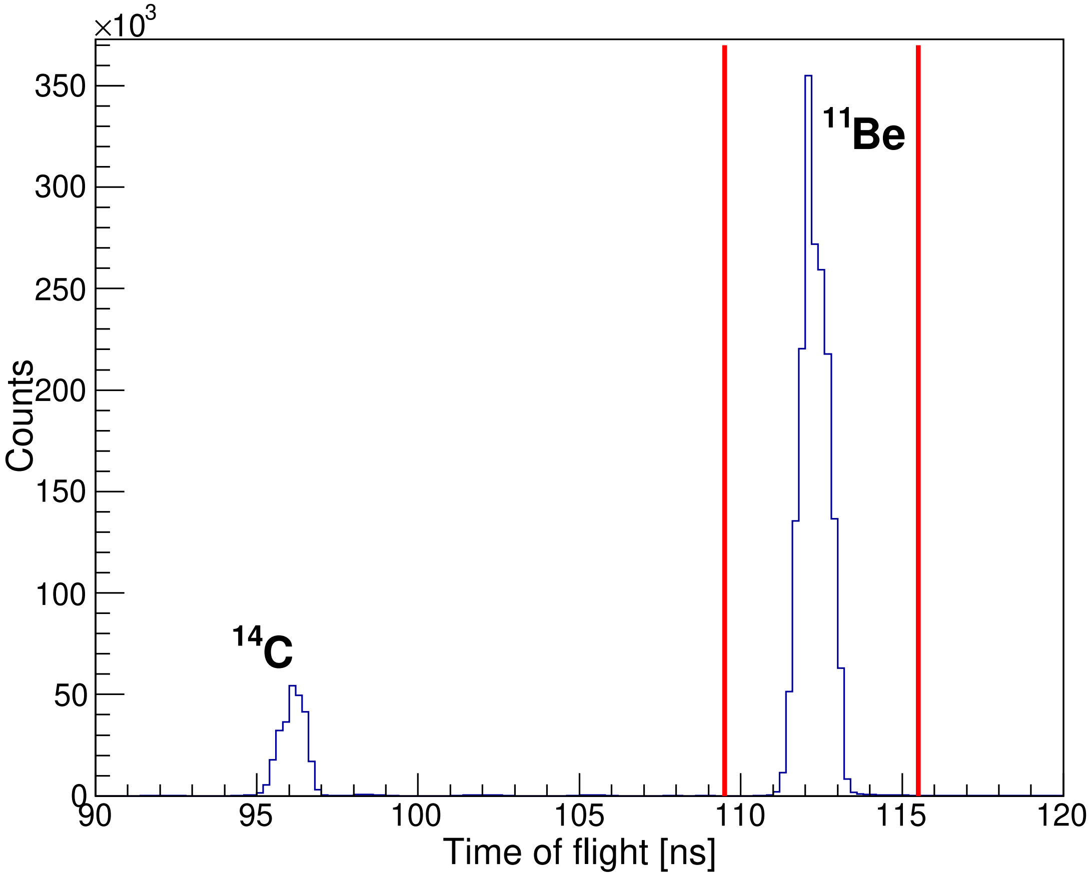

Figure 4.11: ^{11}Be secondary beam identification gate. A 1D cut requiring the ToF to lie between the red vertical lines is used to select events where the incoming particle is ^{11}Be. The main contaminant in this case is ^{14}C, which is easily removed by applying this gate. The same process is applied to the ^{12}B beam, even though it is almost pure.

4.2.2 CRDC quality gates

To make good identification of fragments of interest, and correctly reconstruct their kinetic energies at the target position, good measurements positions and angles at the CRDCs are needed. However the CRDC detectors sometimes give erroneous results due to incomplete charge collection. In order to remove these events from the analysis, "CRDC quality gates" are made to select events in which both CRDCs functioned properly. The CRDC quality gates used in this analysis are shown in Figure 4.12. Events with very low pad sum (the sum of the charge collected on each pad) and/or abnormally small fit σ may give unreliable results for the position, and are removed from the analysis using these gates.

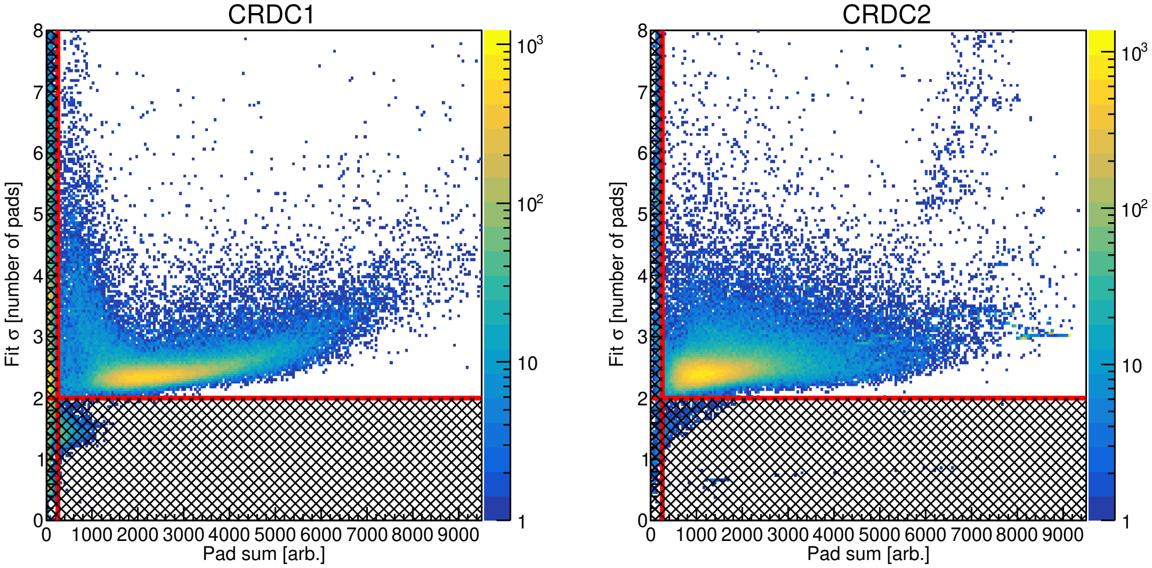

Figure 4.12: The CRDC quality gates used for the ^{11}Be beam. The same gates were used for the ^{12}B beam. The left panel shows CRDC1, and the right panel shows CRDC2. The events above both the horizontal and vertical lines are accepted as good events, and the rest (within the cross-hatched area) are removed from the analysis.

4.2.3 Charged fragments

Once the desired seconday beam has been selected using the beam gate, there are still potentially multiple different reaction channels that the beam particles can undergo when they interact with the target nuclei. One particular reaction channel contains the unbound nuclide of interest, and the rest do not, so they must be removed from the analysis. To select the appropriate reaction channel, the selection is made on the charged fragments detected by the Sweeper detectors.

The process of selecting the fragments of interest is referred to as “particle identification” (PID). PID is a two-step process in which the detected fragments are separated by

Z (element identification), and then within a given element, they are separated by A (isotope identification). Once individual isotopes of the desired elements have been separated, software gates can be made to select events with a given species of fragment in the final state.

Element identification is done using the energy loss of the charged fragments as they pass through the ionization chamber detector. From the well-known Bethe-Bloche formula for the energy loss of non-relativistic heavy ions, the stopping power is related to the Z of the fully-stripped ion by:

$$-\frac{dE}{dx} = Z^2 f(v) \tag{4.7}$$

where $f(v)$ is some function that depends on the speed of the ion, but not its charge [85]. The speed of the ion is related in the obvious way to its time-of-flight (ToF). So a 2D histogram of the ion chamber energy loss versus ToF between the target and thin scintillators will show bands of constant Z^2. Then, an element can be selected in software by drawing a 2D gate around the corresponding band in the 2D histogram. An example is shown in Figure 4.13.

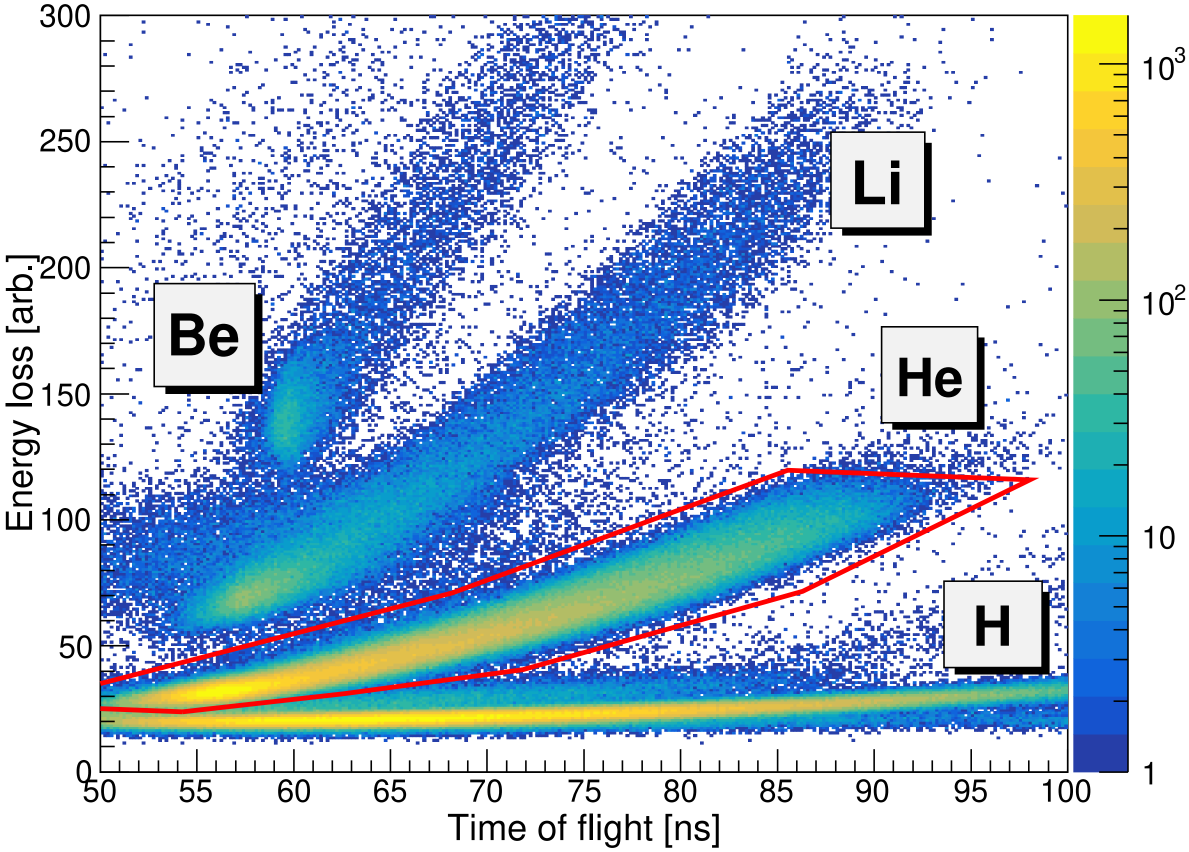

Figure 4.13: Element identification for the ^{11}Be beam. The helium element gate is shown in red. A similar gate can be made for other elements, and the same procedure is followed for the ^{12}B beam.

After element identification is complete, all that remains for PID is separating out the isotopes of the desired element. The Sweeper magnet produces dispersion of the fragments based on magnetic rigidiy ($B\rho = p/q$). The Sweeper magnet current was set such that particles with the rigidity of ^{8}He should travel along the design trajectory, and given that the neighboring isotopes of helium are unbound, isotope separation in this case mainly just entails separating ^{8}He from ^{6}He. This can be done by simply plotting the dispersive phase space coordinates (x, θ_x) of the fragments at the CRDCs. The plot should show two main groups, one corresponding to ^{8}He, and one corresponding to ^{6}He (with some contamination due to leakage of other particles into the helium Z gate). If the Sweeper current is indeed set to center ^{8}He, then the group which crosses $(x, \theta_x) = (0, 0)$ will be ^{8}He, and the other will be ^{6}He. In order to improve separation, one can include the correlations of the phase space coordinates with the ToF. For simplicity, rather than looking at the full 3D correlation between these three variables, one can define a "corrected angle" which is some nonlinear (typically quadratic) combination of the x and θ_x coordinates, and then plot that quantity against the ToF from the target to thin scintillators. At this point, a 2D gate can be drawn around the group of interest, or if desired, the distribution can be rotated and projected onto an axis in order to make 1D isotope ID gates (see Figure 4.14). If the isotope separation is not very clean, making 1D gates is less arbitrary than just drawing a 2D gate around each group. However for this experiment where the fragments are light and with some of the neighboring isotopes being unbound, the different isotopes are very well-separated, and it is straightforward to omit the last step and simply draw 2D isotope ID gates.

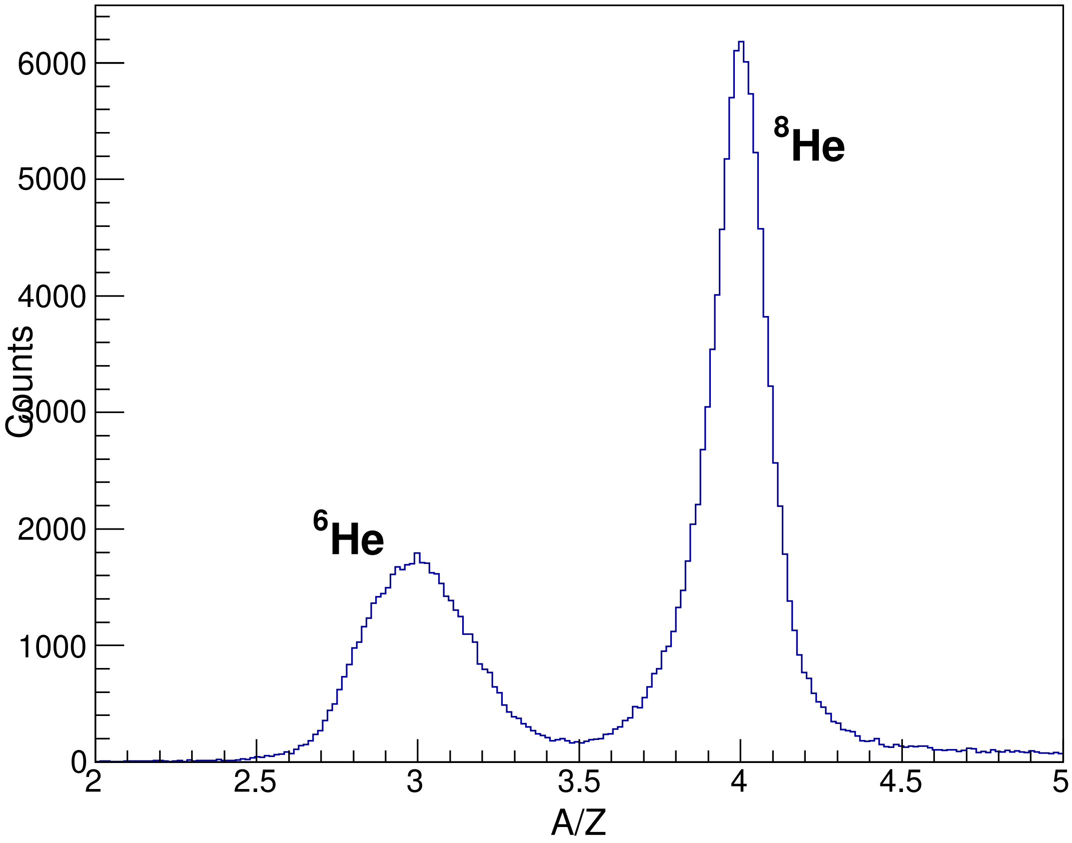

Figure 4.14: 1D helium isotope identification for the ^{11}Be beam.

4.2.4 Neutrons

Once the charged particle event selection is complete, a MoNA-LISA spectrum in coincidence with the desired fragment can be made. This spectrum will in general contain neutrons which are in true coincidence with the fragment, and unwanted accidental coincidences with photons or muons. In order to remove the spurious photon and muon events from the decay energy spectrum, one last event selection is made on the MoNA-LISA data in order to isolate neutrons. The “neutron gate” used in this analysis is a combination of two 1D cuts based on the MoNA-LISA time and light output spectra. The neutrons should appear in the MoNA-

LISA velocity spectrum as a peak around the beam velocity, and a 1D cut can be made around that peak (equivalent to a 1D cut in time-of-flight). If further suppression of the background is necessary, an additional 1D cut can be made to remove events of very low light output. The neutron gate used in this analysis is shown in Figure 4.15.

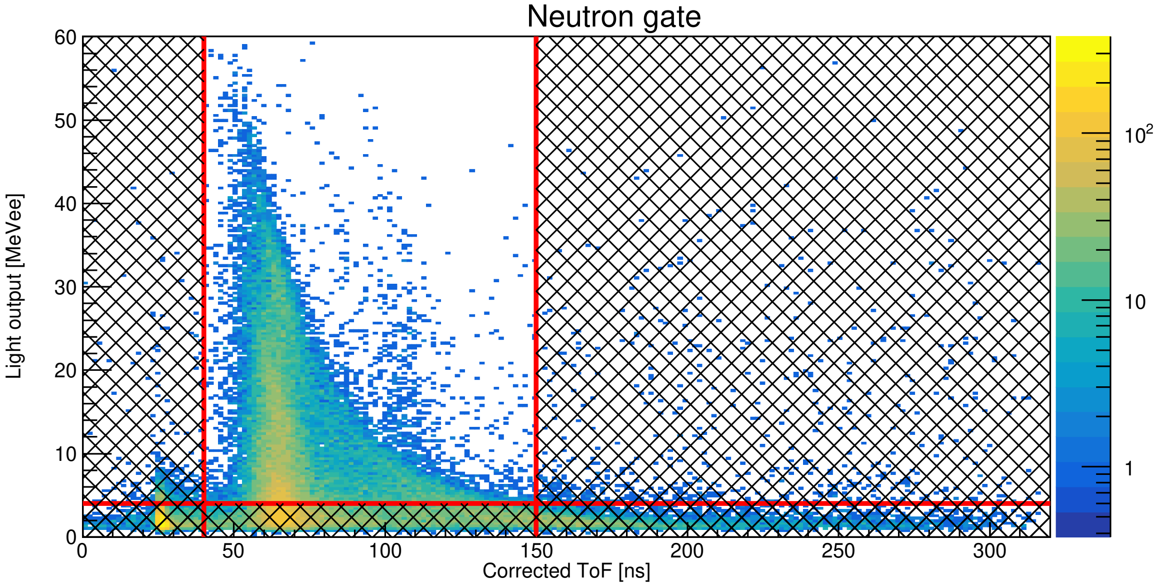

Figure 4.15: Neutron selection for the ^{11}Be beam. The same cuts are made on the ^{12}B data. The corrected ToF is the ToF, position-corrected as if the interaction had occurred in the front and center bar of the array. Events which lie above the horizontal line and between the vertical lines are identified as neutron events. All others (within the cross-hatched area) are presumed to be cosmic muons or photons, and are removed from the analysis.

4.3 Fragment tracking

Because the neutrons are not significantly scattered or slowed in the air, measuring the 3D position vector and time-of-flight of the neutrons between the target position and MoNA-LISA determines its four-momentum vector immediately after the decay. The fragments, on the other hand, are measured after having their paths bent through the Sweeper magnet. So the measured fragment positions and angles at the CRDCs need to be mapped to the angles and energy before entering the Sweeper magnet. This mapping is done using a nonlinear ion-optics calculation with the program COSY INFINITY. The details of COSY INFINITY will not be explained here, but the interested reader should consult Reference [86].

The purpose of an ion-optics calculation is to relate the phase space coordinates of the beam in one part of the beamline to the phase space coordinates of the beam in another part of the beamline. Instead of working with the standard (x, p_x, y, p_y, z, p_z) phase space coordinates, COSY INFINITY uses a more convenient set of coordinates, labeled by $\vec{Z} = (x, a, y, b, \ell, \delta)$, where

$$a \equiv \frac{p_x}{p_z} = \tan\theta_x \approx \theta_x \tag{4.8}$$

$$b \equiv \frac{p_y}{p_z} = \tan\theta_y \approx \theta_y \tag{4.9}$$

$$\ell \equiv -\frac{v_0\gamma_0}{1+\gamma_0}(t - t_0) \tag{4.10}$$

$$\delta \equiv \frac{K - K_0}{K_0} \approx 2\frac{\Delta p}{p} \tag{4.11}$$

The subscript 0 denotes the reference particle, which travels exactly along the design trajectory, with exactly the design energy. In words, a and b represent angles transverse to the beam direction, ℓ is a “time-of-flight-like” variable which is not relevant to this analysis, and δ is the normalized deviation from the kinetic energy of the reference particle. For a more detailed discussion of this choice of coordinates, the interested reader is directed to Reference [87].

With these coordinates established, the equations of motion for a charged particle in the electric and magnetic fields of a given beamline element can be solved for the elements of a matrix transformation $M(s'|s)$ such that:

$$\vec{Z}(s') = M(s'|s)\vec{Z}(s) \tag{4.12}$$

This linear transformation can be extended to higher orders, where nonlinear terms are included as well, and M is no longer a square matrix. COSY INFINITY uses differential algebraic methods to solve these equations of motion to arbitrary order for the elements of the transfer matrix. For this particular case, a matrix is needed which relates the phase space coordinates at the target position (denoted "t") to the phase space coordinates at the CRDC1 detector (denoted "d"):

$$\vec{Z}_d = M(d|t)\vec{Z}_t \tag{4.13}$$

Because the measured quantities are those at the CRDCs, this equation must be inverted:

$$\vec{Z}_t = M^{-1}(d|t)\vec{Z}_d \tag{4.14}$$

For this analysis, the optics calculation was carried out to third order, and the elements of M were provided by COSY INFINITY.

Not all 6 phase space dimensions are relevant for this analysis, so following the procedure in Reference [77], the dimensionality can be reduced, and the transfer matrix can be "partially inverted" to yield a set of equations of the form:

Table 4.4: The common inputs to COSY used for all settings in this analysis.

Parameter:	Value:	Significance:
order	3	Order of the optics calculation
angle	-0.3°	Incoming beamline angle
pos	0.50 m	Conversion between COSY coordinates and field map coordinates
drift	1.5791 m	Arc length of the design trajectory through the field map

$$\begin{pmatrix} a_t \\ y_t \\ b_t \\ \ell_t \\ \delta \end{pmatrix} = M_{PI}(d|t) \begin{pmatrix} x_d \\ a_d \\ y_d \\ b_d \\ x_t \end{pmatrix} \tag{4.15}$$

The outputs relevant to the decay energy are a_t, b_t, and δ, and the measured inputs are x_d, y_d, a_d, and b_d. The horizontal position at the target (x_t) is not a measured quantity, so it must be assumed that the incoming beam distribution is a Dirac delta function at $x = 0$. This is an approximation, and it contributes to the total systematic uncertainty on the final result.

The inputs required to generate the partial inverse matrix are the properties of the beam particle (A, q, and reference $B\rho$), and geometric properties of the beamline, such as its incoming angle, and the arc length of the design trajectory through the Sweeper field map. The value of the inputs common to all settings in this experiment are displayed in Table 4.4. A text file containing $B_y(x, z)$ in the midplane of the Sweeper magnet is also supplied. It can be shown by Fourier-transforming Ampère's law that the magnetic field in the midplane fully determines B_y everywhere inside the gap. The fringe field extends slightly outside the Sweeper gap, and is modeled using Enge functions. It is assumed due to the design of the

Table 4.5: Sweeper current, magnetic field, and rigidities for various settings used in this work. The Hall probe is physically located near the edge of the magnet, so the Hall probe value is not indicative of the central field strength, which is usually on the order of 1 Tesla.

Setting:	Current [A]:	Hall probe [kG]:	Bρ [Tm] for 43.3° bending:
Centered ^{11}Be	211	-7.307	2.60
Centered ^{12}B	173	-6.179	2.26
Centered ^{8}He	355	-10.70	3.81

magnet that B_x and B_z are negligible.

These midplane text files are generated using the magnetic field strength measured by a Hall probe inside the Sweeper gap. The Sweeper field was characterized using a 3D Hall probe scan at various currents, so using the measured Hall probe values, one can interpolate between the measured 2D field values to determine the midplane map at any given value of the Hall probe field. The relationship between the Sweeper current setting, the measured magnetic field strength at the Hall probe location, and the design trajectory rigidity needed to produce a bending angle of 43.3° is shown in Table 4.5.

4.4 Simulation

Once the quantity of interest (i.e., the decay energy or relative velocity) is calculated in data, it must be compared with simulations in order to fit a decay model to the experimental data. Monte Carlo simulations including the incoming beam parameters, target energy loss, knockout reaction kinematics, neutron emission decays, propagation of the neutrons and fragments into the detectors, and detector resolutions/acceptances are used for the comparison. The simulation code is a combination of an in-house fragment simulation package called ST MONA, and a GEANT4 [88, 89] simulation for the neutrons. The neutron physics package used in the GEANT4 portion of the code is MENATE_R.

The transverse phase space coordinates of the incoming beam are modeled in ST MONA by Gaussian distributions with tunable means and standard deviations. The kinetic energy distribution is modeled using a uniform distribution, with the center and width fixed by the A1900 rigidity and slit settings. The beam is then propagated through the target, including energy losses and straggling, until a randomly-chosen position where the reaction occurs. The dynamics of the knockout reactions are modeled within the Glauber formalism using a longitudinal momentum kick from the model of A. S. Goldhaber [90] and a transverse momentum kick from the model of K. Van Bibber, *et al.* [91]. Following the reaction, a decay energy is randomly generated according to some input distribution, and the two-body decay is simulated using the TGenPhaseSpace class in ROOT. The fragments are then propagated to the end of the target, where the COSY forward matrix is used to propagate the fragments to CRDC1, and a drift is applied to reach CRDC2. Realistic spreading based on the resolution of the CRDC detectors is applied to the pseudodata, and then the COSY inverse matrix is applied to reconstruct the fragment angles and energies at the target, in order to treat the simulated pseudodata identically to the real data. The simulated neutron energies and momenta are written to a file which is used as input to the GEANT4 part of the code, which propagates the neutrons from the target position into the MoNA-LISA array. The GEANT4 simulation contains a realistic model of the detector response, including timing and position resolutions, and a calculation of the light output using Birks' model [92]. The simulation package has been extensively benchmarked and characterized in previous works (Refs. [76, 79, 80, 1, 6, 5]).

The main tunable parameters in the simulation can be divided into three classes: incoming beam parameters, reaction parameters, and decay parameters. Each of these quantities must be systematically set in order to force the simulation to best reproduce the data. Each

Table 4.6: The simulated beam parameters used in this analysis.

Parameter:	Value for ^{11}Be:	Value for ^{12}B:	Significance:
eBeam	43.27	43.94	Beam energy [MeV/u]
beamA	11	12	Beam A
beamZ	4	5	Beam Z
targA	9	9	Target A
targZ	4	4	Target Z
dEbeam	0.01	0.01	Fractional width of energy distribution
bSpotCx	-0.005	-0.003	Beam spot x centroid [m]
bSpotCtx	-0.010	-0.011	Beam spot θ_x centroid [rad]
bSpotCy	-0.001	-0.005	Beam spot y centroid [m]
bSpotCty	0.000	0.001	Beam spot θ_y centroid [rad]
bSpotDx	0.0095	0.0093	Beam spot x width (σ) [m]
bSpotDy	0.0070	0.0070	Beam spot y width (σ) [m]
bSpotDtx	0.0100	0.0093	Beam spot θ_x width (σ) [rad]
bSpotDty	0.0041	0.0044	Beam spot θ_y width (σ) [rad]
bSpotSxtx	0.0000	-0.0012	Beam spot $x - \theta_x$ correlation [(m rad)$^{1/2}$]
bSpotSyty	0.0013	-0.0008	Beam spot $y - \theta_y$ correlation [(m rad)$^{1/2}$]

set of parameters will be covered in the following subsections.

4.4.1 Beam parameters

The incoming beam parameters can be fixed directly to measured values (i.e. the beam energy and A1900 momentum acceptance), or via some kind of minimization procedure. In order to set the parameters of the Gaussian distributions modeling the transverse phase space coordinates of the incoming beam, the measured CRDC distributions from a target-out run can be used. When there is no target in the beamline, and the Sweeper current is set to center the unreacted secondary beam, the beam propagates into the CRDCs without any reactions or energy losses. The incoming beam parameter space can then be scanned in order to best reproduce the CRDC data. The results of this procedure, for the ^{11}Be beam, are shown in Figures 4.16, 4.17, and 4.18, and the parameter values are displayed in Table 4.6.

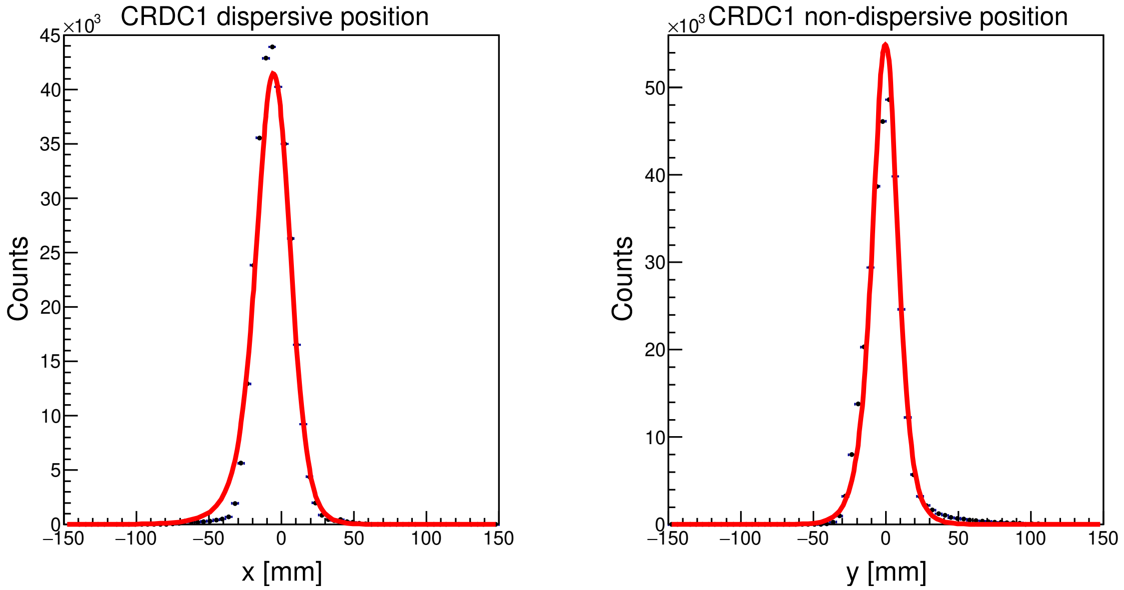

Figure 4.16: Comparison of the CRDC1 position distributions between data and simulation for the ^{11}Be beam. The data were taken in a target-out run, where the Sweeper magnet was set to center the unreacted beam (Run 2005). The points are data and the curves are simulation. The same comparison was done for the ^{12}B (Run 2026).

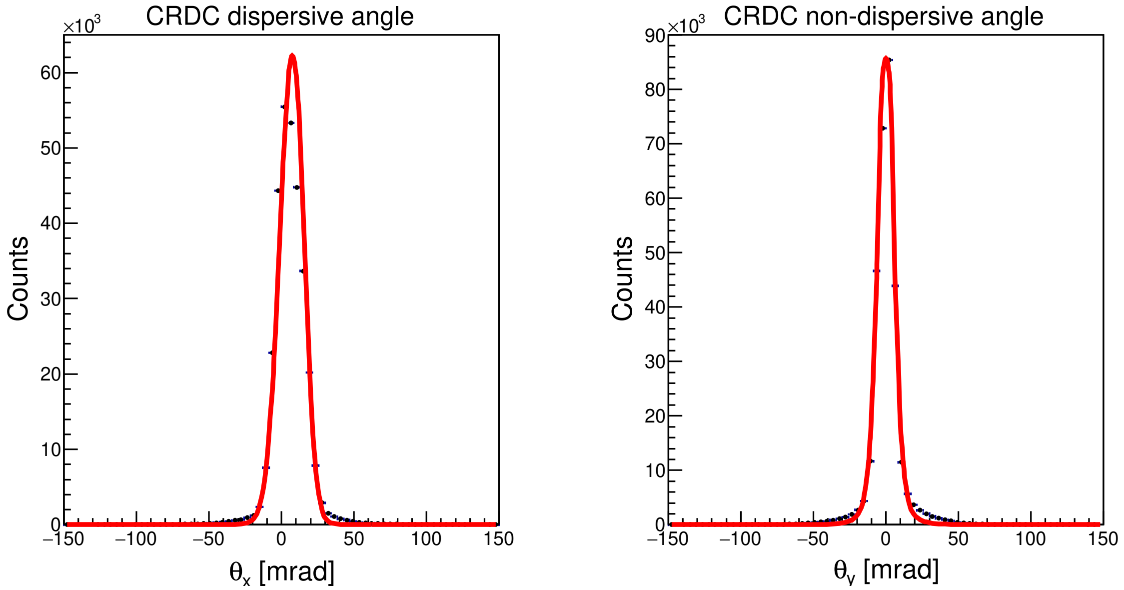

Figure 4.17: Comparison of the CRDC angle distributions between data and simulation for the ^{11}Be beam. The data were taken in a target-out run, where the Sweeper magnet was set to center the unreacted beam (Run 2005). The points are data and the curves are simulation. The same comparison was done for the ^{12}B (Run 2026).

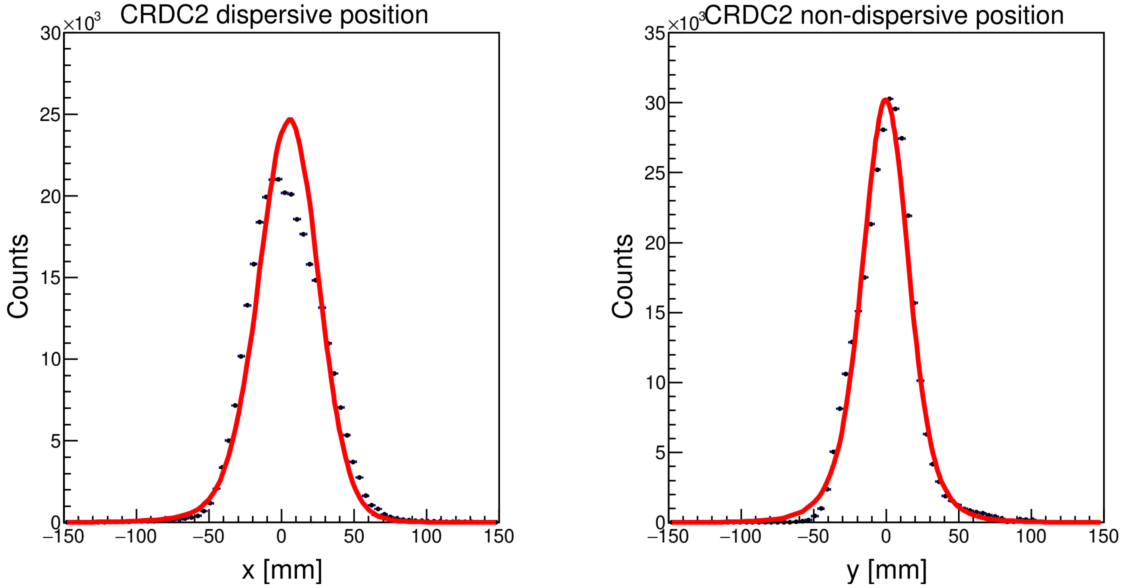

Figure 4.18: Comparison of the CRDC2 position distributions between data and simulation for the ^{11}Be beam. The data were taken in a target-out run, where the Sweeper magnet was set to center the unreacted beam (Run 2005). The points are data and the curves are simulation. The same comparison was done for the ^{12}B (Run 2026).

4.4.2 Reaction parameters

Once the incoming beam parameters have been set based on target-out runs, target-in runs can be used to fix the reaction parameters. The presence of the target causes both energy losses and reactions to occur. Because the fragment of interest has a low Z, energy losses are not very significant ($\sim$ 4 MeV for ^{8}He over half the target thickness), but they are easy to correct for with energy loss calculations. More significant, however, are the energy and momentum kicks provided to the reaction products by the knockout reactions.

As mentioned previously, the knockout reactions are modeled using the Glauber model, which includes transverse and longitudinal momentum kicks as discussed in Refs. [90, 91]. However these models were developed for high-energy fragmentation reactions, while the energies relevant to this analysis are somewhat lower. So in order to ensure that the reaction model is best reproducing the physics of these reactions, additional scale factors are used to tune the strength of the transverse and longitudinal momentum kicks.

The three parameters used in this work are a transverse scale factor, a longitudinal scale factor, and a velocity scale factor. The momentum kicks from the Glauber model are both in the form of Gaussian distributions with zero mean, and some standard deviations (the functional forms are given in Refs. [90, 91]). The transverse and longitudinal scale factors are just scaling the widths of these Gaussian distributions. The velocity scale factor is a scaling applied directly to the fragment velocity, and can be used to represent an energy kick given to the fragment by the knockout reaction.

The values of these parameters are chosen in order to simultaneously minimize the differences between the fragment kinetic energy and fragment dispersive position distributions between data and simulation for target-in runs. The Kullback-Leibler divergence (Equation 4.16) is used to quantify the difference between the histogrammed data (q) and pseudodata (p). The summation runs over histogram bins.

$$D(p||q) = \sum_i p_i \ln\left(\frac{p_i}{q_i}\right) \tag{4.16}$$

The method is simply a brute force search over a predefined parameter space to find the values which simultaneously minimize the K-L divergences for the fragment kinetic energy and fragment x. The velocity shift parameter space searched was the interval $[1.00, 1.04]$, in steps of 0.01, and the Glauber scale parameter spaces searched were $[0.0, 1.5]$ in steps of 0.5. The minimization process was performed separately for each beam, as these parameters relate to the specific reaction which is occurring, and the reactions of interest are different for the two different secondary beams. The results are shown in Figure 4.19 and Table 4.7.

Table 4.7: The simulated reaction parameters.

Beam:	Longitudinal scale:	Transverse scale:	Velocity scale:
^{11}Be	1.0	0.0	1.02
^{12}B	1.0	0.5	1.02

The plots in Figure 4.19 are on a logarithmic scale to emphasize the disagreements in the tails. In spite of these disagreements, the shapes and locations of both peaks are fairly well-reproduced in simulation, given the simplicity of the reaction model.

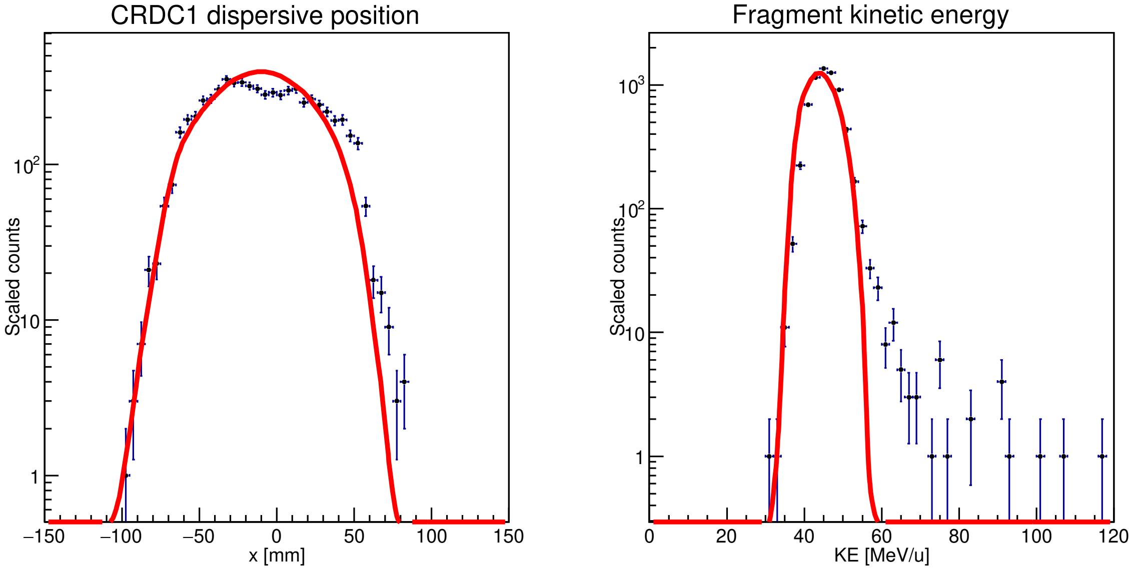

Figure 4.19: Comparison of the CRDC1 x and fragment kinetic energy distributions between data and simulation for the ^{11}Be beam. The data were taken from a chain of target-in runs. The points are data and the curves are simulation. The same comparison was done independently for the ^{12}B beam.

4.4.3 Decay parameters

Once the beam and reaction parameters are fixed, all that remains is to find the parameters of the neutron decay lineshape(s). The decay lineshape functions are discussed in detail in Chapter 2.

In this work, all s-wave decays are parametrized by a scattering length, denoted by a. All decays with $\ell > 0$ are parametrized by a resonance energy, denoted by E, and a resonance width, denoted by Γ. Backgrounds are modeled phenomenologically using a Maxwellian function:

$$f(E;\Theta) \propto \sqrt{E}\exp\Big(-E/\Theta\Big) \tag{4.17}$$

The Maxwellian function has a single free parameter, Θ. The Maxwellian function is a good model for the background in a MoNA-LISA-Sweeper experiment because it produces a decay energy spectrum resembling coincidences between correlated fragments and neutrons when convolved with the experimental response function. This model has been used in many previous MoNA works, and typical values of the parameter Θ range between $\sim 1 - 5$ MeV.

In addition to these "intrinsic" parameters, there are scale factor parameters whenever more than one component is included in the fit. If the fit contains N components, then there are $N - 1$ free scale factor parameters, with the overall scale of the summed spectrum being used to normalize simulation to data.

The values of the decay parameters are determined using standard statistical techniques for parameter estimation, to be discussed in the next section.

4.5 Parameter estimation

4.5.1 Binned likelihood parameter estimation

This section will describe the use of likelihood maximization for parameter estimation, following the treatment in the data analysis textbook by G. Cowan [93].

An experimental data set can be thought of as a sequence of random values drawn from some underlying probability density function (PDF). Then, one can assume some functional form of the PDF, and try to estimate the values of its parameters from the experimental data. One method for doing so is known as maximum likelihood parameter estimation. The idea behind maximum likelihood is very simple: just find the values of the parameters of some assumed PDF such that the probability of observing the experimental data given those parameters is maximal. Mathematically, the goal is to find:

$$\hat{\theta} \equiv \underset{\vec{\theta}}{\operatorname{argmax}} \, L(\vec{\theta}) = \underset{\vec{\theta}}{\operatorname{argmax}} \, f_{joint}(\vec{x}|\vec{\theta}) \tag{4.18}$$

The quantity $L(\vec{\theta})$ is known as the "likelihood function". $f_{joint}(\vec{x}|\vec{\theta})$ is the joint PDF for observing the data $\vec{x}$, given the parameters $\vec{\theta}$. For independent and identically-distributed data, the joint PDF is simply a product of PDFs for the individual components of the data vector. For computational ease, it is typical to instead maximize the logarithm of the likelihood function, since the logarithm is a monotonic function.

In this approach, the values of the estimators of the parameters can be determined by finding the values of $\vec{\theta}$ that maximize $\log L(\vec{\theta})$, and the statistical uncertainties and correlations of the estimators can be estimated (assuming the estimators are unbiased) using:

$$\hat{V}_{ij}^{-1} = -\left.\frac{\partial^2 \log L(\vec{\theta})}{\partial\theta_i \partial\theta_j}\right|_{\vec{\theta}=\hat{\theta}} \tag{4.19}$$

For purposes of this work, we will be concerned with the summation running over N bins in a histogram, where the number of counts in the bins (n_i, $\sum_{i=1}^{N} n_i \equiv n_{tot}$) can be treated as independent variables with means $\nu_i = \nu_i(\vec{\theta})$, with a joint probability density given by a multinomial distribution:

$$f_{joint}(\vec{n},\vec{\nu}) = n_{tot}! \prod_{i=1}^{N} \frac{1}{n_i!}\Big(\frac{\nu_i}{n_{tot}}\Big)^{n_i} \tag{4.20}$$

The logarithm of this joint PDF is then equal to:

$$\log f_{joint} = \log(n_{tot}!) + \sum_{i=1}^{N} \Big[n_i \log \nu_i(\vec{\theta}) - \log(n_i!) + n_i \log n_{tot} \Big] \tag{4.21}$$

The terms which do not depend on the values of $\vec{\theta}$ are irrelevant to the maximization, so they can be dropped, and what remains is:

$$\log L(\vec{\theta}) = \sum_{i=1}^{N} n_i \log \nu_i(\vec{\theta}) \tag{4.22}$$

In this analysis, this log-likelihood function is maximized with respect to $\vec{\theta}$. The numerical algorithms used to maximize the $\log L$ in this work were either brute force in low-dimensional parameter spaces, or simulated annealing in high-dimensional spaces ($D > 5$). Brute force maximization is straightforward, and will not be explained further in this work. Simulated annealing will be discussed in the following section.

Finally, it is useful to consider the special case of a likelihood function of only one parameter. Near the maximum, the log-likelihood can be Taylor-expanded to give:

$$\log L(\theta) = \log L(\hat{\theta}) - \frac{(\theta - \hat{\theta})^2}{2\hat{\sigma}_{\hat{\theta}}^2} \tag{4.23}$$

The constant term is simply $\log L_{max}$, and the linear term is zero at a maximum. Equivalently, this equation says:

$$\log L(\hat{\theta} \pm \hat{\sigma}_{\hat{\theta}}) = \log L_{max} - \frac{1}{2} \tag{4.24}$$

This gives way the graphical method of quantifying statistical uncertainties. The 1σ statistical uncertainty of the estimator $\hat{\theta}$ is given by the points where the log-likelihood decreases from its maximum value by 1/2.

In the case of more than one parameter, a profile likelihood method was used to determine statistical confidence intervals and limits. In this method, the likelihood as a function of D parameters is first maximized with respect to $D-1$ of its parameters, and then the 1D "profile likelihood" is scanned in the final dimension. The 1σ interval is then given by the locus of points near the maximum such that:

$$2\Delta\Big(\log L(\theta)\Big) < Q_{D-1}(\alpha) \tag{4.25}$$

where $Q_{D-1}(\alpha)$ is the quantile of the chi-squared distribution for a significance α, with $D-1$ degrees of freedom. Finding the interval simply entails using the graphical method, but with 1/2 replaced by $Q_{D-1}(\alpha)/2$.

4.5.2 Simulated annealing

In order to minimize the $\log L$ function in the 7-dimensional parameter space for the ^{12}B(-3p)^{9}He reaction, a stochastic hill climbing (SHC) algorithm coupled with simulated annealing (SA) was used. The algorithm was developed because the 7D space was too large to do a brute force search in a reasonable amount of time. The SHC allows maxima to be found without having to iterate over the entire space, and the SA prevents the maximizer from getting trapped in local maxima. With an appropriately chosen "cooling schedule" and hyperparameters of the algorithm, it can be made to converge to the true global maximum with a probability arbitrarily close to 1.

The SHC algorithm employed for this analysis was simply a random Gaussian step, sampled from an uncorrelated 7-dimensional Gaussian distribution with mean $\vec{0}$, and covariance matrix $2\hat{I}$ (in the discretized parameter space). The initial point is sampled from a uniform distribution over the entire space. Then in each iteration, the subsequent point is chosen based on this Gaussian step distribution. If a value outside the specified volume of parameter space is chosen, that value is simply resampled until a valid value is obtained. With each step, an acceptance/rejection condition is applied, and the acceptance/rejection condition changes as a function of iteration number according to the cooling schedule of the SA.

Defining $\Delta(\log L) \equiv \log L_{current} - \log L_{proposed}$, the acceptance/rejection condition is as follows:

- if $\Delta(\log L) < 0$, accept the proposed point
- if $\Delta(\log L) \geq 0$, accept the proposed point with probability $e^{-\Delta(\log L)/T}$, otherwise, reject it

where T is the "temperature" of the SA algorithm. T is initialized to some pre-defined value (in this case, 5), and then it evolves as a function of Monte Carlo time according to the cooling schedule. The temperature is meant to start with a high value, which allows the maximizer to frequently jump in the direction of a worse $\log L$. This is what allows the algorithm to escape from local maxima, and eventually converge to the global maximum. A linear cooling schedule was chosen for this analysis, of the form $T_{new} = \alpha T_{old}$, where $\alpha = 0.9$. The criterion for the temperature to change was taken to be the number of consecutive rejections, N_{rej}, reaching a value of $N_{stays} \equiv 5$. In other words, if the maximizer decides to stay at the same point for five propositions in a row, the temperature decreases, and the algorithm continues. This process repeats until some predefined minimum temperature (in this case, 10^{-6}) is reached. As the temperature decreases in Monte Carlo time, it becomes more and more unlikely for a worse $\log L$ to be accepted, which forces to algorithm to stay near the maximum. However the fact that the steps are Gaussian means that there is a nonzero probability in any given sampling to propose any other point in the parameter space, no matter how far away it is. So even if the maximizer is somewhere on a large local maximum, it has the chance to escape.

In order to test convergence, random restarts were applied. This simply entails running the algorithm multiple times with random initial conditions, and verifying that it converges to the same maximum each time. The user can perform as many random restarts as they deem necessary to be convinced that they have found the true global maximum. Once the algorithm is known to be converging, the user can play with the values of the hyperparameters (initial temperature, minimum temperature, cooling rate, cooling criterion, Gaussian step size, etc.) in order to try to shorten the runtime of the algorithm. The number of iterations until convergence will vary each time the algorithm runs, but for this particular case, the total number of iterations before convergence tends to be on the order of $\sim 1\%$ of the total volume of the parameter space. So the global optimum of the 7D parameter space can be reached by iterating over a small fraction of the entire space. This allows the optimum values to be found much faster than with the brute force method. The name "simulated annealing" comes from the analogy of this procedure with annealing in materials science. Pseudocode demonstrating the entire combined algorithm (SHC+SA) is shown in the Appendix .

Chapter 5

Results and Discussion

5.1 ^{12}B(-3p)^{9}He

Figure 5.1 shows the invariant mass results for this reaction, which was expected to preferentially populate *p*-wave resonances. The shape of the experimental spectrum is not well-reproduced by any single input distribution, so it was fit with a combination of two *p*-wave Breit-Wigner resonances and a Maxwellian background. In this case, the likelihood maximization has seven variable parameters: the energy, width, and scale factor of each resonance ($3 \times 2 = 6$), plus the Θ parameter of the Maxwellian background. The log-likelihood between data and simulation was maximized in this 7D parameter space using the simulated annealing algorithm described in Section 4.5.2. The scale factors for the two BW distributions, and the Maxwellian Θ parameter were treated as nuisance parameters in the analysis, but best fit parameters and 1σ uncertainties were obtained for the resonance energies, and 1σ limits were obtained for the decay widths of the two BW distributions. The statistical uncertainty quantification for each parameter was done by fixing the values of the other parameters to their best estimates, and scanning the 1D profile of the log-likelihood function, using the "graphical method" described in Section 4.5.1. This is demonstrated for the first resonance energy in Figure 5.2. The systematic uncertainties were calculated by varying parameters of the analysis over a physically reasonable range and looking at the shift in the location of the likelihood maximum, following the procedure in the dissertation of M. D. Jones [6]. A breakdown of the uncertainties is shown in Table 5.1.

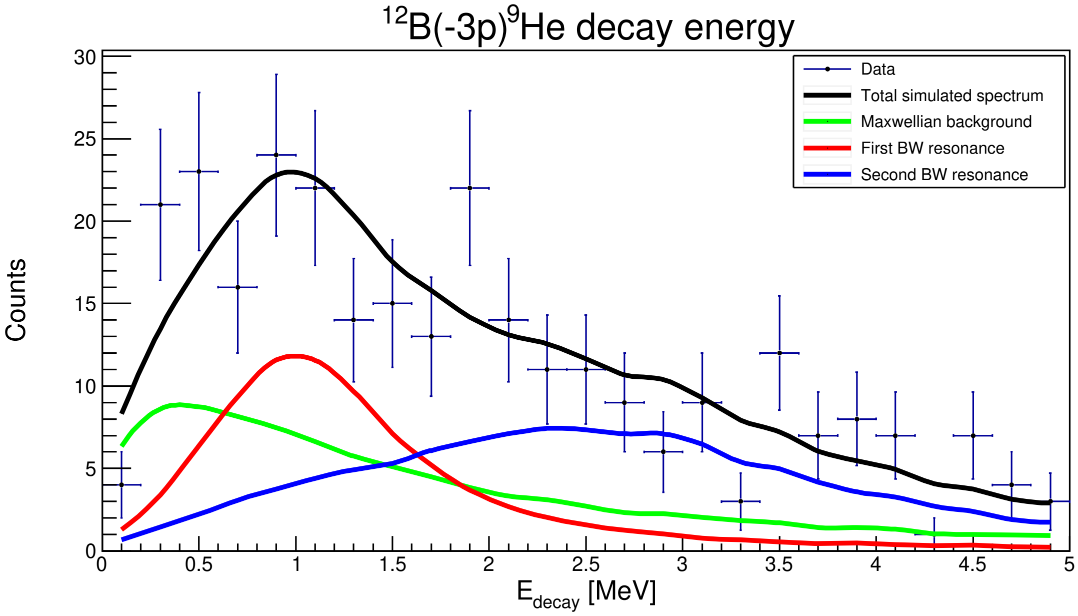

Figure 5.1: The decay energy spectrum from the ^{12}B(-3p)^{9}He reaction.

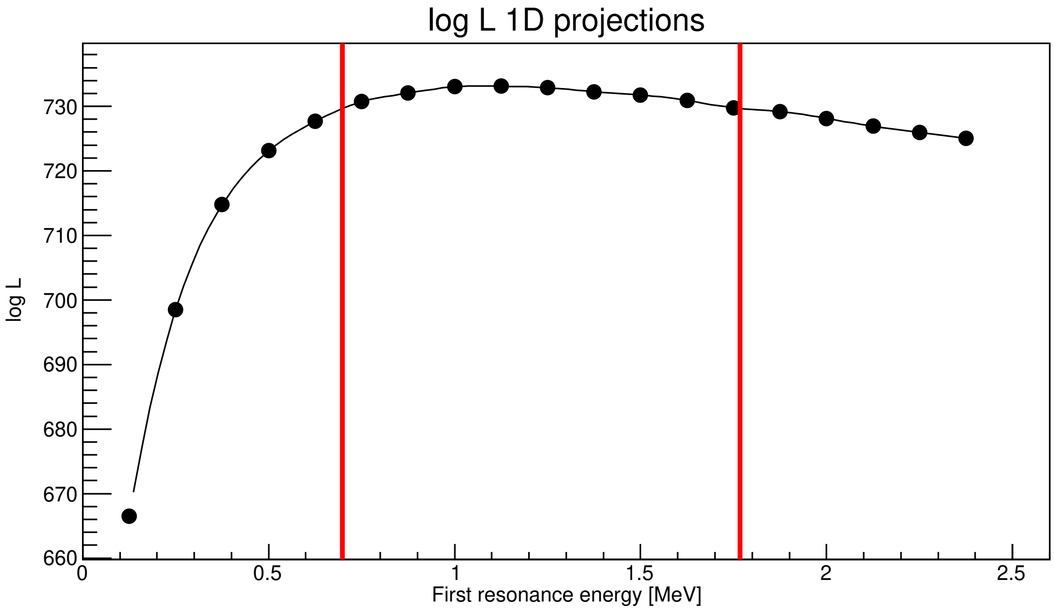

Figure 5.2: The likelihood maximization for the first resonance energy from the ^{12}B(-3p)^{9}He reaction. The points are the calculated likelihoods, and the black curve is a cubic spline interpolation. The red vertical lines correspond to the 1σ (stat.) error band.

Table 5.1: Statistical and systematic uncertainties in the fitting of the resonance parameters for ^{12}B(-3p)^{9}He. The values for the E_1 and E_2 parameters are for two-sided intervals, and the values for the Γ_1 and Γ_2 parameters correspond to one-sided deviations from the likelihood maximum.

	Fit values [MeV]:	1.1	2.3	3.1	2.8
Contribution:	Variation:	E_1 [keV]:	Γ_1 [keV]:	E_2 [keV]:	Γ_2 [keV]:
Statistical	–	$^{+700}_{-400}$	-1000	$^{+1000}_{-800}$	-1100
Target energy loss	±0.222 MeV	1.7	18.5	81.8	21.4
Global T_{mean} offset	±0.2 ns	0.03	43.2	143.9	74.2
Simulated θ_x mean	±15 mrad	22	30	20	13
CRDC1 x offset	±1 mm	20	13	46	45
CRDC2 x offset	±1 mm	21	31	3	24
COSY “drift”	±10 cm	37	98	118	174
Total systematic	–	52	118	209	238

The results of the fit suggest that there is a relatively low-lying p-wave resonance at $E = 1.1^{+0.7}_{-0.4}$ MeV ($\Gamma > 1.3$ MeV), and a higher-lying resonance at $E = 3.1^{+1.0}_{-0.8}$ MeV ($\Gamma > 1.7$ MeV). Due to the high energy and width of the higher-lying resonance, the p-wave and d-wave lineshapes cannot be strongly distinguished. A p-wave lineshape was assumed for the analysis, although a d-wave lineshape would fit the data similarly well. From both theoretical and previous experimental level schemes, no resonances with $J > \frac{5}{2}$ are expected to contribute within the range of decay energies that this experiment was sensitive to. The use of a p or d lineshape for the higher resonance does not affect the values of the other fitted parameters in a statistically significant way. The fit was also performed with the lower resonance replaced by a d-wave, but the scale factor for the first resonance was pushed to zero. Therefore, the lower resonance can be definitively assigned an ℓ of 1. The value of the Maxwellian parameter at the global likelihood maximum is $\Theta = 3.5$ MeV.

The presence of a p-wave resonance at about 1 MeV above the ^{8}He ground state is in close agreement with multiple previous experiments [36, 37, 38, 39, 41, 42, 44, 45, 46]. There are large variations in the experimental level schemes of the multipolarities and resonance energies of higher excited states, although many agree that $J = \frac{3}{2}$ and/or $J = \frac{5}{2}$ excited levels exist in the $\sim 2 - 5$ MeV range [36, 37, 38, 39, 41, 43, 46].

5.2 ^{11}Be(-2p)^{9}He

The ^{11}Be(-2p)^{9}He data are where ground state inversion of ^{9}He should be evident if it is present. The presence of an s-wave resonance with a large, negative scattering length would signal that ^{9}He has a significant contribution from an s neutron in the ground state. On the other hand, a scattering length close to zero would indicate weak final state interactions between the neutron and ^{8}He core, and suggest that there is no low-lying s state in ^{9}He. If the energy of the resonance is assumed to be $E \approx \frac{\hbar^2}{2\mu a^2}$, then for an s-wave resonance to have an energy less than 1 MeV, the scattering length must satistfy $|a| \lessapprox 5$ fm. In the limit of $a \to 0$, the s-wave simply becomes a "correlated background", where the halo of the ^{11}Be beam is broken up by the reaction, with no final state interactions between the neutron and fragment.

The comparison between experiment and simulations for this analysis were done as a maximum likelihood fit to the combination of the decay energy and relative velocity spectra. The simulations included two components: an s-wave, and a Maxwellian background, for a total of three paramaters: the s-wave scattering length, the Maxwellian Θ, and the relative scale factor. The scale factor is applied to the Maxwellian spectra before adding them to the s-wave spectra, so the scale factor represents the fractional contribution of the Maxwellian background. Because the parameter space has sufficiently low dimension, the fit was done using a brute force maximization. The first step is a coarse-grained fit to find the approximate global maximum, and then a more fine-grained fit around the maximum is performed to get accurate estimates of the uncertainties.

The coarse-grained search was performed over the regions $a \in (-16, 0]$ fm (step size of 1 fm), $\Theta \in (0, 6]$ MeV (step size of 0.5 MeV), and scale factor in $(0, 5]$ (step size of 0.5). The resulting decay energy spectrum is shown in Figure 5.3, and a 1D profile likelihood is shown in Figure 5.4.

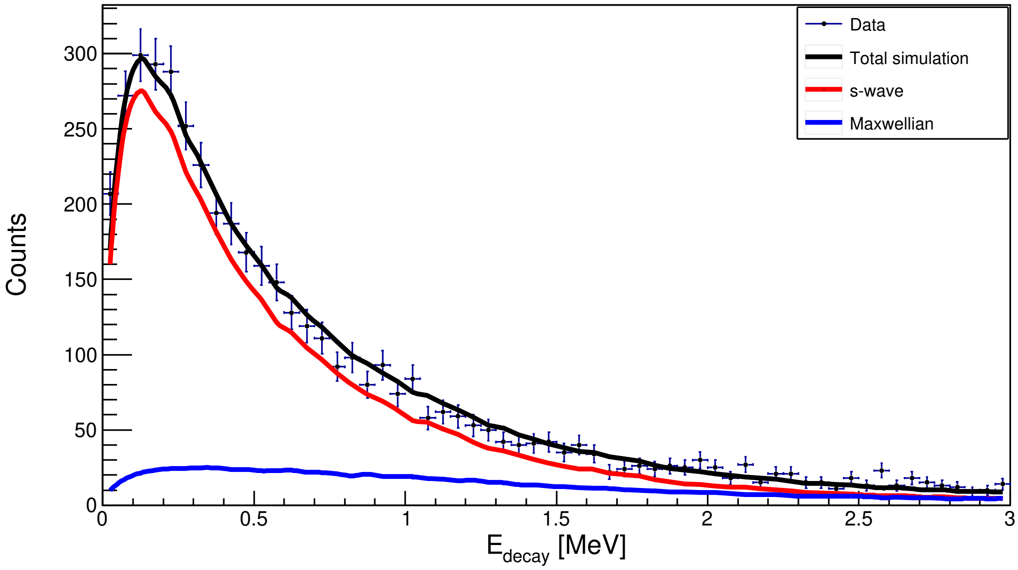

Figure 5.3: The ^{11}Be(-2p)^{9}He decay energy at the global maximum of the coarse-grained search. The simulated parameter values are $a = -2$ fm, $\Theta = 2.5$ MeV, and a relative scale factor of 0.5.

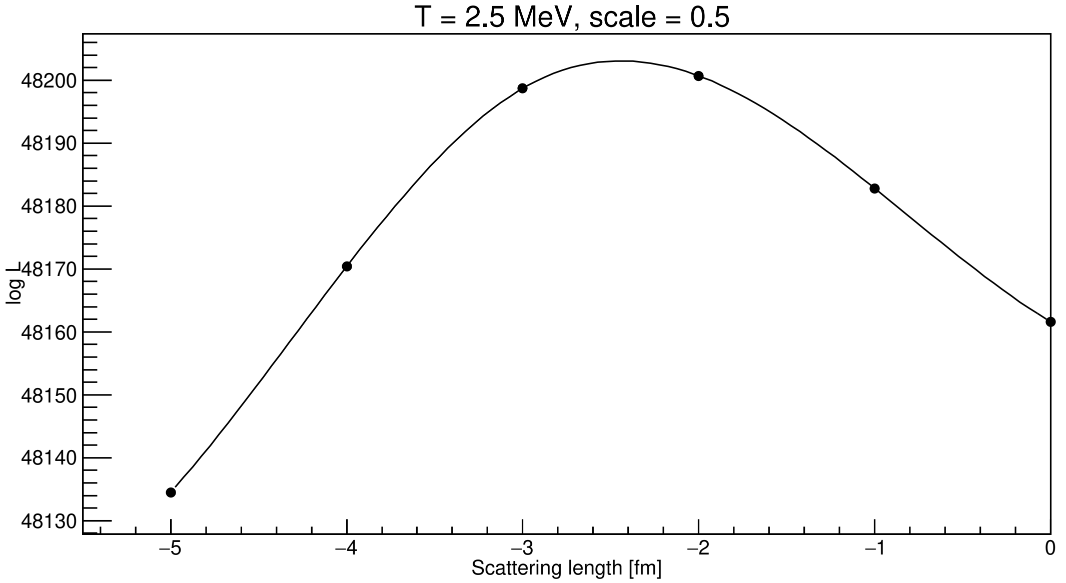

Figure 5.4: A 1D projection of the log-likelihood near the global maximum of the coarse-grained search. The points are the calculated log-likelihoods, and the curve is a cubic spline interpolation to guide the eye.

However, this result seems to show an abnormally small fractional contribution from background when compared with the previous measurements using the same technique, including that of L. Chen, *et al.* [40], which used the same exact reaction to populate ^{9}He. If the search space is limited to large values of the scale factor parameter, another maximum is found with $a = -7$ fm, $\Theta = 1.5$ MeV, and scale factor of 1.5, shown in Figures 5.5 and 5.6. Qualitatively, this represents a combination of s-wave and Maxwellian contributions similar in height, while in the previous case, the spectrum is dominated by the s-wave. The values of the scattering length parameter at these two likelihood maxima are markedly different, and have contradictory implications about whether or not inversion is present in the ground state of ^{9}He. The case with $a = -2$ fm would imply a non-observation of inversion, while the case with $a = -7$ fm would imply that ^{9}He is inverted in the ground state. The latter case seems to be more consistent with the observation made by Chen, *et al.*, where it was concluded that ^{9}He has an s-wave ground state.

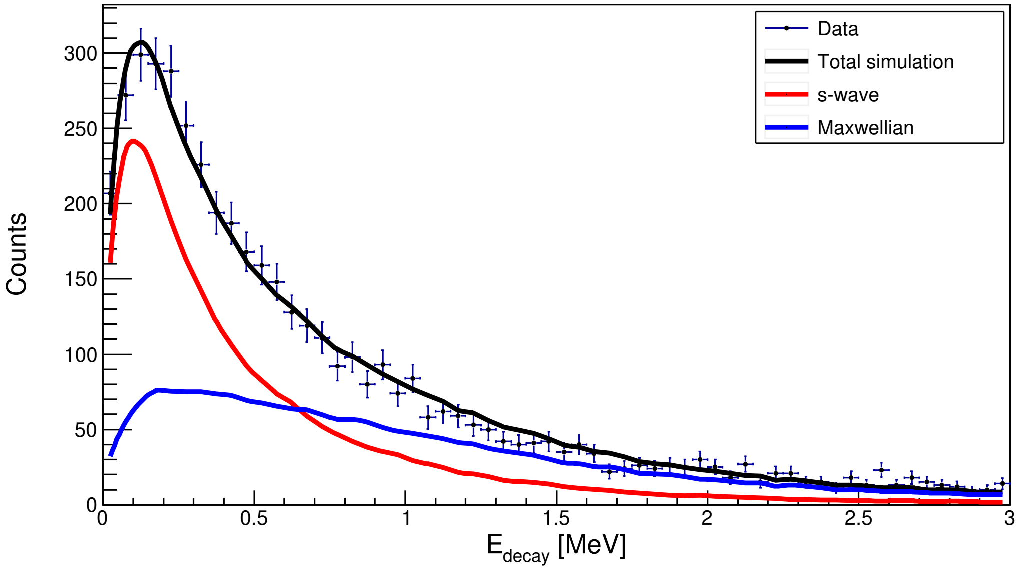

Figure 5.5: The ^{11}Be(-2p)^{9}He decay energy at the maximum in the restricted parameter space. The points are data and the curves are simulations. The simulated parameter values are $a = -7$ fm, $\Theta = 1.5$ MeV, and a relative scale factor of 1.5.

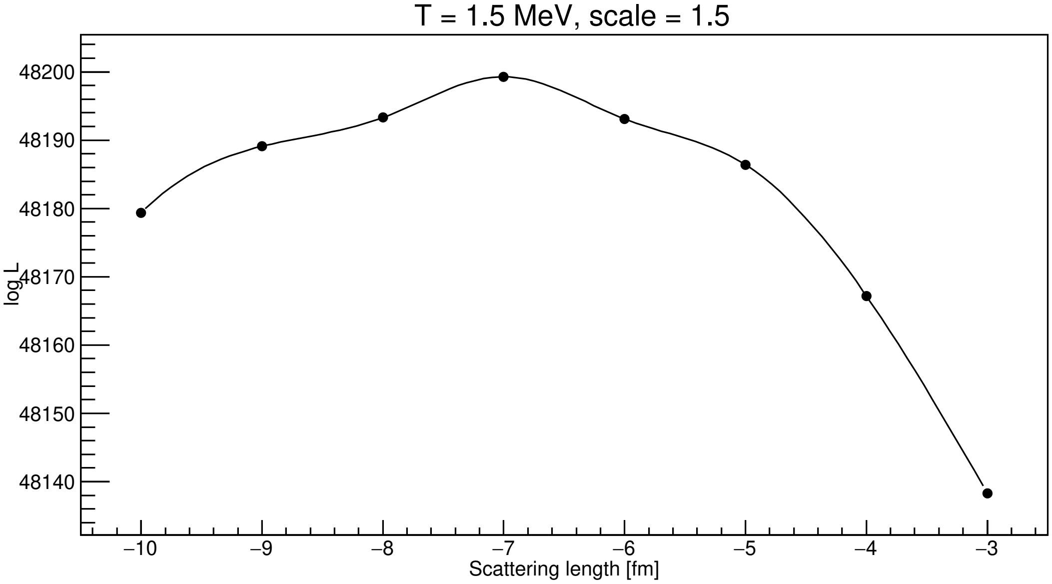

Figure 5.6: A 1D projection of the log-likelihood near the maximum of the coarse-grained search, when the parameter space has been restricted to large scale factors. The points are the calculated log-likelihoods, and the curve is a cubic spline interpolation to guide the eye.

In the analysis by Chen, *et al.*, the background was modeled using event mixing rather than a Maxwellian function. Event mixing assumes that the neutron and fragment are uncorrelated, and in random coincidence, and a background lineshape was generated by randomly selecting fragments and neutrons from different events, and calculating their relative velocities. However this background model is unrealistic, because any reaction or decay process which produces neutrons and fragments in coincidence will have kinematic correlations between the fragment and neutron. Therefore, the Maxwellian function is a more realistic background model for both this work and the work of Chen, *et al.*. Additionally, the Maxwellian Θ parameter and the scale factor parameter are correlated, because changing the value of Θ can push particles in and out of the geometric acceptance of the detectors, and therefore the scale factor has to be varied accordingly in order to achieve a good fit. Therefore, using this improved background model allows for access to a region of parameter space which was not searched by Chen, *et al.*, and this explains why the current analysis can produce seemingly ambiguous results while the Chen analysis did not.

On the other hand, a scattering length close to zero seems to be consistent with the conclusion of Uberseder, *et al.* [47], which states that if an s state exists, it must lie at several MeV above the neutron separation energy. Given the ambiguity of the current result, no definitive statement can be made about the ground state inversion of ^{9}He, but we can begin to understand why previous analyses have reached seemingly contradictory conclusions.

The fine-grained fit near the $a = -2$ fm maximum was performed over the range $a \in [-3, -1]$ fm in steps of 0.1 fm. The values and step sizes of the Θ and scale factor parameters were kept fixed. The global likelihood maximum was found at $a = -2.1 \pm 0.6$ (stat.) $\pm$ 0.2 (syst.) fm, $\Theta = 3.0$ MeV, and scale factor 0.5. The value of the Maxwellian Θ is slightly different between the fine- and coarse-grained fits, but the difference is only one unit in the discretization of Θ. The 1D profile likelihood near this maximum is shown in Figure 5.7.

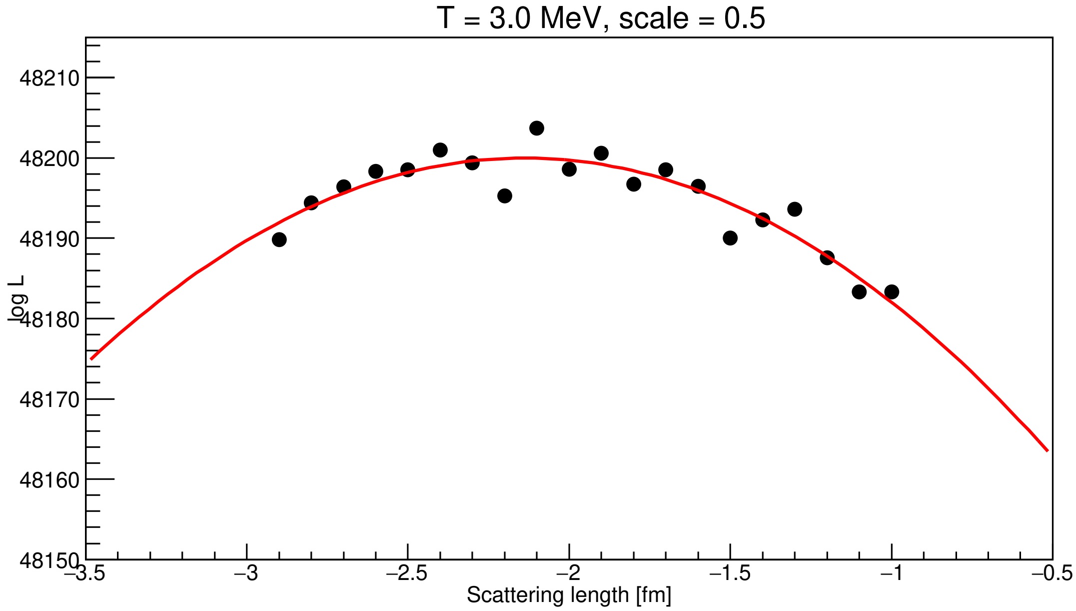

Figure 5.7: The 1D log-likelihood of fine-grained search around $a = -2$ fm. The points are the calculated log-likelihoods, and the curve is a parabolic fit.

For the $a = -7$ fm maximum, the fit range for the scattering length was $[-8, -6]$ fm, in steps of 0.1 fm, with the values of Θ and the scale factor fixed to 1.5 MeV, and 1.5, respectively. The likelihood maximum on this interval was found at $a = -6.8 \pm 1.2$ (stat.) ± 0.7 (syst.) fm. The 1D profile likelihood for this fit is shown in Figure 5.8.

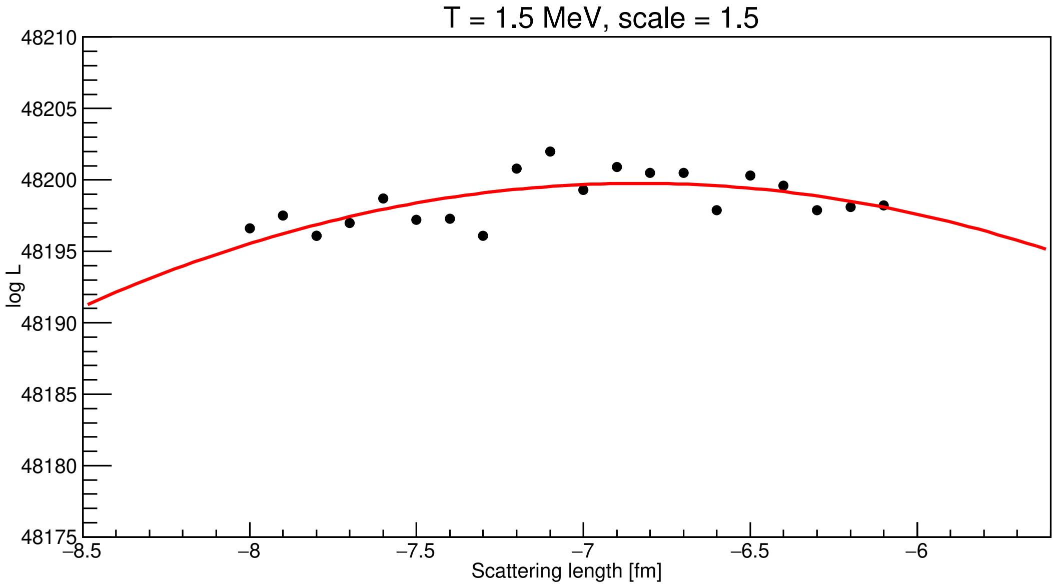

Figure 5.8: The 1D log-likelihood of fine-grained search around $a = -7$ fm. The points are the calculated log-likelihoods, and the curve is a parabolic fit.

The values of the log-likelihood at the -2 fm and -7 fm maxima are 48200.0 and 48199.8, respectively, so the difference between them is less than the 1σ deviation calculated from the quantile of the chi-squared distribution ($Q_{D-1}(\alpha)/2 \approx 1.15$). A breakdown of the statistical and systematic uncertainties for both maxima is shown in Table 5.2.

Table 5.2: Statistical and systematic uncertainties in the fitting of the scattering length for ^{11}Be(-2p)^{9}He.

Contribution:	Variation:	$a = -6.8$ fm:	$a = -2.1$ fm:
Statistical	–	1.2 fm	0.6 fm
Target energy loss	±0.222 MeV	0.1 fm	0.02 fm
Global T_{mean} offset	±0.2 ns	0.1 fm	0.04 fm
Simulated θ_x mean	±15 mrad	0.6 fm	0.16 fm
CRDC1 x offset	±1 mm	0.2 fm	0.09 fm
CRDC2 x offset	±1 mm	0.1 fm	0.02 fm
COSY "drift"	±10 cm	0.2 fm	0.12 fm
Total systematic	–	0.7 fm	0.22 fm
Total (rounded to 0.1 fm)	–	1.4 fm	0.6 fm

5.3 ^{12}B(-2p)^{10}Li

Resonances in ^{10}Li have been populated using a ^{12}B beam and Be target, albeit with a different beam energy, in a previous MoNA experiment [1]. In that work, invariant mass spectroscopy was used to fit a decay energy spectrum to a combination of three p-wave resonances. The results of that fit are shown in Table 5.3. These resonances can then serve as a benchmark for the current analysis, which aims to reconstruct ^{10}Li from a ^{11}Be beam using the Time-of-Flight method (see Section 3.5).

Table 5.3: ^{10}Li resonance parameters from the Ph.D. dissertation of J. K. Smith [1].

Multipolarity:	Resonance energy [keV]:	Width [keV]:	Population [%]:
$\ell = 1$	110 ± 40	200	13
$\ell = 1$	500 ± 100	800	55
$\ell = 1$	1100 ± 100	1000	32

Without any fitting or tunable resonance parameters, the resonances from the previous work can be simulated and overlaid with the data from the current work. The result is shown in Figure 5.9.

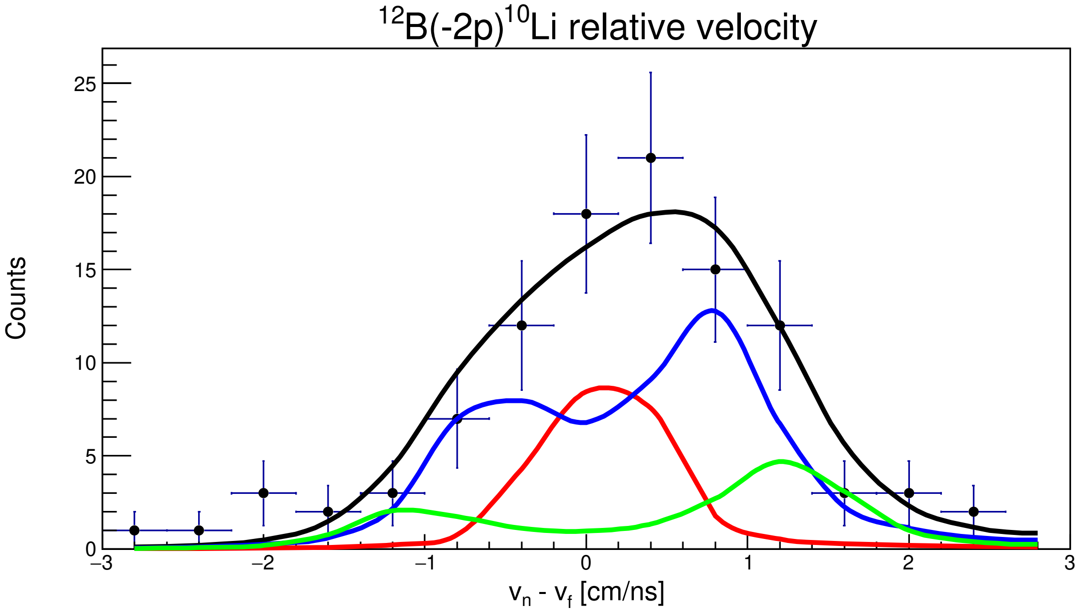

Figure 5.9: The relative velocity spectrum from the ^{12}B(-2p)^{10}Li reaction. The points are data from this work, and the curves are the simulations of the resonances from the previous work. The three resonances are shown individually in the red, green, and blue curves. The black curve is the combined simulation.

This demonstrates that the Time-of-Flight method correctly reconstructs previously-known states in ^{10}Li.

5.4 ^{11}Be(-1p)^{10}Li

Producing ^{10}Li using a neutron-halo beam should preferentially populate states with an s neutron. If such a state with a large scattering length (in absolute value) is observed in the relative velocity spectrum, it would indicate ground state inversion of ^{10}Li. In this work, the relative velocity spectrum was produced using the ToF method (see Section 3.5). The fit was performed in a similar way to the fit of the ^{11}Be(-2p)^{9}He reaction, the likelihood was maximized over the same 3D parameter space, where the three parameters are the s-wave scattering length, the Maxwellian Θ, and the relative scale factor.

Similar to the ^{11}Be(-2p)^{9}He case, in a coarse-grained fit, two distinct maxima appear, depending on the size of the scale factor parameter. The global maximum occurs at a scattering length of -1 fm, a Θ of 1.0 MeV, and a scale factor of 0.5, as pictured in Figure 5.10.

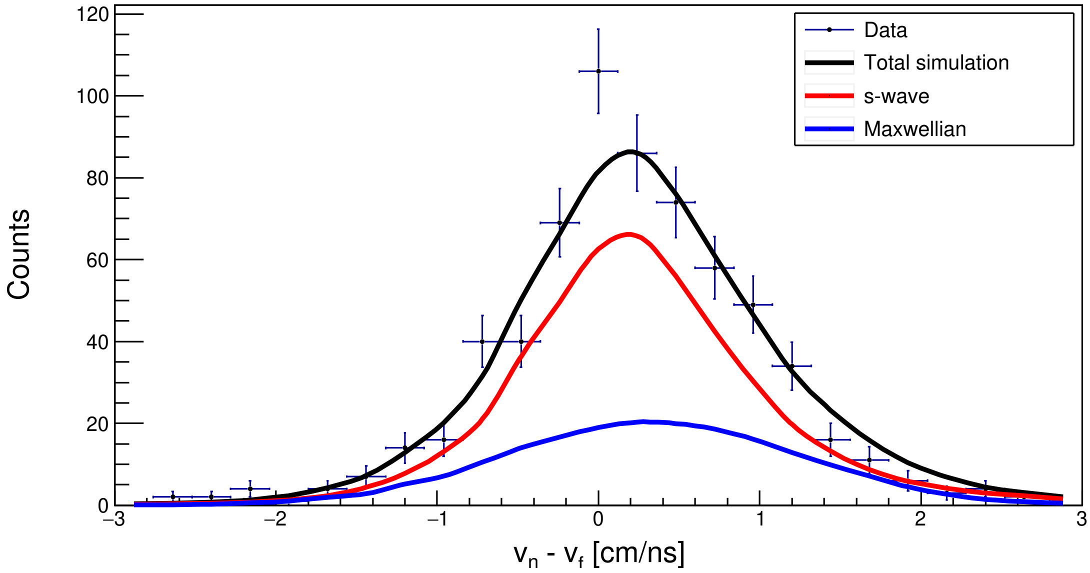

Figure 5.10: The ^{11}Be(-1p)^{10}Li decay energy at the global maximum of the coarse-grained search. The simulated parameter values are $a = -1$ fm, $\Theta = 1.0$ MeV, and a relative scale factor of 0.5.

However, if the scale factor parameter is again assumed to take on more reasonable values, there is a local maximum at a scattering length of -7 fm, a Θ of 1.0 MeV, and a scale factor of 1.5, pictured in Figure 5.11.

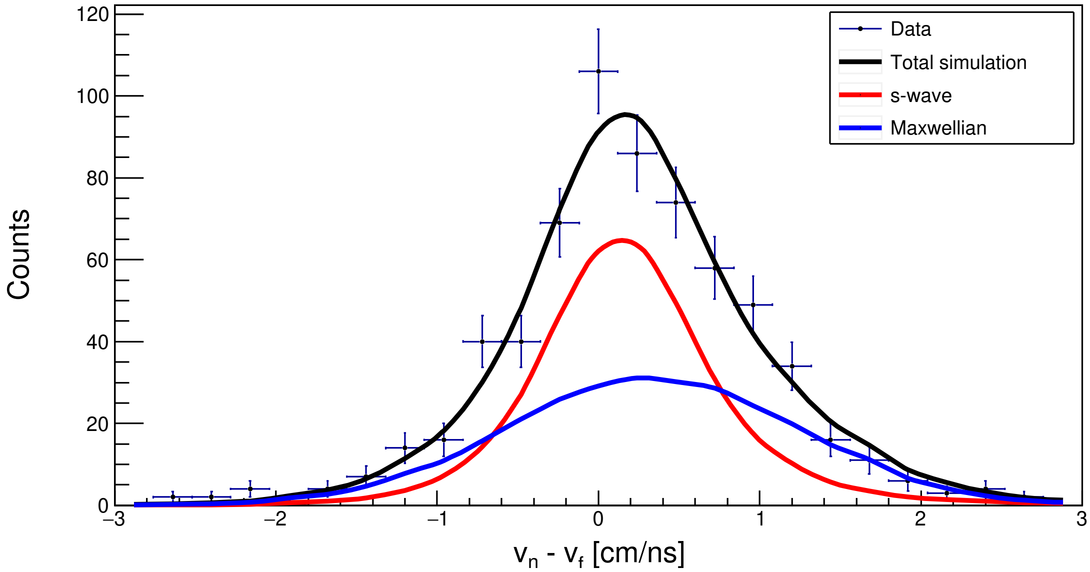

Figure 5.11: The ^{11}Be(-1p)^{10}Li decay energy at the maximum of the restricted, coarse-grained search. The simulated parameter values are $a = -7$ fm, $\Theta = 1.0$ MeV, and a relative scale factor of 1.5.

These parameters are qualitatively more consistent with the results of Kryger, *et al.* [51], where the background was also very wide, and the *s*-wave scattering length was large in magnitude. However the maximum with the -1 fm scattering length is consistent with previous works which did not observe ground state inversion.

After performing a fine-grained search around both maxima, following the same procedure as with the ^{11}Be(-2p)^{9}He data, the final values of the scattering lengths are $a = -7.0 \pm 2.4$ fm and $a = -1.4 \pm 1.0$ fm.

Chapter 6

Summary and Conclusions

In this dissertation, unbound states in ^{9}He and ^{10}Li have been reported. ^{11}Be and ^{12}B secondary beams were provided by the NSCL Coupled Cyclotron Facility, and proton removal reactions were performed using a beryllium target in order to populate the unbound states. The neutron-emission decays of these unbound states were experimentally reconstructed using the MoNA-LISA-Sweeper setup, and the decay energy or relative velocity was compared with theoretical models via Monte Carlo simulations.

Invariant mass spectroscopy was used to reconstruct decay energies for ^{9}He from both beams. From the ^{12}B beam, two levels in ^{9}He were assigned resonance energies, widths, and ℓ values. From the ^{11}Be beam, the puzzle of the possible low-lying s-wave ground state remains unsolved. Due to an ambiguity in the background model, the data from this work could either be consistent with previous results which have supported or opposed the presence of ground state inversion in ^{9}He. While there is no definitive answer to the question yet, this gives some insight into why there are apparently contradictory results in previous experimental analyses.

Additionally, the Time-of-Flight (ToF) method was used to reconstruct relative velocities for ^{10}Li from both beams. The ToF method applied to this data set was able to correctly reproduce previously-observed levels in ^{10}Li from the ^{12}B beam. Once the method was verified, it was applied to the data from the ^{11}Be beam. Similar to the case of ^{9}He from the

^{11}Be beam, the ^{10}Li relative velocity spectrum can be fit in multiple ways. Like ^{9}He, ^{10}Li also has a controversial experimental history, where some have claimed to observe ground state level inversion and others have not.

To resolve the persisting ambiguity about the possible inversion of ^{9}He and ^{10}Li, more experiments are needed, using various combinations of reaction mechanism, beam energy, and target, in order to more systematically understand how these factors contribute to the observed spectra. Additionally, improved reaction theory which includes the detailed structure of the beam and target nuclei would make experimental data easier to intepret.

APPENDIX

Appendix

Simulated annealing

```
Initialize temperature
Select first point randomly (uniform over all allowed parameter space)
Calculate $\log L$ at current point
while $T > T_{min}$ do
    while $N_{rej} < N_{stays}$ do
        Gaussian step
        Calculate $\log L$ at proposed point
        Accept/reject with acceptance probability $P(A) = \min\{1, e^{-\Delta(\log L)/T}\}$
        if Accept then
            Reset $N_{rej}$
        else
            Increment $N_{rej}$
        end
    end
    Reduce temperature according to $T_{new} = \alpha T_{old}$
end
Print result
Random restart (as many as desired)
```

REFERENCES

REFERENCES

[1] J. K. Smith. *Unbound states in the lightest island of inversion: neutron decay measurements of 11Li, 10Li, and 12Be.* PhD thesis, Michigan State University, 2014.

[2] NNDC. National Nuclear Data Center, https://www.nndc.bnl.gov.

[3] Bakken. *Wikipedia.* Feb 2008.

[4] M. D. Bird, S. J. Kenney, J. Toth, H. W. Weijers, J. C. DeKamp, M. Thoennessen, and A. F. Zeller. System Testing and Installation of the NHMFL/NSCL Sweeper Magnet. *IEEE Transactions on Applied Superconductivity*, 15(2):1252–1254, 2005.

[5] H. Liu. *Reaction mechanism dependence of the population and decay of 10He.* PhD thesis, Michigan State University, 2019.

[6] M. D. Jones. *Spectroscopy of neutron unbound states in 24O and 23N.* PhD thesis, Michigan State University, 2015.

[7] Jorge Pereira. Sweeper DAQ Wiki, https://wikihost.nscl.msu.edu/sweepermagnet/.

[8] M. Thoennessen. Reaching the limits of nuclear stability. *Reports on Progress in Physics*, 67(7):1187–1232, 2004.

[9] M. J. Savage. Nuclear physics from lattice QCD. *Progress in Particle and Nuclear Physics*, 67(2):140 – 152, 2012.

[10] S. Weinberg. Phenomenological Lagrangians. *Physica A: Statistical Mechanics and its Applications*, 96(1):327 – 340, 1979.

[11] S. Weinberg. Effective chiral Lagrangians for nucleon-pion interactions and nuclear forces. *Nuclear Physics B*, 363(1):3 – 18, 1991.

[12] R. Machleidt and D. R. Entem. Chiral effective field theory and nuclear forces. *Physics Reports*, 503(1):1 – 75, 2011.

[13] P. Hohenberg and W. Kohn. Inhomogeneous Electron Gas. *Phys. Rev.*, 136:B864–B871, 1964.

[14] W. Kohn and L. J. Sham. Self-Consistent Equations Including Exchange and Correlation Effects. *Phys. Rev.*, 140:A1133–A1138, Nov 1965.

[15] J. Dobaczewski. Current developments in nuclear density functional methods. *Journal of Physics: Conference Series*, 312(9):092002, 2011.

[16] S. A. Giuliani, Z. Matheson, W. Nazarewicz, E. Olsen, P.-G. Reinhard, J. Sadhukhan, B. Schuetrumpf, N. Schunck, and P. Schwerdtfeger. Colloquium: Superheavy elements: Oganesson and beyond. *Rev. Mod. Phys.*, 91:011001, 2019.

[17] A. V. Afanasjev, S. E. Agbemava, and A. Gyawali. Hyperheavy nuclei: Existence and stability. *Physics Letters B*, 782:533 – 540, 2018.

[18] G. Gamow. Zur Quantentheorie des Atomkernes. *Zeitschrift für Physik*, 51(3):204–212, 1928.

[19] C. F. v. Weizsäcker. Zur Theorie der Kernmassen. *Zeitschrift für Physik*, 96(7):431–458, 1935.

[20] Otto Haxel, J. Hans D. Jensen, and Hans E. Suess. On the Magic Numbers in Nuclear Structure. *Phys. Rev.*, 75:1766–1766, 1949.

[21] Maria Goeppert Mayer. Nuclear Configurations in the Spin-Orbit Coupling Model. *Phys. Rev.*, 78(16), 1950.

[22] Takaharu Otsuka. Exotic nuclei and nuclear forces. *Physica Scripta*, T152:014007, 2013.

[23] Takaharu Otsuka, Toshio Suzuki, Rintaro Fujimoto, Hubert Grawe, and Yoshinori Akaishi. Evolution of nuclear shells due to the tensor force. *Phys. Rev. Lett.*, 95:232502, 2005.

[24] G. Hagen, M. Hjorth-Jensen, G. R. Jansen, R. Machleidt, and T. Papenbrock. Continuum effects and three-nucleon forces in neutron-rich oxygen isotopes. *Phys. Rev. Lett.*, 108:242501, 2012.

[25] E. K. Warburton, J. A. Becker, and B. A. Brown. Mass systematics for A = 29-44 nuclei: The deformed A$\sim$32 region. *Phys. Rev. C*, 41:1147–1166, 1990.

[26] M. V. Zhukov, B. V. Danilin, D. V. Fedorov, J. M. Bang, I. J. Thompson, and J. S. Vaagen. Bound state properties of Borromean halo nuclei: 6He and 11Li. *Physics Reports*, 231(4):151 – 199, 1993.

[27] S. Shimoura, T. Nakamura, M. Ishihara, N. Inabe, T. Kobayashi, T. Kubo, R. H. Siemssen, I. Tanihata, and Y. Watanabe. Coulomb dissociation reaction and correlations of two halo neutrons in 11Li. *Physics Letters B*, 348(1):29 – 34, 1995.

[28] A. A. Korsheninnikov, E. Yu. Nikolskii, T. Kobayashi, A. Ozawa, S. Fukuda, E. A. Kuzmin, S. Momota, B. G. Novatskii, A. A. Ogloblin, V. Pribora, I. Tanihata, and

K. Yoshida. Spectroscopy of the halo nucleus ^{11}Li by an experimental study of ^{11}Li+p collisions. *Phys. Rev. C*, 53:R537–R540, 1996.

[29] I. Tanihata, M. Alcorta, D. Bandyopadhyay, R. Bieri, L. Buchmann, B. Davids, N. Galinski, D. Howell, W. Mills, S. Mythili, R. Openshaw, E. Padilla-Rodal, G. Ruprecht, G. Sheffer, A. C. Shotter, M. Trinczek, P. Walden, H. Savajols, T. Roger, M. Caamano, W. Mittig, P. Roussel-Chomaz, R. Kanungo, A. Gallant, M. Notani, G. Savard, and I. J. Thompson. Measurement of the Two-Halo Neutron Transfer Reaction ^{1}H(^{11}Li,^{9} Li)^{3}H at 3A MeV. *Phys. Rev. Lett.*, 100:192502, 2008.

[30] R. Kanungo, A. Sanetullaev, J. Tanaka, S. Ishimoto, G. Hagen, T. Myo, T. Suzuki, C. Andreoiu, P. Bender, A. A. Chen, B. Davids, J. Fallis, J. P. Fortin, N. Galinski, A. T. Gallant, P. E. Garrett, G. Hackman, B. Hadinia, G. Jansen, M. Keefe, R. Krücken, J. Lighthall, E. McNeice, D. Miller, T. Otsuka, J. Purcell, J. S. Randhawa, T. Roger, A. Rojas, H. Savajols, A. Shotter, I. Tanihata, I. J. Thompson, C. Unsworth, P. Voss, and Z. Wang. Evidence of Soft Dipole Resonance in ^{11}Li with Isoscalar Character. *Phys. Rev. Lett.*, 114:192502, 2015.

[31] Shigeyoshi Aoyama. Theoretical Prediction for the Ground State of ^{10}He with the Method of Analytic Continuation in the Coupling Constant. *Phys. Rev. Lett.*, 89:052501, 2002.

[32] K. Fossez, J. Rotureau, and W. Nazarewicz. Energy spectrum of neutron-rich helium isotopes: Complex made simple. *Phys. Rev. C*, 98:061302, 2018.

[33] P. G. Hansen and B. M. Sherrill. Reactions and single-particle structure of nuclei near the drip lines. *Nuclear Physics A*, 693(1):133 – 168, 2001. Radioactive Nuclear Beams.

[34] C. R. Hoffman, B. P. Kay, and J. P. Schiffer. Neutron s states in loosely bound nuclei. *Phys. Rev. C*, 89:061305, Jun 2014.

[35] Matteo Vorabbi, Angelo Calci, Petr Navrátil, Michael K. G. Kruse, Sofia Quaglioni, and Guillaume Hupin. Structure of the exotic ^{9}He nucleus from the no-core shell model with continuum. *Phys. Rev. C*, 97:034314, 2018.

[36] Kamal K. Seth, M. Artuso, D. Barlow, S. Iversen, M. Kaletka, H. Nann, B. Parker, and R. Soundranayagam. Exotic Nucleus Helium-9 and its Excited States. *Phys. Rev. Lett.*, 58:1930–1933, 1987.

[37] H. G. Bohlen, B. Gebauer, D. Kolbert, W. von Oertzen, E. Stiliaris, M. Wilpert, and T. Wilpert. Spectroscopy of 9He with the (13C,13O)-reaction on 9Be. *Zeitschrift für Physik A Atomic Nuclei*, 330(2):227–228, 1988.

[38] W. von Oertzen, H. G. Bohlen, B. Gebauer, M. von Lucke-Petsch, A. N. Ostrowski, Ch. Seyfert, Th. Stolla, M. Wilpert, Th. Wilpert, D. V. Alexandrov, A. A. Korsheninnikov,

I. Mukha, A. A. Ogloblin, R. Kalpakchieva, Y. E. Penionzhkevich, S. Piskor, S. M. Grimes, and T. N. Massey. Nuclear structure studies of very neutron-rich isotopes of 7-10He, 9-11Li and 12-14Be via two-body reactions. *Nuclear Physics A*, 588(1):c129 – c134, 1995. Proceedings of the Fifth International Symposium on Physics of Unstable Nuclei.

[39] H. G. Bohlen, A. Blazevic, B. Gebauer, W. Von Oertzen, S. Thummerer, R. Kalpakchieva, S. M. Grimes, and T. N. Massey. Spectroscopy of exotic nuclei with multi-nucleon transfer reactions. *Progress in Particle and Nuclear Physics*, 42:17 – 26, 1999. Heavy Ion Collisions from Nuclear to Quark Matter.

[40] L. Chen, B. Blank, B. A. Brown, M. Chartier, A. Galonsky, P. G. Hansen, and M. Thoennessen. Evidence for an $\ell = 0$ ground state in 9He. *Physics Letters B*, 505(1):21 – 26, 2001.

[41] G. V. Rogachev, V. Z. Goldberg, J. J. Kolata, G. Chubarian, D. Aleksandrov, A. Fomichev, M. S. Golovkov, Yu. Ts. Oganessian, A. Rodin, B. Skorodumov, R. S. Slepnev, G. Ter-Akopian, W. H. Trzaska, and R. Wolski. $t = 5/2$ states in ^{9}Li : isobaric analog states of ^{9}He. *Phys. Rev. C*, 67:041603, 2003.

[42] S. Fortier, E. Tryggestad, E. Rich, D. Beaumel, E. Becheva, Y. Blumenfeld, F. Delaunay, A. Drouart, A. Fomichev, N. Frascaria, S. Gales, L. Gaudefroy, A. Gillibert, J. Guillot, F. Hammache, K. W. Kemper, E. Khan, V. Lapoux, V. Lima, L. Nalpas, A. Obertelli, E. C. Pollacco, F. Skaza, U. Datta Pramanik, P. RousselChomaz, D. Santonocito, J. A. Scarpaci, O. Sorlin, S. V. Stepantsov, G. M. Ter Akopian, and R. Wolski. Search for resonances in 4n, 7H and 9He via transfer reactions. *AIP Conference Proceedings*, 912(1):3–12, 2007.

[43] M. S. Golovkov, L. V. Grigorenko, A. S. Fomichev, A. V. Gorshkov, V. A. Gorshkov, S. A. Krupko, Yu. Ts. Oganessian, A. M. Rodin, S. I. Sidorchuk, R. S. Slepnev, S. V. Stepantsov, G. M. Ter-Akopian, R. Wolski, A. A. Korsheninnikov, E. Yu. Nikolskii, V. A. Kuzmin, B. G. Novatskii, D. N. Stepanov, P. Roussel-Chomaz, and W. Mittig. New insight into the low-energy ^{9}He spectrum. *Phys. Rev. C*, 76:021605, 2007.

[44] H. T. Johansson, Yu. Aksyutina, T. Aumann, K. Boretzky, M. J. G. Borge, A. Chatillon, L. V. Chulkov, D. Cortina-Gil, U. Datta Pramanik, H. Emling, C. Forssén, H. O. U. Fynbo, H. Geissel, G. Ickert, B. Jonson, R. Kulessa, C. Langer, M. Lantz, T. LeBleis, K. Mahata, M. Meister, and G. M˙ The unbound isotopes 9,10He. *Nuclear Physics A*, 842(1):15 – 32, 2010.

[45] H. Al Falou, A. Leprince, and N. A. Orr. Structure of the neutron-rich N = 7 isotones 10Li and 9He. *Journal of Physics: Conference Series*, 312(9):092012, 2011.

[46] T. Al Kalanee, J. Gibelin, P. Roussel-Chomaz, N. Keeley, D. Beaumel, Y. Blumenfeld, B. Fernández-Domínguez, C. Force, L. Gaudefroy, A. Gillibert, J. Guillot, H. Iwasaki,

S. Krupko, V. Lapoux, W. Mittig, X. Mougeot, L. Nalpas, E. Pollacco, K. Rusek, T. Roger, H. Savajols, N. de Séréville, S. Sidorchuk, D. Suzuki, I. Strojek, and N. A. Orr. Structure of unbound neutron-rich ^{9}He studied using single-neutron transfer. *Phys. Rev. C*, 88:034301, 2013.

[47] E. Uberseder, G. V. Rogachev, V. Z. Goldberg, E. Koshchiy, B. T. Roeder, M. Alcorta, G. Chubarian, B. Davids, C. Fu, J. Hooker, H. Jayatissa, D. Melconian, and R. E. Tribble. Nuclear structure beyond the neutron drip line: The lowest energy states in 9He via their T = 5/2 isobaric analogs in 9Li. *Physics Letters B*, 754:323 – 327, 2016.

[48] H. T. Fortune. Constraints on energies of ^{10}He(0^{+}) and ^{9}He($1/2^{+}$). *Phys. Rev. C*, 91:034306, 2015.

[49] K. H. Wilcox, R. B. Weisenmiller, G. J. Wozniak, N. A. Jelley, D. Ashery, and J. Cerny. The (9Be,8B) reaction and the unbound nuclide 10Li. *Physics Letters B*, 59(2):142 – 144, 1975.

[50] A. I. Amelin et al. *Sov. J. Nucl. Phys.*, 52(501), 1990.

[51] R. A. Kryger, A. Azhari, A. Galonsky, J. H. Kelley, R. Pfaff, E. Ramakrishnan, D. Sackett, B. M. Sherrill, M. Thoennessen, J. A. Winger, and S. Yokoyama. Neutron decay of ^{10}Li produced by fragmentation. *Phys. Rev. C*, 47:R2439–R2442, Jun 1993.

[52] H. G. Bohlen, B. Gebauer, M. von Lucke-Petsch, W. von Oertzen, A. N. Ostrowski, M. Wilpert, Th. Wilpert, H. Lenske, D. V. Alexandrov, A. S. Demyanova, E. Nikolskii, A. A. Korsheninnikov, A. A. Ogloblin, R. Kalpakchieva, Y. E. Penionzhkevich, and S. Piskor. Solution of the 10Li Puzzle. *Zeitschrift für Physik A Hadrons and Nuclei*, 344(4):381–393, 1993.

[53] B. M. Young, W. Benenson, M. Fauerbach, J. H. Kelley, R. Pfaff, B. M. Sherrill, M. Steiner, J. S. Winfield, T. Kubo, M. Hellström, N. A. Orr, J. Stetson, J. A. Winger, and S. J. Yennello. Mass of ^{11}Li from the ^{14}C(^{11}B,^{11}Li)^{14}O Reaction. *Phys. Rev. Lett.*, 71:4124–4126, 1993.

[54] M. Zinser, F. Humbert, T. Nilsson, W. Schwab, H. Simon, T. Aumann, M. J. G. Borge, L. V. Chulkov, J. Cub, Th. W. Elze, H. Emling, H. Geissel, D. Guillemaud-Mueller, P. G. Hansen, R. Holzmann, H. Irnich, B. Jonson, J. V. Kratz, R. Kulessa, Y. Leifels, H. Lenske, A. Magel, A. C. Mueller, and G. M˙Invariant-mass spectroscopy of 10Li and 11Li. *Nuclear Physics A*, 619(1):151 – 176, 1997.

[55] T. Kobayashi, K. Yoshida, A. Ozawa, I. Tanihata, A. Korsheninnikov, E. Nikolski, and T. Nakamura. Quasifree nucleon-knockout reactions from neutron-rich nuclei by a proton target: p(6He,pn)5He, p(11Li,pn)10Li, p(6he,2p)5H, and p(11Li,2p)10He. *Nuclear Physics A*, 616(1):223 – 230, 1997. Radioactive Nuclear Beams.

[56] H. G. Bohlen, W. von Oertzen, Th. Stolla, R. Kalpakchieva, B. Gebauer, M. Wilpert, Th. Wilpert, A. N. Ostrowski, S. M. Grimes, and T. N. Massey. Study of weakly bound and unbound states of exotic nuclei with binary reactions. *Nuclear Physics A*, 616(1):254 – 261, 1997. Radioactive Nuclear Beams.

[57] G. F. Bertsch, K. Hencken, and H. Esbensen. Nuclear breakup of Borromean nuclei. *Phys. Rev. C*, 57:1366–1377, 1998.

[58] J. A. Caggiano, D. Bazin, W. Benenson, B. Davids, B. M. Sherrill, M. Steiner, J. Yurkon, A. F. Zeller, and B. Blank. Spectroscopy of the ^{10}Li nucleus. *Phys. Rev. C*, 60:064322, 1999.

[59] M. Thoennessen, S. Yokoyama, A. Azhari, T. Baumann, J. A. Brown, A. Galonsky, P. G. Hansen, J. H. Kelley, R. A. Kryger, E. Ramakrishnan, and P. Thirolf. Population of ^{10}Li by fragmentation. *Phys. Rev. C*, 59:111–117, 1999.

[60] M. Chartier, J. R. Beene, B. Blank, L. Chen, A. Galonsky, N. Gan, K. Govaert, P. G. Hansen, J. Kruse, V. Maddalena, M. Thoennessen, and R. L. Varner. Identification of the 10Li ground state. *Physics Letters B*, 510(1):24 – 28, 2001.

[61] P. Santi, J. J. Kolata, V. Guimãraes, D. Peterson, R. White-Stevens, E. Rischette, D. Bazin, B. M. Sherrill, A. Navin, P. A. DeYoung, P. L. Jolivette, G. F. Peaslee, and R. T. Guray. Structure of the ^{10}Li nucleus investigated via the $^{9}\mathrm{Li}(d,p)^{10}\mathrm{Li}$ reaction. *Phys. Rev. C*, 67:024606, 2003.

[62] H. B. Jeppesen, A. M. Moro, U. C. Bergmann, M. J. G. Borge, and J. Cederk˙Study of 10Li via the 9Li(2H,p) reaction at REX-ISOLDE. *Physics Letters B*, 642(5):449 – 454, 2006.

[63] H. Simon, M. Meister, T. Aumann, M. J. G. Borge, L. V. Chulkov, U. Datta Pramanik, Th. W. Elze, H. Emling, C. Forssén, H. Geissel, and M. Hellstr˙Systematic investigation of the drip-line nuclei 11Li and 14Be and their unbound subsystems 10Li and 13Be. *Nuclear Physics A*, 791(3):267 – 302, 2007.

[64] J. K. Smith, T. Baumann, J. Brown, P. A. DeYoung, N. Frank, J. Hinnefeld, Z. Kohley, B. Luther, B. Marks, A. Spyrou, S. L. Stephenson, M. Thoennessen, and S. J. Williams. Selective population of unbound states in 10Li. *Nuclear Physics A*, 940:235 – 241, 2015.

[65] B. A. Chernyshev, Yu. B. Gurov, L. Yu. Korotkova, S. V. Lapushkin, R. V. Pritula, and V. G. Sandukovsky. Study of the level structure of the lithium isotope 10Li in stopped pion absorption. *International Journal of Modern Physics E*, 24(01):1550004, 2015.

[66] A. Sanetullaev, R. Kanungo, J. Tanaka, M. Alcorta, C. Andreoiu, P. Bender, A. A. Chen, G. Christian, B. Davids, J. Fallis, J. P. Fortin, N. Galinski, A. T. Gallant, P. E. Garrett, G. Hackman, B. Hadinia, S. Ishimoto, M. Keefe, and R. Kr˙Investigation of the

role of 10Li resonances in the halo structure of 11Li through the Li11(p,d)Li10 transfer reaction. *Physics Letters B*, 755:481 – 485, 2016.

[67] M. Cavallaro, M. De Napoli, F. Cappuzzello, S. E. A. Orrigo, C. Agodi, M. Bondí, D. Carbone, A. Cunsolo, B. Davids, T. Davinson, A. Foti, N. Galinski, R. Kanungo, H. Lenske, C. Ruiz, and A. Sanetullaev. Investigation of the ^{10}Li shell inversion by neutron continuum transfer reaction. *Phys. Rev. Lett.*, 118:012701, 2017.

[68] Yu. Aksyutina, H. T. Johansson, P. Adrich, F. Aksouh, T. Aumann, K. Boretzky, M. J. G. Borge, A. Chatillon, L. V. Chulkov, D. Cortina-Gil, U. Datta Pramanik, H. Emling, C. Forssn, H. O. U. Fynbo, H. Geissel, M. Hellstrm, G. Ickert, K. L. Jones, B. Jonson, A. Kliemkiewicz, J. V. Kratz, R. Kulessa, M. Lantz, T. LeBleis, A. O. Lindahl, K. Mahata, M. Matos, M. Meister, G. Mnzenberg, T. Nilsson, G. Nyman, R. Palit, M. Pantea, S. Paschalis, W. Prokopowicz, R. Reifarth, A. Richter, K. Riisager, G. Schrieder, H. Simon, K. Smmerer, O. Tengblad, W. Walus, H. Weick, and M. V. Zhukov. Lithium isotopes beyond the drip line. *Physics Letters B*, 666(5):430 – 434, 2008.

[69] I. J. Thompson and F. M. Nunes. *Nuclear Reactions for Astrophysics.* Cambridge University Press, 1 edition, 2009.

[70] A. M. Lane and R. G. Thomas. R-Matrix Theory of Nuclear Reactions. *Rev. Mod. Phys.*, 30:257–353, 1958.

[71] F. Marti, P. Miller, D. Poe, M. Steiner, J. Stetson, and X. Y. Wu. Commissioning of the coupled cyclotron system at nscl. *AIP Conference Proceedings*, 600(1):64–68, 2001.

[72] I. Tanihata. Radioactive beam facilities and their physics program. *Nuclear Physics A*, 553:361 – 372, 1993.

[73] D. J. Morrissey, B. M. Sherrill, M. Steiner, A. Stolz, and I. Wiedenhoever. Commissioning the A1900 projectile fragment separator. *Nuclear Instruments and Methods in Physics Research Section B: Beam Interactions with Materials and Atoms*, 204:90 – 96, 2003. 14th International Conference on Electromagnetic Isotope Separators and Techniques Related to their Applications.

[74] J. Yurkon, D. Bazin, W. Benenson, D. J. Morrissey, B. M. Sherrill, D. Swan, and R. Swanson. Focal plane detector for the S800 high-resolution spectrometer. *Nuclear Instruments and Methods in Physics Research Section A: Accelerators, Spectrometers, Detectors and Associated Equipment*, 422(1):291 – 295, 1999.

[75] B. Luther, T. Baumann, M. Thoennessen, J. Brown, P. DeYoung, J. Finck, J. Hinnefeld, R. Howes, K. Kemper, P. Pancella, G. Peaslee, W. Rogers, and S. Tabor. MoNA – The Modular Neutron Array. *Nuclear Instruments and Methods in Physics Research Section A: Accelerators, Spectrometers, Detectors and Associated Equipment*, 505(1):33

– 35, 2003. Proceedings of the tenth Symposium on Radiation Measurements and Applications.

[76] N. Frank. *Spectroscopy of neutron unbound states in neutron rich oxygen isotopes.* PhD thesis, Michigan State University, 2006.

[77] N. Frank, A. Schiller, D. Bazin, W. A. Peters, and M. Thoennessen. Reconstruction of nuclear charged fragment trajectories from a large-gap sweeper magnet. *Nuclear Instruments and Methods in Physics Research Section A: Accelerators, Spectrometers, Detectors and Associated Equipment*, 580(3):1478 – 1484, 2007.

[78] N. Frank, T. Baumann, D. Bazin, B. A. Brown, J. Brown, P. A. DeYoung, J. E. Finck, A. Gade, J. Hinnefeld, R. Howes, J.-L. Lecouey, B. Luther, W. A. Peters, H. Scheit, A. Schiller, M. Thoennessen, and J. Tostevin. Neutron decay spectroscopy of neutron-rich oxygen isotopes. *Nuclear Physics A*, 813(3):199 – 211, 2008.

[79] B. Peters. *Study of neutron unbound states using the Modular Neutron Array (MoNA).* PhD thesis, Michigan State University, 2007.

[80] G. Christian. *Spectroscopy of neutron-unbound fluorine.* PhD thesis, Michigan State University, 2011.

[81] K. E. Stiefel. *Measurement and modeling of fragments and neutrons produced from projectile fragmentation reactions.* PhD thesis, Michigan State University, 2018.

[82] Ron Fox. NSCLDAQ 11.2 documentation, http://docs.nscl.msu.edu/daq/newsite/nscldaq-11.2/index.html.

[83] Ron Fox. SpecTcl documentation, http://docs.nscl.msu.edu/daq/spectcl/.

[84] J. M. Paul. The density effect and rate of energy loss in common plastic scintillators. *Nuclear Instruments and Methods*, 96(1):51 – 59, 1971.

[85] G. F. Knoll. *Radiation Detection and Measurement.* John Wiley and Sons, Inc., 4 edition, 2010.

[86] Kyoko Makino and Martin Berz. Cosy INFINITY version 8. *Nuclear Instruments and Methods in Physics Research Section A: Accelerators, Spectrometers, Detectors and Associated Equipment*, 427(1):338 – 343, 1999.

[87] M. Berz, K. Makino, and W. Wan. *An Introduction to Beam Physics.* CRC Press, 2015.

[88] S. Agostinelli, J. Allison, K. Amako, J. Apostolakis, H. Araujo, P. Arce, M. Asai, D. Axen, S. Banerjee, G. Barrand, F. Behner, L. Bellagamba, J. Boudreau, L. Broglia, A. Brunengo, H. Burkhardt, S. Chauvie, J. Chuma, R. Chytracek, G. Cooperman,

G. Cosmo, P. Degtyarenko, A. Dell'Acqua, G. Depaola, D. Dietrich, R. Enami, A. Feliciello, C. Ferguson, H. Fesefeldt, G. Folger, F. Foppiano, A. Forti, S. Garelli, S. Giani, R. Giannitrapani, D. Gibin, J. J. Gómez Cadenas, I. González, G. Gracia Abril, G. Greeniaus, W. Greiner, V. Grichine, A. Grossheim, S. Guatelli, P. Gumplinger, R. Hamatsu, K. Hashimoto, H. Hasui, A. Heikkinen, A. Howard, V. Ivanchenko, A. Johnson, F.W. Jones, J. Kallenbach, N. Kanaya, M. Kawabata, Y. Kawabata, M. Kawaguti, S. Kelner, P. Kent, A. Kimura, T. Kodama, R. Kokoulin, M. Kossov, H. Kurashige, E. Lamanna, T. Lampn, V. Lara, V. Lefebure, F. Lei, M. Liendl, W. Lockman, F. Longo, S. Magni, M. Maire, E. Medernach, K. Minamimoto, P. Mora de Freitas, Y. Morita, K. Murakami, M. Nagamatu, R. Nartallo, P. Nieminen, T. Nishimura, K. Ohtsubo, M. Okamura, S. O'Neale, Y. Oohata, K. Paech, J. Perl, A. Pfeiffer, M.G. Pia, F. Ranjard, A. Rybin, S. Sadilov, E. Di Salvo, G. Santin, T. Sasaki, N. Savvas, Y. Sawada, S. Scherer, S. Sei, V. Sirotenko, D. Smith, N. Starkov, H. Stoecker, J. Sulkimo, M. Takahata, S. Tanaka, E. Tcherniaev, E. Safai Tehrani, M. Tropeano, P. Truscott, H. Uno, L. Urban, P. Urban, M. Verderi, A. Walkden, W. Wander, H. Weber, J. P. Wellisch, T. Wenaus, D. C. Williams, D. Wright, T. Yamada, H. Yoshida, and D. Zschiesche. GEANT4 a simulation toolkit. *Nuclear Instruments and Methods in Physics Research Section A: Accelerators, Spectrometers, Detectors and Associated Equipment*, 506(3):250 – 303, 2003.

[89] J. Allison, K. Amako, J. Apostolakis, H. Araujo, P. Arce Dubois, M. Asai, G. Barrand, R. Capra, S. Chauvie, R. Chytracek, G. A. P. Cirrone, G. Cooperman, G. Cosmo, G. Cuttone, G. G. Daquino, M. Donszelmann, M. Dressel, G. Folger, F. Foppiano, J. Generowicz, V. Grichine, S. Guatelli, P. Gumplinger, A. Heikkinen, I. Hrivnacova, A. Howard, S. Incerti, V. Ivanchenko, T. Johnson, F. Jones, T. Koi, R. Kokoulin, M. Kossov, H. Kurashige, V. Lara, S. Larsson, F. Lei, O. Link, F. Longo, M. Maire, A. Mantero, B. Mascialino, I. McLaren, P. Mendez Lorenzo, K. Minamimoto, K. Murakami, P. Nieminen, L. Pandola, S. Parlati, L. Peralta, J. Perl, A. Pfeiffer, M. G. Pia, A. Ribon, P. Rodrigues, G. Russo, S. Sadilov, G. Santin, T. Sasaki, D. Smith, N. Starkov, S. Tanaka, E. Tcherniaev, B. Tome, A. Trindade, P. Truscott, L. Urban, M. Verderi, A. Walkden, J. P. Wellisch, D. C. Williams, D. Wright, and H. Yoshida. GEANT4 developments and applications. *IEEE Transactions on Nuclear Science*, 53(1):270–278, 2006.

[90] A. S. Goldhaber. Statistical models of fragmentation processes. *Physics Letters B*, 53(4):306 – 308, 1974.

[91] K. Van Bibber, D. L. Hendrie, D. K. Scott, H. H. Weiman, L. S. Schroeder, J. V. Geaga, S. A. Cessin, R. Treuhaft, Y. J. Grossiord, J. O. Rasmussen, and C. Y. Wong. Evidence for Orbital Dispersion in the Fragmentation of ^{16}O at 90 and 120 MeV/Nucleon. *Phys. Rev. Lett.*, 43:840–844, 1979.

[92] J. B. Birks. The specific Fluorescence of Anthracene and Other Organic Materials. *Phys. Rev.*, 84:364–365, 1951.

[93] G. Cowan. *Statistical Data Analysis.* Oxford University Press, 1998.